



## Durham E-Theses

---

### *Photonic crystal fibres in astronomy*

Corbett, Jason CW.

#### How to cite:

---

Corbett, Jason CW. (2006) *Photonic crystal fibres in astronomy*, Durham theses, Durham University. Available at Durham E-Theses Online: <http://etheses.dur.ac.uk/2661/>

#### Use policy

---

The full-text may be used and/or reproduced, and given to third parties in any format or medium, without prior permission or charge, for personal research or study, educational, or not-for-profit purposes provided that:

- a full bibliographic reference is made to the original source
- a [link](#) is made to the metadata record in Durham E-Theses
- the full-text is not changed in any way

The full-text must not be sold in any format or medium without the formal permission of the copyright holders.

Please consult the [full Durham E-Theses policy](#) for further details.

# Photonic crystal fibres in astronomy

Jason CW Corbett

The copyright of this thesis rests with the author or the university to which it was submitted. No quotation from it, or information derived from it may be published without the prior written consent of the author or university, and any information derived from it should be acknowledged.

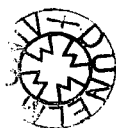
A Thesis presented to Durham University in  
accordance with the regulations for admittance  
to the degree of Doctor of Philosophy

Centre for Advanced Instrumentation

Dept. of Physics

Durham University

December 2006



- 8 AUG 2007

# Photonic crystal fibres in astronomy

or (Collected thoughts in Natural Philosophy)

Jason CW Corbett - December 2006

## Abstract

Photonic crystal fibres (PCF) are a new generation of optical fibre that guide light via a periodic air-silica, photonic crystal structure instead of the more traditional step change in refractive index associated with traditional fibre. Careful design of the photonic structure causes the fibres to behave in interesting new ways and one of main aims of this thesis is to begin the investigation of the uses of PCF's in astronomy.

Step index and large mode area (LMA) PCF's are introduced in Chapters 2 and 3, respectively. Chapter 4 then deals with the instrumental simplifications associated with the use of LMA PCF's in fibre stellar interferometry showing that up to four step index fibres and associated optics can be replaced with a single LMA fibre.

One of the key features of LMA fibres, for astronomy, is that, unlike the step index fibre, the mode field size is independent of wavelength and the fibre can therefore be fed with a pupil image via a field lens. Chapter 5 investigates this important new parameter space showing that contiguous sampling using single mode fibres is now possible for the first time. Further, unlike the direct feed to the LMA fibre, maximised coupling over very large wavebands is now possible using just a single fibre.

Chapter 6 deals with another new fibre technology in astronomy: Multi-mode fibre (MMF) to single-mode array (SMA) transitions. These fibre systems break out the modes of the multi-mode fibre into an array of single-mode fibres upon which Bragg gratings can be etched. The SMA is then refused into an output MMF resulting in a multimode device but with single-mode line suppression. The number of modes transmitted is numerically equal to the number of fibres in the SMA and the performance of these devices is investigated on a model telescope showing that only a few tens of modes is required to efficiently transmit either the J or H bands.

Finally, Chapter 7 details the experimental investigation of fibre modal noise in high dispersion spectroscopy. This is a photometric error on a resolution element due to fibre modes interfering with each other at very high spectral dispersion. Worryingly, the results show that no current theory exists that can predict the performance of a fibre based high R spectrometer.

## Declaration

The work in this thesis is based on research carried out at the Centre for Advanced Instrumentation in the Department of Physics of Durham University in the United Kingdom. No part of this thesis has been submitted elsewhere for any other degree or qualification.

Chapters 4 and 6 were published in Monthly Notices of the Royal Astronomical Society [1,2], and the first part of Chapter 5 in Optics Express [3]. These three papers were all collaborations, however, I was lead author and primary researcher on all of them. Chapter 7 describes the first phase of a work in progress but will be submitted to MNRAS early next year. This is a collaboration with Jeremy Allington-Smith but again, I am lead researcher and will be lead author this paper as-well.

- 1) 'The coupling performance of photonic crystal fibres in fibre stellar interferometry', JCW Corbett, A Dabirian, T Butterley, NA Mortensen, JR Allington-Smith, Monthly Notices of the Royal Astronomical Society, **368**, 203–210, (2006)
- 2) 'Fibre modal power distributions for OH-suppression applications in Astronomy', Jason CW Corbett, T Butterley, JR Allington-Smith, Monthly Notices of the Royal Astronomical Society, *On-line early May (2006)*.
- 3) 'Coupling starlight into single-mode photonic crystal fibre using a field lens', JCW Corbett and J.R. Allington-Smith, Optics Express, Vol. **13**, Iss. 17 (2005) pp: 6527-6540

**Copyright © 2006 by Jason CW Corbett**

“This copy has been supplied for the purpose of research or private study on the understanding that it is copyright material and that no quotation from the thesis may be published without proper acknowledgement.”

## Acknowledgements

Many thanks must go firstly to Dr Jeremy Allington-Smith, my thesis advisor, for whom I have provided the subtitle to this thesis. Jeremy's balance of hand holding and student autonomy was ideal and I flourished under his guidance.

Many thanks should also go to Professors, Ray Sharples and Tim Birks for the curiously enjoyable viva (15.3.07 at Durham). Both remained friendly and yet persistent throughout. I guess any chance a scientist gets to discuss their work is welcome, even under exam conditions!

Thanks also to my office mates throughout, nearly all of, my PhD, Tim B, Tim M and also Chris S, whom I lodged with for a year, or so. Since it is unlikely to be published anywhere else, Chris holds the Galactic record of eating 3.2 metres of Twix™ in two days. Well done that man. Further, Tim B and I have collaborated on two full Journal papers now and Tim M and I have collaborated on a conference paper, but it turns out that this is likely to be quite an important one.

I'd like also thank my Mum, Cece and Dad, Johnny, my in-laws, Cynthia and Chris, my brother's Marcus and Luke, sister's-in-law Becky and Claire and my niece and nephew, Megan and Charlie...er... because I can, really. I also need to thank Julie Skerrit, Mel Weaver and Claire Whaley for keeping my wife sane over the past few years. Thanks to my eldest son, Ben, for keeping me, by turns, up all night and endlessly entertained during the PhD. He has coped very well with having a weekend father whilst I worked away. Thanks also to Baby Sam who, having been born after the viva, has provided welcome distraction from the thesis corrections. Nice one old boys! And finally.....

## **Dedication**

Ten years ago, I signed up to the Open University to start my undergraduate degree in Physics. My wife, Tracey, didn't really have an opinion at the time, it was just another in a long line of hobbies for me. Seven years, one renovated house and a baby Ben later, I completed the degree without either of us having taken a holiday and worse, any holiday entitlement I did have, having been used to go away to summer schools.

Almost immediately after this I asked her if I could leave my well paid job, move us all to the other end of the country and sell our house to supplement our income, whilst I tried to achieve my life's ambition to become a Doctor. Despite the fact that she was suffering from post-natal depression at the time, she said yes!

We moved to Durham and almost immediately Tracey's condition worsened. However, she remained in Durham for a further 18 months before going back to Hereford. I then commuted between Hereford and Durham on a weekly basis for the last 18 months of the degree whilst she recovered and at the same time looked after our eldest son, Ben, as, effectively, a single parent during the week. To compound matters, she was also pregnant, with Baby Sam, for the last four/five months of the PhD.

We have now been together for over 17 years and married for 11 of those. She is my childhood sweetheart and quite simply the bravest person I have ever met. This thesis is dedicated solely to her. Having passed my viva voce, I have achieved my life's ambition but owe her a debt I can never repay.

Finally, because only Trace and I know what this means, I am crying whilst I write this dedication.

For Tracey Anne Corbett

# Contents

<b>1</b>	<b>INTRODUCTION</b>	<b>1</b>
1.1	INTRODUCTION	1
1.2	OPTICAL FIBERS AND ASTRONOMY	1
1.3	PHOTONIC CRYSTAL FIBRES	4
1.4	PHOTONIC INSTRUMENTATION	6
1.5	MULTIMODE FIBRES IN MODERN ASTRONOMY	8
1.6	SUMMARY OF THESIS CONTENTS	9
1.7	REFERENCES	11
<b>2</b>	<b>STEP INDEX FIBRES</b>	<b>16</b>
2.1	INTRODUCTION	16
2.2	THE RAY OPTICAL MODEL	17
2.2.1	<i>The guidance mechanism</i>	17
2.2.2	<i>Types of ray mode</i>	17
2.2.3	<i>The numerical aperture</i>	18
2.2.4	<i>Ray optical model comment</i>	19
2.3	THE ELECTROMAGNETIC MODE MODEL	19
2.3.1	<i>Some basic properties of EM modes</i>	20
2.3.2	<i>Using the scalar wave equation</i>	22
2.3.3	<i>The solution of the scalar wave equation in the step index case</i>	23
2.3.4	<i>Description of EM modes</i>	26
2.3.5	<i>Comparison with the ray optical model</i>	30
2.3.6	<i>The single-mode regime</i>	31
2.4	THE COUPLING INTEGRAL	32
2.4.2	<i>Range of validity of the coupling integral</i>	36
2.5	SUMMARY	39
2.6	REFERENCES	39
<b>3</b>	<b>PHOTONIC CRYSTAL FIBRES</b>	<b>40</b>
3.1	INTRODUCTION	40
3.2	SOME PHYSICAL BACKGROUND	40
3.3	PHOTONIC BAND GAP FIBRES	43
3.3.1	<i>- The photonic band gap</i>	43
3.3.2	<i>The waveguiding mechanism of PBG fibres</i>	46
3.3.3	<i>Characteristics of PBG fibres</i>	48
3.4	INDEX GUIDING FIBRES	48
3.4.1	<i>General principles</i>	48
3.4.2	<i>- Endlessly single-mode behaviour</i>	50
3.4.3	<i>- Characteristics of index guiding (single-mode) fibres</i>	55

3.5	THE COUPLING INTEGRAL REVISITED .....	55
3.6	SUMMARY.....	57
3.7	REFERENCES .....	57
<b>4</b>	<b>COUPLING STARLIGHT INTO PCF'S - I - DIRECT FEED.....</b>	<b>60</b>
4.1	INTRODUCTION .....	60
4.2	COUPLING LIGHT IN IDEAL SEEING CONDITIONS .....	62
4.2.1	<i>On-axis coupling in ideal seeing</i> .....	64
4.2.2	<i>Off-axis coupling in ideal seeing</i> .....	67
4.3	COUPLING LIGHT WITH NATURAL SEEING .....	69
4.3.1	<i>Fibre feed focal ratio</i> .....	74
4.3.2	<i>Coupling variations with atmosphere</i> .....	74
4.4	DEFOCUSED AIRY RESULTS.....	76
4.5	SUMMARY.....	79
4.6	REFERENCES .....	80
<b>5</b>	<b>COUPLING STARLIGHT INTO PCF'S - II - FIELD LENS FEED.....</b>	<b>82</b>
5.1	INTRODUCTION .....	82
5.2	THE OPTICAL MODEL.....	83
5.3	CHARACTERISTICS OF THE FIELD LENS FEED .....	86
5.3.1	<i>On axis source</i> .....	86
5.3.2	<i>Gaussian apodisation</i> .....	89
5.3.3	<i>Off axis source</i> .....	89
5.3.4	<i>Coupling due to the fibre, <math>\rho_f(\theta)</math></i> .....	90
5.3.5	<i>Coupling due to the lenslet, <math>\rho_s(\theta)</math></i> .....	94
5.4	COMPARISON OF DIRECT AND FIELD LENS COUPLING .....	94
5.5	SINGLE-MODE FIBRES IN INTEGRAL FIELD SPECTROSCOPY? .....	97
5.5.1	<i>Telecentric requirement</i> .....	98
5.5.2	<i>The coupling of multiple lenslets</i> .....	98
5.5.3	<i>The effect of slower lenslets</i> .....	99
5.5.4	<i>Single-mode sampling</i> .....	101
5.6	EXPERIMENTAL CONSIDERATIONS .....	104
5.6.1	<i>Fibre Preparation</i> .....	104
5.6.2	<i>Experimental investigation of the LMA fibre</i> .....	108
5.7	SUMMARY.....	112
5.8	REFERENCES .....	113
<b>6</b>	<b>MMF TO SMA FIBRES .....</b>	<b>114</b>
6.1	INTRODUCTION .....	114
6.2	THE FIBRE MODEL .....	115
6.2.1	<i>From the MMF to the SMA</i> .....	115

6.2.2	<i>The geometrical, ray optical, model</i> .....	116
6.2.3	<i>The general effect of <math>M &lt; N</math></i> .....	117
6.2.4	<i>The coupling calculations</i> .....	118
6.3	<b>AIRY PATTERN COUPLING</b> .....	118
6.3.1	<i>Ideal seeing</i> .....	118
6.3.2	<i>M, transmission and field of view</i> .....	122
6.3.3	<i>Airy pattern coupling - Natural seeing</i> .....	124
6.4	<b>PUPIL COUPLING</b> .....	127
6.4.1	<i>Negligible spherical term - Ideal seeing</i> .....	127
6.4.2	<i>Non- negligible spherical term - Ideal seeing</i> .....	129
6.4.3	<i>The field of view as a function of M</i> .....	131
6.4.4	<i>Sampling performance of OH suppression fibres</i> .....	134
6.4.5	<i>The effect of de-focusing, demagnification and de-centration of the pupil image on the MPD.</i> 135	
6.5	<b>SUMMARY</b> .....	135
6.6	<b>REFERENCES</b> .....	136
<b>7</b>	<b>FIBRE MODAL NOISE</b> .....	<b>138</b>
7.1	<b>INTRODUCTION</b> .....	138
7.2	<b>WHAT IS MODAL NOISE?</b> .....	139
7.2.1	<i>Effects of an arbitrary field of view – Perfect fibre</i> .....	141
7.2.2	<i>The effects of non-perfect fibres</i> .....	143
7.3	<b>HOW IS MODAL NOISE DESCRIBED?</b> .....	144
7.4	<b>EXPERIMENTAL INVESTIGATION OF MODAL NOISE – EXPERIMENTAL SETUP</b> .....	151
7.4.1	<i>Spectrometer design</i> .....	151
7.5	<b>EXPERIMENTAL INVESTIGATION OF MODAL NOISE – MULTIMODE FIBRE</b> .....	156
7.5.1	<i>Introduction</i> .....	156
7.5.2	<i>Details of the analysis</i> .....	156
7.5.3	<i>Coherent illumination</i> .....	158
7.5.4	<i>Partially coherent illumination</i> .....	159
7.6	<b>EXPERIMENTAL INVESTIGATION OF MODAL NOISE – SINGLE-MODE PCF</b> .....	165
7.7	<b>SUMMARY</b> .....	166
7.8	<b>REFERENCES</b> .....	167
<b>8</b>	<b>CLOSING COMMENTS</b> .....	<b>170</b>
8.1	<b>INTRODUCTION</b> .....	170
8.2	<b>THESIS SYNOPSIS</b> .....	170
8.3	<b>CONTRIBUTION</b> .....	171
8.4	<b>PROPOSALS OF FURTHER WORK</b> .....	172
8.5	<b>FINAL WORDS</b> .....	174
8.6	<b>REFERENCES</b> .....	175

# *Chapter 1*

---

## *Optical fibre technology and astronomy*

### *1.1 Introduction*

In this introductory chapter some of the more common uses of optical fibre technology in astronomy are explained. New fibre technologies and, at least as importantly, new instrument technologies that require specialist fibre feeds, such as single mode fibres are also covered and the relationships between them discussed. Pointers to each chapter within the thesis occur throughout, intended to place the contents of the thesis in context. A general overview is given in section 1.2, with the new breed of photonic crystal fibres, photonic instrumentation and more modern fibre technologies such as OH suppression devices, described in sections 1.3 – 1.5. Section 1.6 then gives an overview of the thesis on chapter by chapter basis.

### *1.2 Optical fibres and astronomy*

Optical fibres are currently used in astronomy for a number of reasons but the three most prevalent are measurement multiplicity, convenient light transport at large facility class telescopes and image scrambling.

Integral field spectroscopy, whilst possible using image slicing techniques has been achieved with great success using optical fibres. The technique is based on the pixelisation of the image field by a lenslet array. Each lenslet then feeds a fibre which is then re-formatted into a single input slit to a spectrometer. The 3 dimensional data cube, of two spatial and one spectral dimension, then gives this branch of astronomy

its name – 2D spectroscopy\*. Figure 1.1 is a schematic representation of the process where the integral field unit is used to analyse a particular object in the Abell 2218 galaxy cluster.

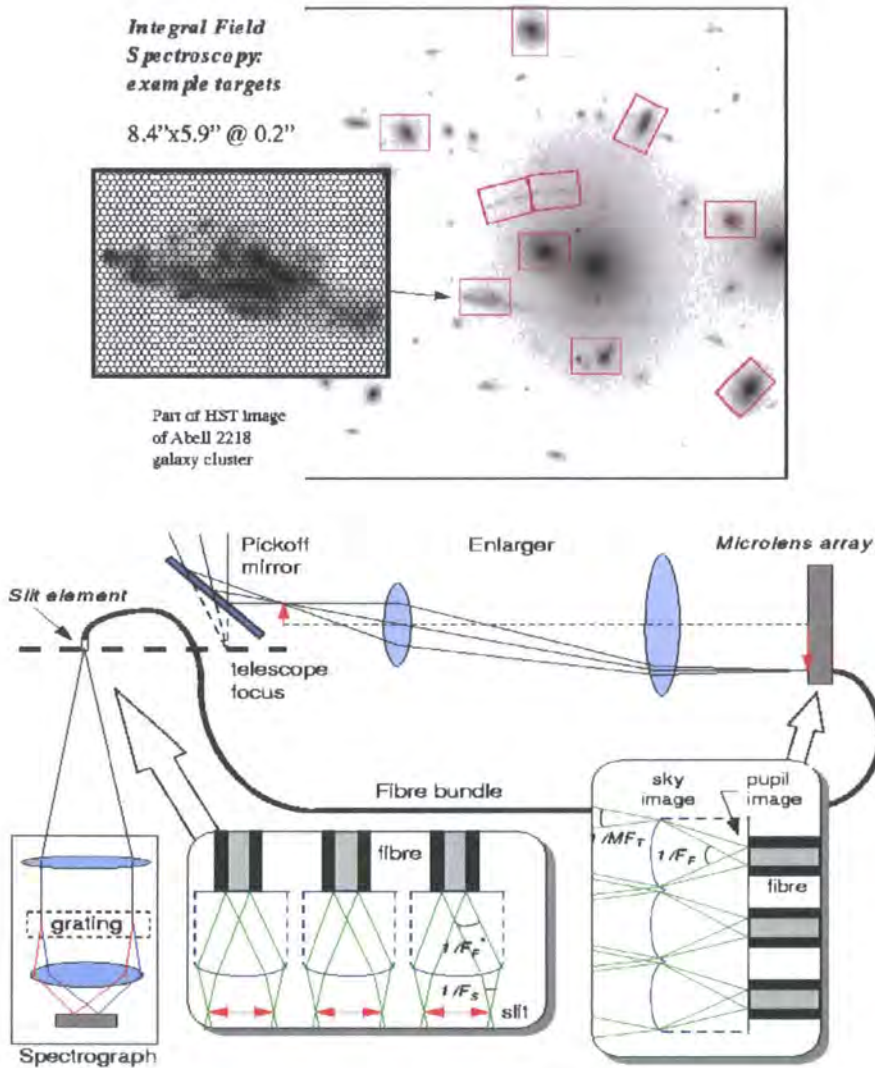


*Figure 1.1 – The basic principles behind fibre fed integral field spectroscopy – Courtesy of CfA.*

There are many integral field instruments now in use throughout the community with examples such the highly successful GMOS project<sup>[1]</sup> and FLAMES<sup>[2]</sup>, VIMOS<sup>[3]</sup>. The convenient transport of light from telescope to instrument is not exclusive from measurement multiplicity. For instance the FMOS instrument, currently being constructed<sup>[4]</sup>, uses fibres for both multiple simultaneous pick off of celestial targets,

\* Or if a redshift is inferred from the data cube, 3D imaging.

(multi-object spectroscopy (MOS)) and the transport of the light from the telescope focus to the spectrographs located on a dedicated platform above the Subaru Nasmyth platform.

Image scrambling is a reference to the ability of an optical fibre to scramble the image at its input to yield a more, but typically not completely, uniform output. Under certain circumstances the time resolved variation in the image over the slit width due to pointing instability, for instance, can cause unwanted uncertainties in the spectrum and the high scrambling of optical fibres can alleviate this problem – See Hunter and Ramsey<sup>[5]</sup> for full treatment of this phenomenon. Image scrambling is also of use in very high dispersion spectroscopy – this is dealt with in more detail in Chapter 7.

Optical fibres themselves are traditionally described by the ray optical model<sup>[6]</sup>, whereby the geometrical approximation is used as shown in Fig 1.2. The light is trapped by total internal reflection within the *step* change in refractive index and ‘bounces’ down the length of the fibre. As the size of the core gets smaller, so fewer modes (range of angles) are supported.

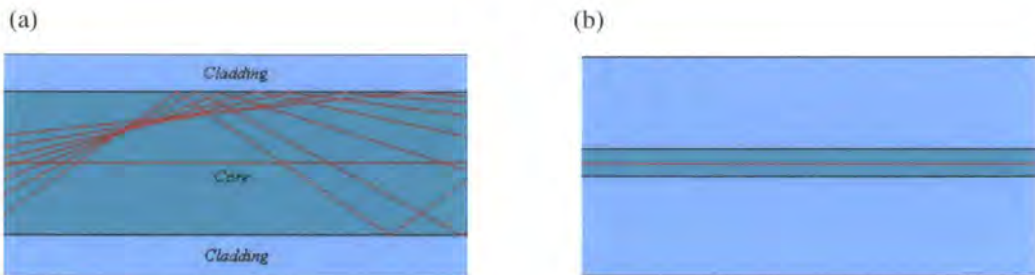


Figure 1.2 – (a) The multi-mode regime, (b) the single-mode regime

At some lower limit the size of the core will only allow the central, axial, ray to propagate but, as is obvious from panel (b), the ray model here is inappropriate (somehow the ray magically finds its way down the fibre axis without touching the sides?) and a full electro-magnetic (EM) field description of the modes is required.

The basic theory of step index optical fibre is introduced in Chapter 2, the results of which will be used throughout the rest of the thesis.

### 1.3 Photonic crystal fibres

As noted in the previous section, step index fibres rely on the step change in refractive index at the core/cladding interface to trap and guide light. However, each separate region, core and cladding is homogeneous. Conversely, photonic crystal fibres (PCF)<sup>[8]</sup> rely on inhomogeneous regions of refractive index in order to provide the guidance mechanism.- Fig 1.3 - The general principles of these fibres are discussed in more detail in Chapter 3, however, the fundamental mechanism that traps light is the coherent scattering of electromagnetic energy between the regularly spaced air holes in a silica (or other base material) substrate.

Light is rejected from the cladding region, by two different mechanisms known as modified total internal reflection (MTIR)<sup>[7]</sup> and the photonic band gap (PBG)<sup>[7]</sup> and trapped and guided in the core. As one might expect the chromatic response of the cladding structure is somewhat different to a homogeneous block of material and thence PCF's are found to behave in new ways that are, as this thesis shows, possibly very useful in astronomy.

The first MTIR fibre was demonstrated by Knight, Birks, St. J. Russell and Atkins in 1996<sup>[8]</sup> and was originally intended to be a photonic band gap fibre. It was quickly realised that the guidance mechanism was MTIR however since the core was found to have a refractive index higher than the cladding and thence an index guided mode appeared. Out of further work on index guiding fibre geometries and manufacturing techniques came the development of the large mode area PCF<sup>[9]</sup>. These are also characterised by a mode field that does not change in size as the wavelength of the incoming light changes but with a core size typically 3-10 times larger than the step index alternative. They are also endlessly single-moded and have useable pass bands that are again typically at least twice that of the step index alternative. LMA fibres are now commercially available in single-mode form and the pass band alone makes them attractive for astronomy. The other properties are also shown to be important as part of the original contribution of this thesis.

In 1998 the first theoretical photonic fibre structure found to demonstrate a photonic bandgap was published by Birks et al<sup>[10]</sup>. Experimental verification of a fibre based photonic band gap, was then demonstrated, by Knight, Birks and St. J Russell<sup>[11]</sup>.

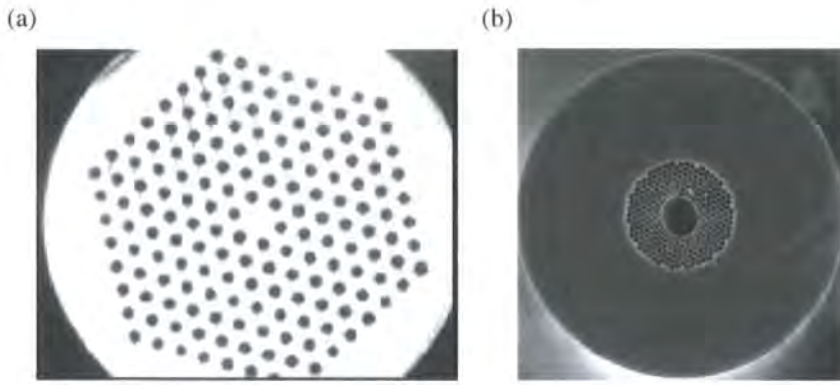


Figure 1.3 - (a) the LMA, MTIR fibre, (b) an air cored PBG guiding fibre

So far in astronomy, single-mode fibres have been used for interferometry and laser beam transport and a few authors have tackled the use of LMA PCF's in this field. Corbett *et al*<sup>[12]</sup>, Corbett & Allington-Smith<sup>[13]</sup>, S Vergnole *et al*<sup>[14]</sup>, Peyrilloux *et al*<sup>[15]</sup>. The application of LMA PCF's to current interferometers is described in Chapter 4.

In the laser beam transport application high power light is transported to the telescope secondary where it is projected onto the sky as laser guide star<sup>[16]</sup>. The advantages over fixed optics are obvious and a PBG fibre was used since the air core is able to carry significantly more power than a silica core without the onset of non-linear effects and in the limit heat damage to the photonic structure.

The use of single-mode fibres in *spectroscopy* is less well defined and although tried before with traditional few mode step index fibres Ge *et al*<sup>[17]</sup>, no work has been done with PCF's. One of the main potential applications in astronomical spectroscopy is to remove the noise from recorded spectra associated with the interference of multiple fibre modes on a very high resolution spectral element Baudrand & Walker<sup>[18]</sup> – this is covered in Chapter 7. One possible advantage of LMA fibres over traditional step index single-mode fibres is that the mode field does not change size with wavelength and hence lenslet-fed IFS *in a single mode* becomes possible, because the diameter of the pupil image placed on the fibre end face also does not change scale with wavelength.. Chapter 5 deals with this subject in some detail.

Multimode PCF's are also available, whereby the core is a very large homogeneous region surrounded by a cladding PCF. This promises extremely high numerical

apertures which would be well matched to the fast primary foci of ELT class telescopes. Although little work has been published to date we are aware of at least one group looking into the focal ratio degradation<sup>[19]</sup> (FRD), throughput and general mechanical performance of these fibres.

Other more advanced photonic crystal fibre types include, non-linear fibres whose most studied application area to date is in the generation of super continua, which might find use in spectroscopic calibration in the lab or even on instrument.

#### **1.4 Photonic Instrumentation**

Microscopic photonic devices (PD), such as integrated optical circuits and photonic crystals are characterised by physical scales typically 2 to 4 orders of magnitude smaller than traditional optical instruments. They have a number of unique properties which make them very attractive to modern astronomy including no internal alignment or maintenance once manufactured, simple deployment due to their small size, avoidance of lossy air/glass interfaces and ease of scaling in manufacture. Generally their operation is described in terms of the optics of the vectorial electromagnetic field rather than the intensity field appropriate for macroscopic devices. To realise instrumentation for extremely large telescopes (ELT's) that is both affordable and efficient is a daunting task. Projected instrument sizes and cost are very large with complex and lossy optical paths. The small size of photonic devices holds out the possibility of reduced size and cost. Furthermore, their ease of deployment and multiplexing via small coherent bundles make them potentially very attractive to massively-multiplexed integral-field spectroscopy – an important requirement for future astronomical facilities. Considering also that many advances in astronomy have been made possible by instrumentation that fully exploits the vectorial electromagnetic field, such as interferometry<sup>[20]</sup> and, more recently, phase apodisation<sup>[21]</sup>, so the potential to revolutionise astronomical instrumentation and explore new regions of observational parameter space is clear.

Many optical components already exist in the form of PD's for common tasks including dispersion and interferometry<sup>[22]</sup>. In astronomy, PD beam-splitters have been used in interferometry for some time<sup>[23]</sup> and new phase-retardation PD's are being

implemented to further simplify these instruments<sup>[24]</sup>. PDs have not yet been used in astronomical spectroscopy but Joss Bland-Hawthorn *et al*<sup>[25]</sup> note that currently available communications spectrometers (Fig 1.4(a)) already have many features attractive to astronomy.

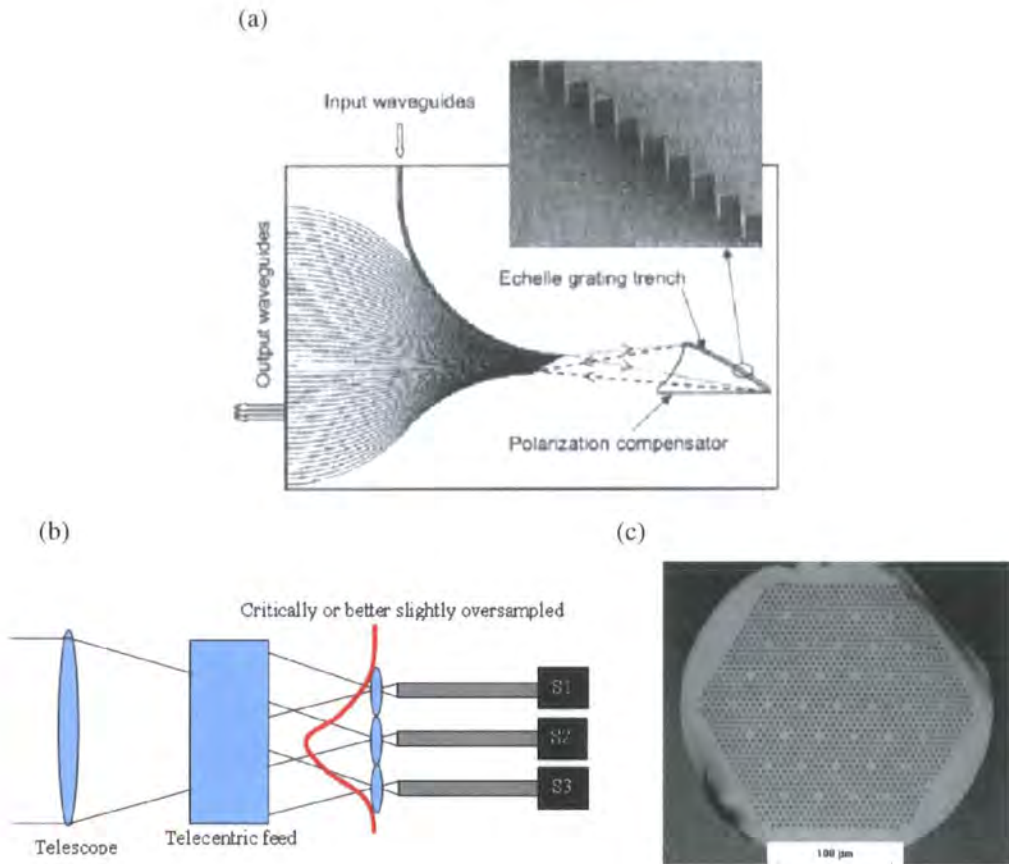


Figure 1.4 – (a) A photonic spectrograph [1], (b) Single-mode array scheme for increased field of view and/or coupling, (c) a multi-core LMA PCF.

However, most of these devices are operated in the single-mode regime. Further to this, the proposed size of the MOMSI instrument<sup>[26]</sup>, for the ESO ELT indicates that photonic instrumentation might be the only way to fully exploit the enormous scientific potential of ELT class facilities and therefore the importance of both photonic instrumentation and single-mode photonic crystal fibres to astronomy is clear.

Previous researchers have derived models<sup>[27]</sup>, and tested the coupling on telescope<sup>[28]</sup> with step index single-mode fibres yielding as much as 44% throughput, in highly AO corrected cases. However, this has required significantly more work than would have

been required in the multimode case. However, overall losses due, for instance, to the number of air/glass interfaces in the optical path in a facility class spectrometer, can lead to a total throughput of 30% or less. (For example 20 air/glass interfaces with  $0.96^{20}$  plus the detector and grating efficiencies). With no air glass interfaces within PD's and losses being reduced as development continues, it is highly likely that PD's and therefore, to some extent single-mode fibres, are going to play a far more prominent role in spectroscopy than has been enjoyed thus far.

Various schemes for efficient coupling are proposed and investigated in this work, particularly in chapters 4 and 5, including for instance the deliberate defocusing of the telescope PSF to better match the coupling efficiency into a single-mode and even perhaps coupling the point spread function (PSF) into multiple single-mode fibres such as the scheme in Fig 1.4(b) utilising specialist fibre arrays such the one shown in Fig 1.4(c). Chapter 5 deals with the coupling for spectroscopy, into single-mode fibres in some detail.

### 1.5 Multimode fibres in modern astronomy.

This thesis also investigates two topics of some interest in multi-moded fibre fed astronomy today. The first is in OH suppressing devices, whereby a multimode fibre is tapered or feathered out into many single-mode fibres. Bragg gratings are then imprinted onto each SM fibre in the array and the whole lot re-fused into a multi-moded output – Figure 6.1. The resulting fibre device is then multi-moded at its ports but with the single-mode performance of the fibre Bragg grating. First proposed by Bland-Hawthorn *et al* <sup>[29]</sup> and demonstrated in the lab by Leon-Saval *et al* <sup>[30]</sup> these devices promise very high atmospheric line<sup>†</sup> rejection for spectroscopy. The number of modes in the SM array has a direct effect on the manufacturability of the device and an analysis of these fibres on telescope is contained in chapter 6.

The other topic is fibre modal noise. When the spectral width of a resolution element on a spectrograph detector is small enough, in  $\lambda$ , such as in very high dispersion

---

<sup>†</sup> This is an atmospheric effect whereby the sky background is dominated by unwanted bright spectral emission lines in the near infra-red due to hydroxyl ions in the upper atmosphere.

applications the modes of the optical fibres that feed the element are seen to partially interfere with each other. This interference pattern changes shape when the fibre is moved, such when the telescope tracks an object on the sky for instance and this causes a photometric uncertainty on each element. Very high spectral resolution applications are typically associated with analysis of line profiles to fractions of percent <sup>[31]</sup> such as planet finding searches. Further, number of echelle based spectrometers are in use already, such as EPSADONS <sup>[32]</sup>, HARPS <sup>[33]</sup> and FOCES <sup>[31]</sup> and with more planned such as PVRS <sup>[34]</sup>, whose contract will be awarded soon and the recently re-proposed WFOS <sup>[35]</sup>, the issues surrounding modal noise are of some contemporary interest.

### ***1.6 Summary of thesis contents***

The uses of traditional multi- and single- mode fibres in astronomy has been covered briefly in this chapter alongside introductions to the new technologies of photonic crystal fibres and photonic instrumentation. Chapters 2 and 3 are an introduction to traditional step index and photonic crystal fibre theory.

Much remains to be understood about how photonic instrumentation might be used to advantage in astronomy including how they are to be fed at the telescope. Coupling analyses in the diffraction limit are useful for finding the extents of the performance envelope but tells us little about what can be expected in natural seeing. The light from an infinitely distant point source reaches the Earth as a plane wave. However, atmospheric turbulence causes changes in the refractive index of the air which itself then causes the planar wavefront to become distorted, that is retarded in phase, yielding a highly non-planar wave at the surface where, generally, the telescope resides. The subsequent image is then badly distorted - Fig 1.6. Worse the turbulent atmosphere is time resolved and an adaptive optics (AO) system <sup>[36]</sup> is required in order to correct as much of the distortion as possible, returning the input wave to the imaging system to something approximating a plane wave.

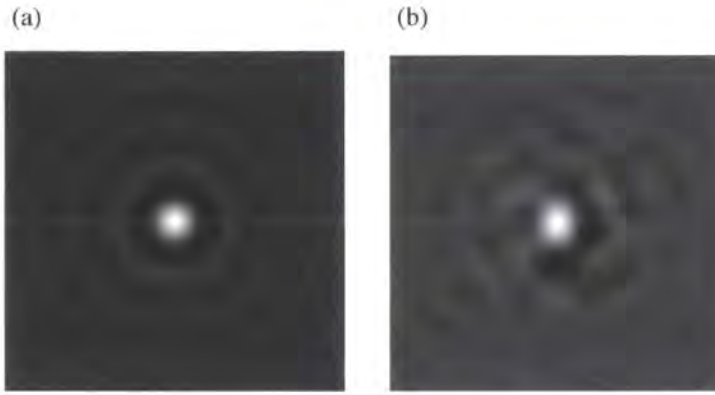


*Figure 1.6 – (a) A diffraction limited (unaberrated) PSF, (b) an atmospherically aberrated PSF. Both in linear grey scale.*

The Centre for Advanced Instrumentation at Durham University is a centre of excellence in the design and construction of AO systems and most importantly here, the modelling of both the atmosphere and the amount of correction applied by model AO systems. Predictions about how these degraded and partially corrected images then couple into optical fibres can be made yielding a far more accurate picture of their on telescope properties. The coupling of atmospherically aberrated telescope PSF's into single-mode photonic crystal fibres is covered in Chapter 4.

The new design parameter space of photonic crystal fibres is also an important new area of research for instrument scientists in astronomy. The most immediate example in this thesis is the ability to feed an LMA fibre with a lenslet due to the wavelength independence of the mode field size. This work will have direct relevance to the application of single moded photonic instruments in astronomy and the fact that Chapter 5 is the largest single chapter in this work should indicate how much there is to learn.

The uses of the atmospheric analysis are not restricted to single-mode fibres, of course. The form, and most specifically the enclosed energy as a function of PSF radius, of the degraded PSF is of singular importance when discussing OH suppressing fibre systems since the number of modes in the single-mode array is directly proportional to the size of the multi-mode fibre core. The total throughput of an OH suppressing fibre is calculated from how much energy in the PSF is vignettted by the core with larger cores increasing coupling but also increasing the manufacturing

complexity of the fibres. Chapter 6 covers this for the two most commonly found cases in astronomy, the direct feed of the Airy pattern into the fibre and when a lenslet is used to place an image of the exit pupil of the telescope on the fibre end face.

Finally, a common theme throughout the preceding sections and, indeed, throughout this work is that, like the single-mode regime, there are many fibre technologies, such as OH suppressing devices and in fact certain properties of normal multi-moded step index fibres such as modal noise, covered in Chapter 7, that are easier to understand in the EM model than the ray model.

Far from being a mature application, then, there is still much new instrument science to be explored in the application of optical fibres in astronomical instrumentation and this thesis goes some way to exemplifying this. I also hope to show, throughout the thesis, that knowledge of *both* the ray optical and EM models for many fibre types is often useful and sometimes necessary even if only to justify the blind use of the ray model.

## 1.7 References

- 1) ‘The GMOS Integral Field Unit: First Integral Field Spectroscopy with an 8m Telescope (Invited Talk)’ JR Allington-Smith *et al*, *Galaxies: The Third Dimension*, ASP Conference Proceedings, Vol. 282. Astronomical Society of the Pacific, p.415 (2002)
- 2) ‘Installation and commissioning of FLAMES, the VLT Multifibre Facility’ Pasquini, L. *et al.*, *The Messenger* 110, 1. (2002)
- 3) ‘VIMOS and NIRMOS multi-object spectrographs for the ESO VLT’, O Le Fevre *et al*, *Proc. SPIE* Vol. 4008, p. 546-557, *Optical and IR Telescope Instrumentation and Detectors* (2000)

- 4) ‘The UK FMOS spectrograph’, G.B. Dalton *et al*, Ground-based and Airborne Instrumentation for Astronomy. Edited by S McLean *et al* Proceedings of the SPIE, Volume **6269** (2006)
- 5) “Scrambling properties of optical fibres and the performance of a double scrambler” T Hunter and L Ramsey, *PASP* **104**, pp. 1244-1251, (1992)
- 6) ‘Optical Waveguide Theory’, A Snyder and JD Love, Kluwer (1983)
- 7) ‘Photonic Crystal Fibres’, A Bjarklev, J Broeng, and AS Bjarklev, Kluwer (2003)
- 8) ‘All-silica single-mode optical fibre with photonic crystal cladding’, J Knight, T Birks, P St J Russell, D Atkins, *Optics letters*, **21**, 19, (1996)
- 9) ‘Large mode area photonic crystal fibre’, J Broeng, S Barkou, A Bjarklev, J Knight, T Birks, RF Cregan, P St. J Russell, J P de Sandro, *IEEE Electronics letters*, **34**, 13 p1347-1348, (1998)
- 10) ‘Full 2-d photonic bandgaps in silica/air structures’, T Birks, P Roberts, P St J Russell, D Atkin, T Shepherd, *IEEE Electronics Letters*, **31** p1941-1943 (1995)
- 11) ‘Photonic band gap guidance in optical fibres’, J Knight, J Broeng, T Birks, P St.J Russell, *Science*, **282**, p1476-1478, November 20<sup>th</sup>, (1998)
- 12) ‘Tip-tilt requirements for coupling starlight into single-mode photonic crystal fibres using a lenslet: - A first analysis’, J Corbett, T Morris, J Allington-Smith, *New Astronomy Reviews*, **49**, Iss.10-12, p.675-680, (2005).
- 13) ‘Coupling starlight into single-mode photonic crystal fibre using a field lens’, J Corbett and J Allington-Smith, *Optics Express*, Vol. **13**, Iss. 17 pp: 6527-6540 (2005)

- 14) 'Test of photonic crystal fiber in broadband interferometry' S Vergnole, L Delage, F Reynaud, L Labonte, P Roy, G Melin and L Gasca, *Appl. Optics* **44**, 2496 (2005)
- 15) 'Evaluation of photonic crystal fibre potential for fibre linked version of stellar interferometer' A Peyrilloux, D Pagnoux, F Raynaud. *Interferometry for Optical Astronomy II. SPIE* **4838** p. 1334-1340 (2003)
- 16) '*Laser guide-star systems for astronomical applications*', R Parenti, and R Sasiela, , *J. Opt. Sci. Am. A* **11** p288-309 (1994)
- 17) 'Optical spectroscopy with a near single-mode fibre feed and adaptive optics', J Ge, R Angel C helton *Proc. SPIE Vol 3355* p253-263, *Optical Astronomical Instrumentation* (1998)
- 18) Ramsey L., Barden S., *ASP Conference series – Fibre optics in astronomy*, 3 (1988)
- 19) 'Modal noise in high-resolution fibre-fed spectra: A study and simple cure'. J Baudrand & GH Walker. *PASP* **113** : 851-858 (2001)
- 20) 'Measurement of the diameter of  $\alpha$  Orionis with the interferometer' AA Michelson and FG Pease, *Astrophys. J* **53**, 249–259 (1921)
- 21) 'Exoplanets imaging with a Phase-Induced Amplitude Apodization Coronagraph - I. Principle', O Guyon, EA Pluzhnik, R Galicher, F Martinache, ST Ridgway, RA Woodruff, , *Astrophys.J.* **622** 744 (2005)
- 22) 'Modern trends in microstructures and integrated optics for communication, sensing and actuation', M. Tabib-Azar, G. Beheim, , *Opt. Eng.* **36**(5), 1307-1318 (1997)

- 23) 'Integrated optics for astronomical interferometry' F Malbet, P Kern, I Schanen-Duport, JP Berger, K Rousselet-Perraut, and P Benech, *Astronomy and Astrophysics, Supplement series*, **138** 135-145 (1999)
- 24) 'Characterization of 4-beam integrated optics combiners for the VLTI-VITRUV instrument', M Benisty, , *SPIE* (2006), *in press*
- 25) 'Instruments without optics: an integrated photonic spectrograph', J Bland-Hawthorn, A Horton, , *Volume 6269*, pp. 62690N (2006)
- 26) 'A multi-object multi-field spectrometer and imager for a European ELT', C Evans, *Ground-based and Airborne Instrumentation for Astronomy. SPIE, Volume 6269* (2006)
- 27) 'Coupling starlight into single-mode fibres', S Shaklan, F Roddier, *Appl. Optics*, **27**, 2334 (1987)
- 28) 'Properties of fibre optics for application in astronomical interferometry', R Rohloff & C Leinert, *Applied Optics*, Vol **30** No.34 (1991)
- 29) 'New approach to atmospheric OH suppression using an aperiodic fibre Bragg grating', Bland-Hawthorn J, Englund M and Edvell G, *Opt. Exp* **12**, 902 (2005)
- 30) 'Multimoded fiber devices with singlemode performance', SG Leon-Saval, T Birks, J Bland-Hawthorn and M Englund, *Opt. Lett.* **30**, 2545. (2005)
- 31) 'FOCES - a fibre optics Cassegrain échelle spectrograph', MJ Pfeiffer *et al*, *Astron. Astrophys. Suppl. Ser.* **130**, 381-393 (1997)
- 32) 'ESPaDOnS; an exhelle spectro-polarimetric device for the observation of stars', N Manset *et al*, *Polarimetry in Astronomy. Edited by Silvano Fineschi . Proceedings of the SPIE, Volume 4843*, pp. 425-436 (2003)

- 33) 'The exoplanet hunter HARPS: unequalled accuracy and perspectives toward 1 cm s<sup>-1</sup> precision', C Lovis *et al*, Ground-based and Airborne Instrumentation for Astronomy. Edited by IS McLean M Iye Proceedings of the SPIE, Volume **6269** (2006).
- 34) PVRS – Precision Radial Velocity Spectrograph –  
[www.roe.ac.uk/ukatc/projects/prvs](http://www.roe.ac.uk/ukatc/projects/prvs)
- 35) 'Instrumentation and Technology Development at the Anglo-Australian Observatory', S Barden and J Bland-Hawthorn, American Astronomical Society Meeting 207, No. 173.17; Bulletin of the American Astronomical Society, Vol. **37**, p.1441 (2006)
- 36) Adaptive Optics for Astronomical Telescopes', John W. Hardy, Oxford University Press. (1998)

# Chapter 2

## *Step index fibres*

### **2.1 Introduction**

The most commonly used type of optical fibre in astronomy are step index fibres. As Fig 2.1 shows they are characterised by a homogeneous core and cladding each with a different refractive index. The core refractive index (RI),  $n_{core}$  is higher than that of the cladding,  $n_{cladding}$  and light is trapped and guided along the fibre by total internal reflection<sup>[1]</sup>.

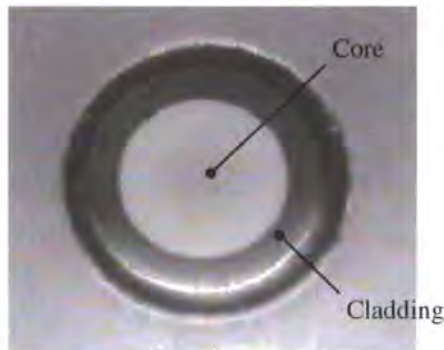


*Figure 2.1 – The polished end of a 100µm diameter core step index optical fibre.*

In this chapter the ray optical and electromagnetic models of guidance are introduced and compared in sections 2.2 and 2.3 respectively. Specifically, the single-mode regime is described in section 2.3.6 and various results useful throughout the rest of this work are introduced where relevant. Section 2.4 deals with the coupling integral, a mathematical device useful for modelling optical fibres as part of an optical system with some experimental verification of the integral shown in section 2.4.2.

2.2 The ray optical model

2.2.1 The guidance mechanism

The ray optical model is generally the simplest way to understand how light is trapped and guided along a step index optical fibre and in fact when many modes are supported within the fibre it is also the most expedient.

With reference to Fig 2.2, Snell’s law at a planar interface tells us that <sup>[2]</sup>

$$n_i \sin \theta_i = n_t \sin \theta_t \tag{2.1}$$

At the critical angle  $\theta_t = \theta_c$ ,  $\theta_i = \pi/2$  and  $\sin \theta_i = n_t/n_i$ . For  $\theta_i > \theta_c$ , the light is totally internally reflected and the ray is trapped within the region of higher RI.

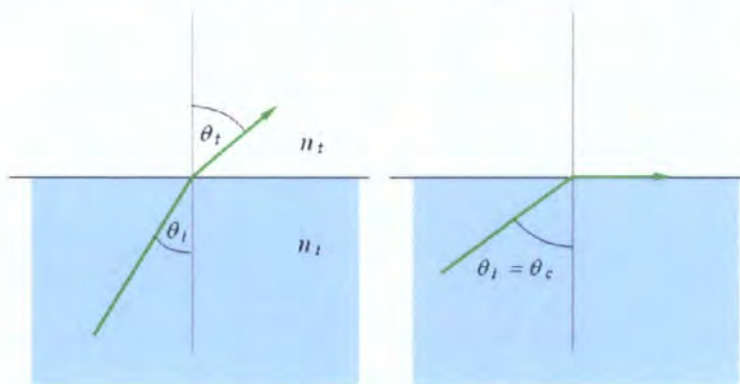


Figure 2.2 – Snell’s law and total internal reflection

When the geometry in Fig 2.2 is wrapped around to form a cylinder, light can be trapped within a region of higher RI, the core, by a cladding region of lower RI thereby creating a step index optical fibre.

2.2.2 Types of ray mode

There are two types of ray that can travel along a step index optical fibre as shown in Fig 2.3. Meridional rays pass through the axis of the fibre and by symmetry are then (and assuming a perfectly straight fibre) trapped to do so for the entire length of the fibre. Each meridional mode is then characterised by only the angle it makes with the axis,  $\theta_z$ . Skew rays, however, are characterised by two angles,  $\theta_z$ , as in the meridional

case and  $\phi$ , the angle that the ray makes with a tangent to the (circular) boundary in the (x-y) plane<sup>[1]</sup>.

As Fig 2.3 shows skew rays cannot pass through the centre of the fibre, instead they rotate about the axis as they propagate along the fibre, with the point of shortest distance between the ray and the axis tracing out a circle. If the circle has zero radius, the mode passes through the axis and the ray, is then, meridional.

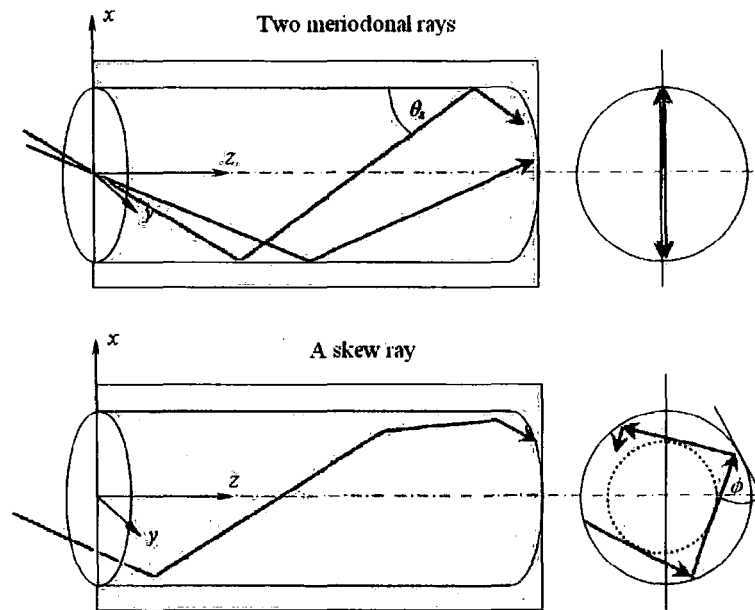


Figure 2.3 – The ray optical model. Each  $(\theta_z, \phi)$  corresponds to a different mode.

Snyder and Love<sup>[1]</sup> show that the ray transit time, the time taken for a ray to travel some given length,  $L$  of fibre is dependent only on  $\theta_z$  and specifically not on  $\phi$ . Hence any correlation between the ray optical and EM models must take this into account.

### 2.2.3 The numerical aperture

The largest angle that the ray can make with the core/cladding surface normal is the critical angle for total internal reflection if the ray is to be guided along the fibre.  $\theta_z$  is traditionally defined with respect to the fibre axis and hence total internal reflection

occurs for  $\cos \theta_z = \frac{n_{cladding}}{n_{core}}$ <sup>[2]</sup>.

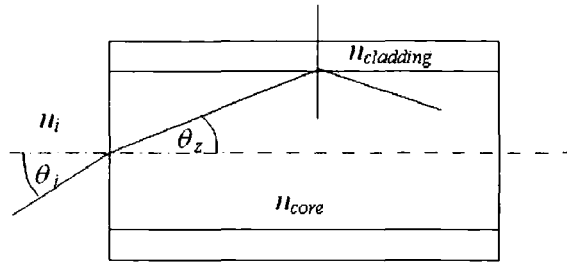


*Figure 2.4 – The numerical aperture*

At the input interface,  $n_i \sin \theta_i = n_{core} \sin \theta_z$  and using the trig identity  $\cos \theta = \sqrt{1 - \sin^2 \theta}$ , substituting and rearranging yields,

$$\Theta = n_i \sin \theta_i = \sqrt{n_{core}^2 - n_{cladding}^2} \tag{2.2}$$

The quantity  $\Theta$  is known as the numerical aperture and is used to describe the largest input angle in region  $n_i$ , supported, i.e. bound, within the fibre.

*2.2.4 Ray optical model comment*

The ray optical model assumes that a continuum of rays exists between  $\theta_i = 0$  and  $\theta_i = \Theta$  and when the fibre supports many modes this will be shown to be approximately true. However, when the fibre supports only a few modes the ray optical model becomes less accurate and indeed in the limit of single-mode guidance when only one mode is supported the model is wholly inappropriate. This is commented upon further in the remainder of this chapter and specifically in Chapter 6.

**2.3 The electromagnetic mode model**

In this section the electromagnetic (EM) modes of step index optical fibres are described and derived. Since the EM modes are solutions of Maxwell’s equations subject to the step index boundary conditions then they should be considered to be a more fundamental description of the guidance of energy by the fibre. By comparison, the ray optical model is an approximate abstraction, albeit quite an accurate one when many modes are supported.

2.3.1 Some basic properties of EM modes

Some basic results are presented in this section for use in later sections and chapters.

The geometry described by Fig 2.5, is used throughout.

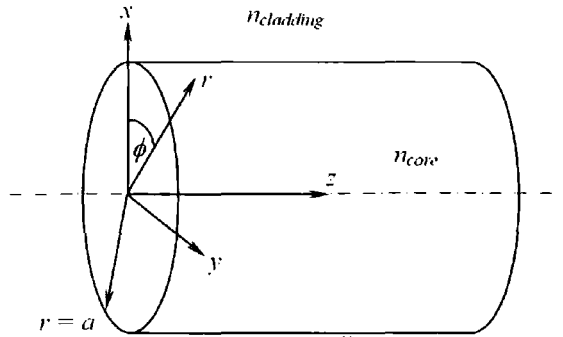


Figure 2.5 – The fibre geometry

Each mode,  $j$ , of a  $z$ -invariant<sup>‡</sup> dielectric waveguide is expressible<sup>[1]</sup> as

$$\mathbf{E}_j(x, y, z) = \mathbf{e}_j(x, y) \exp(i\beta_j z) \quad (2.3)$$

where  $\beta$  is known as the propagation constant. Therefore combining the longitudinal and temporal  $\exp(-i\omega t)$  variations we see that each modal field  $\mathbf{e}_j$  varies as  $e^{i(\beta_j z - \omega t)}$ . The distance between two identical points on the wavefront is given by  $\beta_j \Delta z = 2\pi$  and the time taken for the wave to have travelled this distance is  $\omega \Delta t = 2\pi$ . The ratio of these gives the modal phase velocity given by,

$$v_{pj} = \frac{\omega}{\beta_j} \quad (2.4)$$

This quantity is the speed at which the wavefront of the mode travels along the waveguide when excited by a single monochromatic component. When the fibre is used to transmit information the sinusoidal component is modulated implying that a small spread of wavelengths must exist to form a wavepacket. This wave envelope then travels at the modal group velocity given by

---

<sup>‡</sup> i.e. end effects are ignored by assuming the fibre to be infinite in extent in the  $z$ -direction.

$$v_{gj} = \frac{d\omega}{d\beta_j} \quad (2.5)$$

if  $d\omega$  is small enough for  $\Delta\omega/\Delta\beta \approx d\omega/d\beta$ .

As we shall see, each mode is characterised by a different value of  $\beta$ . Further, different modes have different group delays (the time taken for the mode to traverse the length,  $L$  of the fibre), therefore  $L/v_{gj}$  is analogous to the ray transit time. Since each mode travels with a different speed along the waveguide then any pulse of light used to excite the fibre will be distorted in (temporal) shape at the fibre output. This effect is known as *intermodal dispersion* and, as described in chapter 7, the lack of sufficient intermodal dispersion with respect to the coherence time of the supported pulse is the cause of modal noise in high dispersion fibre fed spectroscopy.

A range of allowed propagation constants,  $\beta_j$ , for the fibre can be derived from Eq.(2.4) on physical grounds<sup>[1]</sup>. The maximum value of refractive index within the fibre is  $n_{core}$  and therefore the minimum possible phase velocity is  $c/n_{core}$ . Conversely, the minimum refractive index is  $n_{cladding}$ . Now it is possible for the phase velocity of the mode to exceed  $c/n_{cladding}$ , but this means that energy is being lost from the wavefront, radiating away within the cladding, into radiation modes. These are modes that do not approach zero as the radial distance from the fibre core approaches infinity and taken as a whole cause energy to radiate away from the fibre core. Thence for truly bound modes,  $v_{core} < v_{mode} < v_{cladding}$  and hence

$$n_{cladding}k < \beta \leq n_{core}k \quad (2.6)$$

In order to make the equations governing EM modes dimensionless and, indeed, to conveniently and completely describe the state of the fibre, the  $V$  parameter and associated modal parameters  $U$  and  $W$  are derived for later use as,

$$V = ka\sqrt{n_{core}^2 - n_{cladding}^2} \equiv ka\Theta \quad (2.7)$$

$$U_j = a\sqrt{k^2 n_{core}^2 - \beta_j^2} \quad (2.8)$$

$$W_j = a\sqrt{\beta_j^2 - k^2 n_{cladding}^2} \quad (2.9)$$

so that  $V^2 = U_j^2 + W_j^2$ .

### 2.3.2 Using the scalar wave equation

Following, closely, the analysis given in reference [1], by assuming that the separable form of the modal fields, Eq.2.3, is valid, that no sources (currents or free charges) exist within the fibre and that Eq.(2.3) is decomposed in Cartesian form,  $\mathbf{e}_j = e_{xj}(x, y)\hat{x} + e_{yj}(x, y)\hat{y} + e_{zj}(x, y)\hat{z}$ , then the wave equation can be expressed as

$$\left(\nabla_t^2 + n(x, y)^2 k^2 - \beta_j^2\right)\mathbf{e}_j = -\left(\nabla_t + i\beta_j\hat{z}\right)\left(\mathbf{e}_{ij} \cdot \nabla_t \ln n(x, y)^2\right) \quad (2.10)$$

where  $\nabla^2 \Psi = \nabla_t \cdot (\nabla_t \Psi) - \nabla_t \times (\nabla_t \times \Psi)$ ,  $\nabla_t \cdot \Psi = \frac{\partial \Psi_x}{\partial x} + \frac{\partial \Psi_y}{\partial y}$ ,  $\nabla_t \Psi = \frac{\partial \Psi}{\partial x} \hat{x} + \frac{\partial \Psi}{\partial y} \hat{y}$

All terms in Eq.(2.10) involving  $\nabla_t \ln n(x, y)^2$  are zero valued everywhere except at the core/cladding boundary. However, if the wave equation is solved in each homogeneous region (i.e. separately in core and cladding) and the boundary conditions at the interface observed then we need only find solutions of the homogeneous equation,

$$\left(\nabla_t^2 + n(x, y)^2 k^2 - \beta_j^2\right)\mathbf{e}_j = 0 \quad (2.11)$$

where  $\nabla_t^2 \Psi = \frac{\partial^2 \Psi}{\partial x^2} + \frac{\partial^2 \Psi}{\partial y^2} + \frac{\partial^2 \Psi}{\partial z^2}$ . Most fibres used in astronomy are commercially

available ‘weakly guiding’ fibres meaning that the difference between the core and cladding refractive indices is very small. The drawing process used to manufacture optical fibres causes tiny density fluctuations in the refractive index of the glass which are small in size with comparison to the illuminating wavelengths typically guided by optical fibres. Hence scattering of the light about these fluctuations occurs isotropically in direction – Rayleigh scattering. The increased RI in the core is generally achieved by doping the virgin cladding material but this increases the micro

RI variations and therefore Rayleigh scattering losses are reduced by minimising the core-cladding RI difference.

Further simplification is possible in the weakly guiding regime. Even though in the fully vectorial case neither  $e_{zj}$  nor  $h_{zj}$  are generally zero for most modes (see section 2.3.4) assuming that  $n_{core} \approx n_{cladding}$  then the core and cladding taken together are almost a homogeneous region of space. Therefore the solutions of the wave equation Eq.(2.11) are approximately plane waves, travelling along  $z$  but with no  $z$ -component and we can therefore approximately specify the mode using only the transverse field,

$$\mathbf{e}_j = e_{xj}(x, y)\hat{\mathbf{x}} + e_{yj}(x, y)\hat{\mathbf{y}} \quad (2.12)$$

and therefore we look for solutions of the scalar wave equation,

$$\left[ \nabla_t^2 + n(x, y)^2 k^2 - \beta^2 \right] \varphi = 0 \quad (2.13)$$

where  $\varphi$  is either  $e_{xj}$  or  $e_{yj}$ .

To summarise, solving the vectorial wave equation Eq.(2.10) can be sidestepped by solving the homogeneous equation (2.11) in each region of refractive index and then imposing the boundary conditions at the core/cladding interface. Further, the fields of weakly guiding optical fibres have a tiny  $z$ -directed field component. This component can thus be ignored reducing a three dimensional Eq.(2.11) problem to two, Eq.(2.13)

### 2.3.3 *The solution of the scalar wave equation in the step index case*

If  $\nabla_t^2$  is expressed in cylindrical-polar coordinates,  $\rho$  and  $\phi$ , there are two separable solutions of Eq.(2.13) for each value of  $\beta$ . These are,

$$\begin{aligned} \Psi &= f_l(r) \sin l\phi \\ \Psi &= f_l(r) \cos l\phi \end{aligned} \quad (2.14)$$

where  $f_l$  satisfies the second order homogeneous equation,

$$\left( \frac{d^2}{dR^2} + \frac{1}{R} \frac{d}{dR} - \frac{l^2}{R^2} + U^2 - V^2 g(R) \right) f_l(R) = 0 \quad (2.15)$$

$U$  and  $V$  were defined in section 2.3 and  $R = r/a$ .  $g(R)$  is the normalised refractive index profile <sup>[1]</sup>.  $l$  is an arbitrary integer. By solving this second equation separately in core and cladding (i.e. where  $g(R) = 0$  for  $0 \leq R < 1$  and  $g(R) = 1$  for  $1 < R < \infty$ ) yields,

$$\begin{aligned} f_{core,l} &= \frac{J_l(UR)}{J_l(U)} & 0 \leq R < 1 \\ f_{cladding,l} &= \frac{K_l(WR)}{K_l(W)} & 1 \leq R < \infty \end{aligned} \quad (2.16)$$

where  $J_l$  is the Bessel function of the first kind (order  $l$ ) and  $K_l$  the modified Bessel function of the second kind. Since  $\varphi$  is chosen arbitrarily to be either  $e_x$  or  $e_y$  then there are four vectorial modal solutions per  $\beta$  in the scalar model. These are,

$$\begin{aligned} \mathbf{e}_1 &= f_l(R)(\cos l\phi\hat{\mathbf{x}} - \sin l\phi\hat{\mathbf{y}}) \\ \mathbf{e}_2 &= f_l(R)(\cos l\phi\hat{\mathbf{x}} + \sin l\phi\hat{\mathbf{y}}) \\ \mathbf{e}_3 &= f_l(R)(\sin l\phi\hat{\mathbf{y}} + \cos l\phi\hat{\mathbf{x}}) \\ \mathbf{e}_4 &= f_l(R)(\sin l\phi\hat{\mathbf{y}} - \cos l\phi\hat{\mathbf{x}}) \end{aligned} \quad (2.17)$$

Applying the condition that  $f_l$  and  $df_l/dR$  must be continuous across the boundary at  $R = 1$  yields an eigenvalue equation that must be satisfied for each valid mode. However, more physically, Maxwell's equations demand that the  $z$ -component is continuous across the boundary. Even though we have approximated this component as zero valued, in the full analysis, of course, it generally is not.  $e_z$  within the core and cladding are given by,

$$e_z = \begin{cases} U \frac{J_{l+1}(U)}{J_l(U)} p(\phi)q(V, n_{core}, n_{clad}) & 0 \leq R < 1 \\ W \frac{K_{l+1}(W)}{K_l(W)} p(\phi)q(V, n_{core}, n_{clad}) & 1 < R < \infty \end{cases} \quad (2.18)$$

where  $p$  and  $q$  are functions of the shown variables. Thence, imposing continuity at  $R$ , the equation for the valid eigenvalues,  $U$ , is,

$$U \frac{J_{l+1}(U)}{J_l(U)} = W \frac{K_{l+1}(W)}{K_l(W)} \quad (2.19)$$

Equation (2.19) can only be solved numerically and computationally this is achieved by first setting the  $V$  value in question and then stepping over  $U$  values, increasing from zero, at some desired resolution for all  $U < V$  and inspecting for zeros.  $U = V$  implies  $\beta = kn_{cladding}$  and all modes, except the lowest order mode, the fundamental, are cut-off, i.e., they are not supported at and below this value of  $U$ . There  $m$  solutions, labelled, 1,2,3..... $m$ , of Eq.(2.19) at each value of  $l$ . Figure 2.6 is a plot of valid  $U(V)$ . The relationship between  $l$ ,  $m$  and the traditional mode nomenclature is dealt with in the next section.

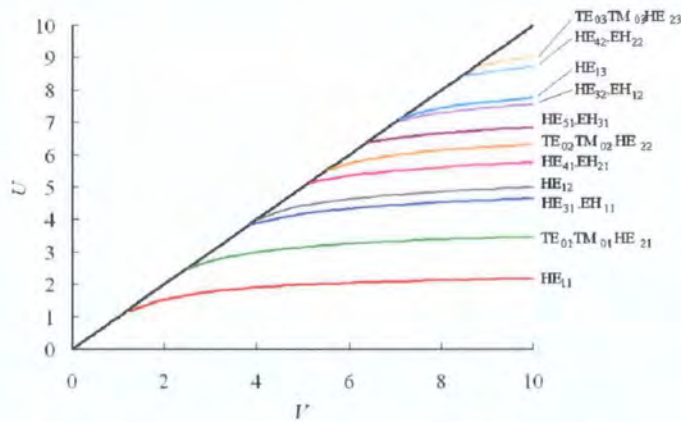


Figure 2.6 – A plot  $U$  against  $V$  including the mode nomenclature of each supported mode.

From Eq.(2.7) as the diameter,  $(2a)$  or the numerical aperture,  $\Theta$  of the fibre increase and/or the wavelength,  $\lambda$  of the guided light decreases then so the  $V$  value increases.

From Fig 2.6 as  $V$  increases so more modes are supported appealing to the physical notion that smaller wavelengths in ‘larger’ waveguides will increase the total number of supported modes.

*2.3.4 Description of EM modes*

With reference to Fig 2.6 and the preceding arguments, the mode nomenclature is traditionally denoted as given in Table 2.1. Generally, the HE modes are designated by  $(l+1,m)$  and the EH by  $(l-1,m)$ . In the  $l=0$  case the HE and EH are degenerate yielding only the  $HE_{lm}$  modes. The  $l=1$  modes are described below.

$l = 0$	Mode number	Transverse mode field	Comment
HE (even)	$l+1, m$	$e_1 = e_2$	
HE (odd)	$l+1, m$	$e_3 = e_4$	
$l = 1$	Mode number	Mode field	Comment
HE (even)	$l+1, m$	$e_1$	
HE (odd)	$l+1, m$	$e_3$	
TM EH (even)	$l-1, m$	$e_2$	Vectorial $h_z = 0$
TE EH (odd)	$l-1, m$	$e_4$	Vectorial $e_z = 0$
$l > 1$	Mode number	Mode field	Comment
HE (even)	$l+1, m$	$e_1$	
HE (odd)	$l+1, m$	$e_3$	
EH (even)	$l-1, m$	$e_2$	
EH (odd)	$l-1, m$	$e_4$	

*Table 2.1 – Mode labelling in step index optical fibres. – See [1] for historical and technical reasons for this nomenclature.*

The TE and TM, transverse electric and transverse magnetic, respectively are so named because they satisfy even the fully vectorial wave equation, Eq.(2.10) with a zero  $z$ -component and are therefore, as the name suggests, fully transverse. They are a special case of the EH mode type when  $l = 1$ . At this point we can align the results of the EM analysis with the ray optical model.

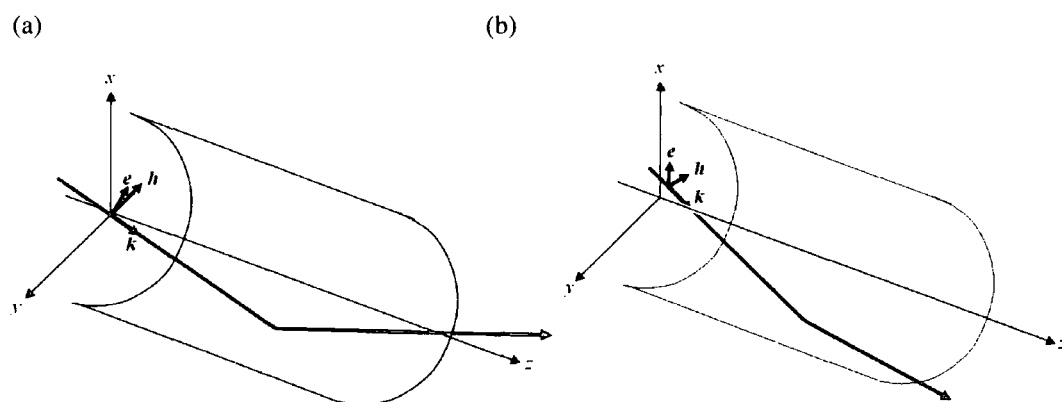


Figure 2-7 – (a) A meridional ray, (b) A skew ray.

Rays, when considered as local plane waves within the fibre, must be characterised by  $\mathbf{e}$ ,  $\mathbf{h}$  and  $\mathbf{k}$  vectors that are orthogonal to each other. Therefore in the meridional case, either  $\mathbf{e}$  or  $\mathbf{h}$  (as shown in Fig 2.7(a)) must be confined to the (x-y) plane. i.e.  $e_z = 0$  or  $h_z = 0$ . In the skew ray case, panel (b), no components of  $\mathbf{e}$  or  $\mathbf{h}$  are generally zero valued. Hence we can see immediately that meridional rays are TE, TM modes and skew rays are all other HE, EH. By inspecting Fig 2.6 it is obvious that many more skew rays are supported within an optical fibre than meridional. As a very rough approximation, there are 6 transverse modes and 32 (odd+even) skew modes in Fig 2.6 at  $V=10$ , which in chapter 5 is shown as yielding a good geometrical approximation and so the ratio of meridional to skew is  $\sim 1/5$ .

To further exemplify section 2.3.3, the field solutions of some lower order modes are found in Fig 2.8. Here the component field amplitudes are shown together with the total field intensity and in some cases the transverse vectorial field itself. Note that the field of designation  $l,m$  has  $2l$  azimuthal extrema and  $m$  radial extrema. Note further that as the order of the mode increases so the spatial frequencies that go to make the 'image' of the mode reduce in wavelength. i.e. at higher modal orders, smaller spatial frequencies are required in order to decompose the image. This description will be revisited in chapter 5.

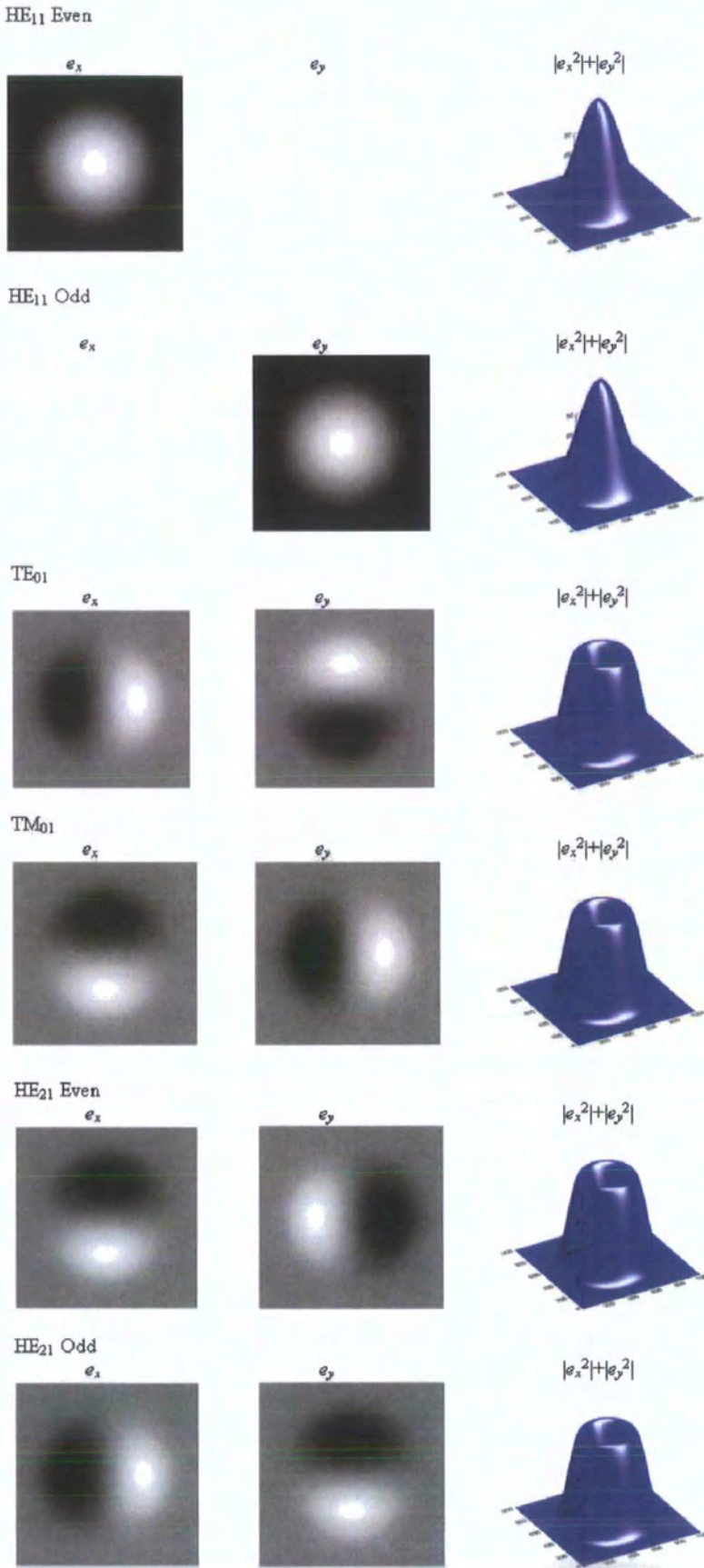


Fig 2.8 continued overleaf.....

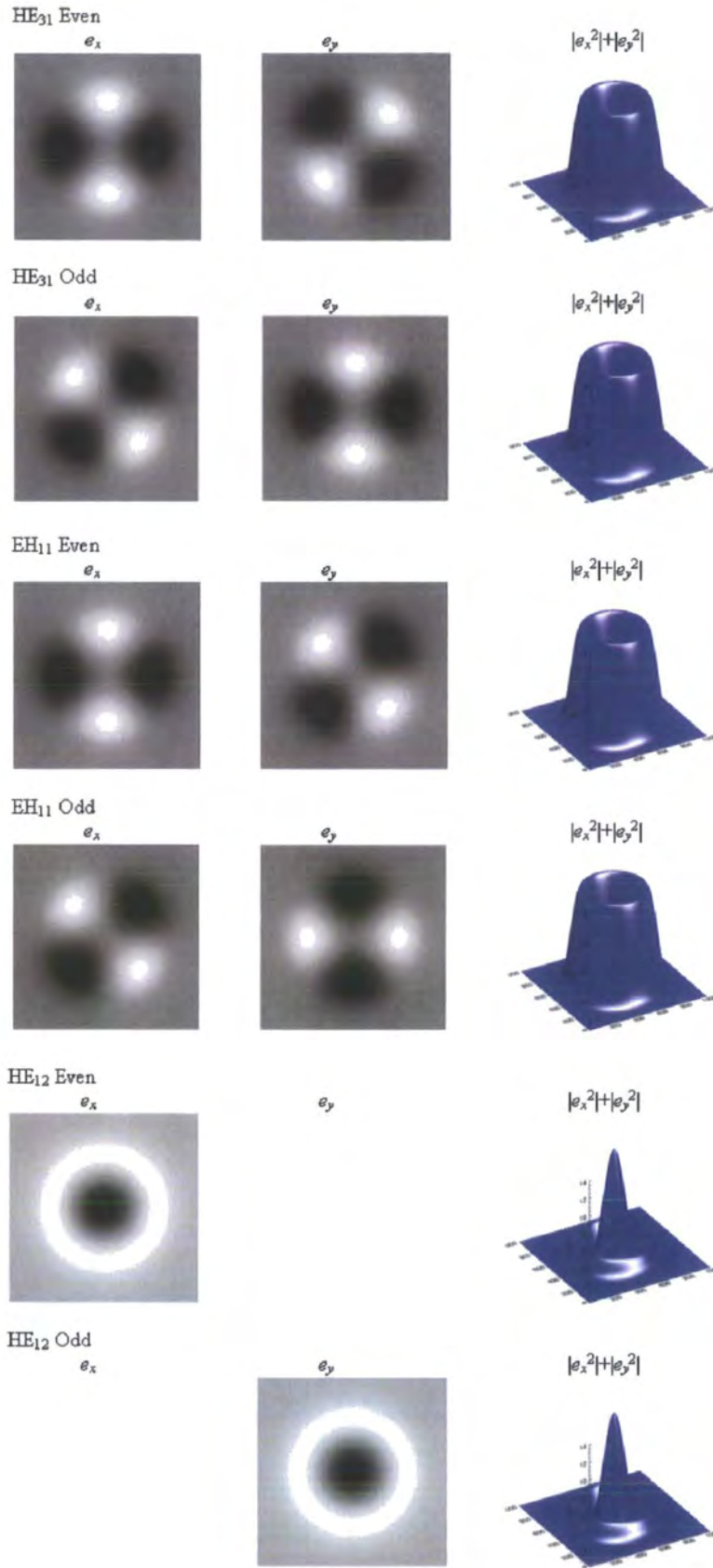


Figure 2.8 – Mode fields and intensity plots for all modes supported at  $V=6$ .

### 2.3.5 Comparison with the ray optical model

A direct and rigorous comparison of the ray and EM models is possible and involves decomposing the modes into families of rays<sup>[1]</sup>. However, the simplest clues to the relationship exist in the form of the EM mode itself and rules derived for the propagation constant  $\beta$  in section 2.3.1.

In the ray optical case, where, once again the ray is modelled as a local plane wave as in Fig 2.7, equiphasal surfaces of the plane wave must exist normally to  $\mathbf{k}$ . Hence equiphasal surfaces in the direction of  $z$  must be found at  $\mathbf{k} \cdot \hat{\mu}_z$  where  $\hat{\mu}_z$  is the  $z$ -directed unit vector. However, from Eq.(2.3) equiphasal surfaces of the EM mode exist at intervals of  $\beta$  along the  $z$ -axis and therefore,

$$\beta = |k|n_{core}\cos\theta_z \quad (2.20)$$

Since each mode is characterised by a separate  $\beta$  then each EM mode is also characterised by a single  $\theta_z$ . To check that this makes physical sense note the following. By substituting Eq.(2.7) and Eq.(2.8) into Eq. (2.20), the following relationship exists<sup>[1]</sup>,

$$U = V \frac{\sin\theta_z}{\sin\Theta} \quad (2.21)$$

so that when  $U = V$  Eq.(2.21) implies that  $\theta_z = \Theta$  and the ray in question is at the numerical aperture of the fibre. For values of  $U < V$  the angles are smaller than  $\theta_c$ .

Further note that total internal reflection occurs when  $n_{cladding} = n_{core}\cos\theta_c$ . Hence, when  $\theta_z = \theta_c$  from Eq. (2.20)  $\beta = |k|n_{cladding}$ , the known lower limit on  $\beta$ , and therefore upper limit on  $\theta_z$  by Eq.(2.20) from the EM model in section 2.3.1.

However, perhaps the most striking example of the correspondence is shown in Chapter 6 – Note particularly the results of section 6.4.1.

It is worth noting that it is only at the cut-off of some mode that a mode exists at the numerical aperture of the fibre since it is only then that  $U=V$ . Also at lower values of  $V$ , the modes are more widely spaced in  $U$  and therefore in  $\theta$  and this is why the ray optical model, when applied to fibres that support only a few modes, implies preferred ray optical directions. These directions are associated with the EM modes directions supported within the fibre.

Finally note that the ray transit time was stated in section 2.2.2 to be dependent on  $\theta_z$  only. By inspection of equations (2.5) and (2.20) we see that this is also true of the EM model.

### 2.3.6 *The single-mode regime*

From Fig 2.6 if  $V < 2.405$ , then the fibre becomes single-moded. Only the fundamental doublet, (HE<sub>11</sub> – Odd and Even) is supported within the waveguide and the geometrical model is entirely inappropriate. Comments in chapter 1 should indicate the importance of this regime to astronomy and chapters 4, 5 and 7 will cover this in far more detail. For now, a brief description of how the mode behaves as the  $V$  parameter varies will suffice.

The mode itself can be well modelled by a Gaussian distribution <sup>[3]</sup> with an RMS width,  $r_o$ , of

$$r_o = \frac{a}{\sqrt{2 \ln V}} \tag{2.22}$$

This variation is of particular significance in chapters 3,4 and 5 when dealing with coupling light into single-mode fibres.

As noted in section 2.3.3 as the  $V$  value increases/decreases, more/less modes are supported within the waveguide. But what effect does varying  $V$  have on the single fundamental mode? Fig 2.9 shows that as  $V$  reduces in value the mode spreads out into the cladding.

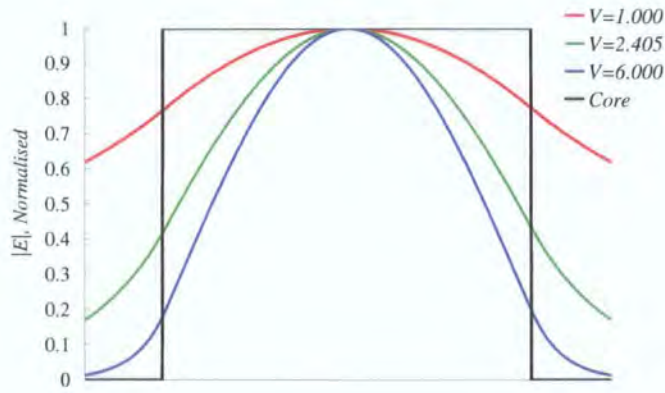


Figure 2.9 The variation in Gaussian field ‘spot size’ with  $V$ . Computed using the results of section 2.3.3

The waveguide is less able to confine longer wavelengths for the same  $\Theta$  and  $a$ .

### 2.4 The coupling integral

In order to model how optical fibres are used in astronomy both the ray and EM models are required. Coupling into the fibre in the ray model is trivial since the fibre acts as a macroscopic optical component. Even focal ratio degradation <sup>[4-6]</sup> can be described (and to *some* extent) explained using the ray model. However, in the single-mode regime and for some few-mode and multi-mode applications the coupling of the incident light in the EM model is required. In this section the coupling formalism is derived that will be used throughout the rest of this work.

#### 2.4.1.1 Derivation of the coupling integral

The problem at hand is that of coupling an arbitrary monochromatic external field into the optical waveguide with its end face cut perpendicularly to its optical axis, as shown in figure 2.10. Hence we need only consider forward travelling bound modes and the radiation continuum within the fibre<sup>§</sup>. Since the analysis is performed

---

<sup>§</sup> The radiation continuum are modes that are valid solutions of the wave-equation<sup>[11]</sup> but do not asymptotically approach zero as  $r \rightarrow \text{inf}$ . There are two types – Evanescent modes that are characterised by  $Re(\beta)=0; Im(\beta)>0$  which decay exponentially with  $z$  and Radiation modes where  $0 \leq \beta < kn_{cladding}$  which are real, have a continuum of  $\beta$  values and individually propagate without loss in  $z$ . However, when summed *in tota*, they represent energy travelling away from core in the transverse direction.

exclusively in the spatial domain we can also ignore the time dependence  $e^{-i\omega t}$  of each field since it will simply remain as a factor at each stage. Indeed a polychromatic extension of the analysis leads only to a summation of each equation over frequency, independent of the spatial domain.

An illuminating electric field is placed on the end face of the fibre  $E_i(x, y)$ . It is important to note that no simple relationship exists between  $E_i(x, y)$  the illuminating field and  $E_t$  for an arbitrary fibre transverse refractive index profile since  $E_t$  composes both  $E_i$  and the back reflection,  $E_r$ . However since we are dealing only with weakly guiding fibres then  $n_{core} \approx n_{cladding}$  and the whole of the end face of the fibre can be approximated as a homogenous block from which a planar  $E_i$  results in a planar  $E_r$ . The total field is then unaltered in form but attenuated by the term  $T = 4n_{input}n_{core}/(n_{input}+n_{core})^2$ .

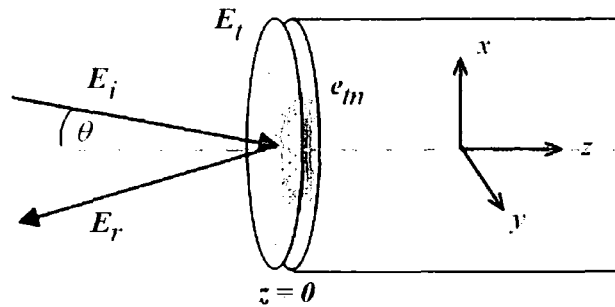


Figure 2.10 – Coupling light into a fibre

The generalised boundary conditions on the electric and magnetic fields at the end face of the fibre are  $E_{\parallel}^1 = E_{\parallel}^2$  and  $H_{\parallel}^1 = H_{\parallel}^2$  the continuity of the transverse electric and magnetic field components, a consequence of Gauss and Ampere's laws, respectively<sup>[7]</sup>. Also the only supported electromagnetic fields within the fibre are the bound (as noted above, assumed lossless) and radiation modes and hence the following equality must be true for any  $E_t$ ,

$$\begin{aligned}
 E_t(x, y) &= \sum a_m e_m(x, y) + E_{rad}(x, y) \\
 H_t(x, y) &= \sum_m a_m h_m(x, y) + H_{rad}(x, y)
 \end{aligned}
 \tag{2.23}$$

where  $m$  is the summation over all forward propagating modes  $\mathbf{e}_m(x,y)$ , each with an associated amplitude coefficient  $a_m$  and  $\mathbf{E}_{rad}(x,y)$ , represents the radiation continuum. It is a standard result in the theory of step index waveguides <sup>[1,8]</sup> that an orthogonality relation between modes exists such that,

$$\int_A \mathbf{e}_m \times \mathbf{h}_n^* \cdot \hat{\boldsymbol{\mu}}_z dA = \delta_{mn} \quad (2.24)$$

( $\hat{\boldsymbol{\mu}}_z$  is the  $z$ -directed unit vector) and  $A = \mathcal{R}^2$ , the infinite  $(x-y)$  plane.

In order to compute the coupling of  $\mathbf{E}_t$  into mode  $n$  we first take the vector product of Eq. (2.23) with the complex conjugate of the mode of interest,  $\mathbf{h}_n^*$  and then integrate over  $A = \mathcal{R}^2$  to yield,

$$\int_A \mathbf{E}_t \times \mathbf{h}_n^* \cdot \hat{\boldsymbol{\mu}}_z dA = \sum_m \int_A a_m \mathbf{e}_m \times \mathbf{h}_n^* \cdot \hat{\boldsymbol{\mu}}_z dA + \int_A \mathbf{E}_{rad} \times \mathbf{h}_n^* \cdot \hat{\boldsymbol{\mu}}_z dA \quad (2.25)$$

By the orthogonality relation Eq. (2.24) the right hand side of Eq. (2.25) is zero valued for all  $m \neq n$  and since the integral does not operate on the amplitude coefficient  $a_m$ , we take it out of the integrand to yield,

$$a_n = \frac{\int_A \mathbf{E}_t \times \mathbf{h}_n^* \cdot \hat{\boldsymbol{\mu}}_z dA}{\int_A \mathbf{e}_n \times \mathbf{h}_n^* \cdot \hat{\boldsymbol{\mu}}_z dA} \quad (2.26)$$

Since we are only treating fibres with assumed fully-bound modes then all bound-mode power travels in the  $z$ -direction only. The time averaged Poynting vector <sup>[12]</sup> can then be integrated over the infinite transverse plane to yield the bound-mode power  $P$ ,

$$P = \int_A \langle \mathbf{S} \rangle \cdot \hat{\boldsymbol{\mu}}_z dA = \frac{1}{2} \int_A \text{Re}(\mathbf{E} \times \mathbf{H}^*) \cdot \hat{\boldsymbol{\mu}}_z dA \quad (2.27)$$

However  $\mathbf{E} = a_n \mathbf{e}_n$  and  $\mathbf{H}^* = a_n \mathbf{h}_n^*$  hence the modal power in mode  $n$ ,  $P_n$  is

$$P_n = \frac{1}{2} a_n^2 \int_A (\mathbf{e}_n \times \mathbf{h}_n^*) \cdot \hat{\boldsymbol{\mu}}_z dA \quad (2.28)$$

Again utilising Eq. (2.27) to calculate the total power,  $P$  in the field in the end face of the fibre  $\mathbf{E}_t$ , substituting Eq. (2.26) into Eq. (2.2.8) and taking the ratio  $P_n/P$  yields the coupling integral<sup>[1,8]</sup>,

$$\begin{aligned} \frac{P_n}{P} &= \frac{\frac{1}{2} \left( \frac{\int_A \mathbf{E}_t \times \mathbf{h}_n^* \cdot \hat{\boldsymbol{\mu}}_z dA}{\int_A \mathbf{e}_n \times \mathbf{h}_n^* \cdot \hat{\boldsymbol{\mu}}_z dA} \right)^2 \left( \frac{\int_A \mathbf{e}_n \times \mathbf{h}_n^* \cdot \hat{\boldsymbol{\mu}}_z dA}{\int_A \mathbf{E}_t \times \mathbf{H}_t^* \cdot \hat{\boldsymbol{\mu}}_z dA} \right)}{\left( \int_A \mathbf{E}_t \times \mathbf{h}_n^* \cdot \hat{\boldsymbol{\mu}}_z dA \right)^2} \\ &= \frac{\left( \int_A \mathbf{E}_t \times \mathbf{h}_n^* \cdot \hat{\boldsymbol{\mu}}_z dA \right)}{\left( \int_A \mathbf{e}_n \times \mathbf{h}_n^* \cdot \hat{\boldsymbol{\mu}}_z dA \right) \left( \int_A \mathbf{E}_t \times \mathbf{H}_t^* \cdot \hat{\boldsymbol{\mu}}_z dA \right)} \end{aligned} \quad (2.29)$$

This integral equation can be recognised as an inner product in the numerator normalised in power in the denominator and hence sum of  $P_n$  over all modes of the fibre will yield a Fourier like decomposition of the input field but in the basis of the fibre modes.

2.4.2 *Range of validity of the coupling integral*

It should be noted that Eq. (2.23) is valid only for  $\theta \ll \theta^2$  due to the need for both  $E$  and  $H$  terms in Eq. (2.2.3) to be valid simultaneously, so some experimental verification of the validity of the coupling integral out to large angles is required. The easiest way to achieve this is to test the coupling at various angles into a single-mode fibre since there is a known relationship between coupling and beam angle for a single input beam <sup>[1]</sup> as shown in Fig 2.11

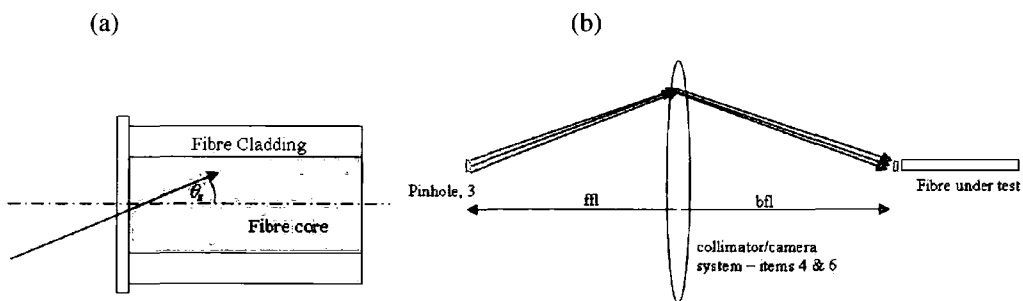


Figure 2-11 – A single input beam to the fibre, (b) input focal ratio modelled as multiple beams

The transmission efficiency of the fibre (assuming no bend loss and perfectly prepared end faces) is given by

$$\frac{P_o}{P_s} = \frac{1}{1 - \cos \theta_m} \int_0^{\theta_m} \frac{P_o(\theta)}{P} \sin \theta d\theta \tag{2.30}$$

where  $P_o/P_s$  is the ratio of the total power coupled into the fundamental mode and the total power in the incident illumination,  $P_o(\theta)/P$  is the ratio of power coupled into the fundamental mode to total incident power for a uniform beam incident on the fibre end face at angle  $\theta$ . Hence Eq. (2.30) is just an integral over a continuum of planar input beams at range of angles 0 to  $\theta_m$ .

Experimentally, the arrangement in Fig 2.11(b) can be approximated by using the experimental apparatus shown in Fig 2.12.

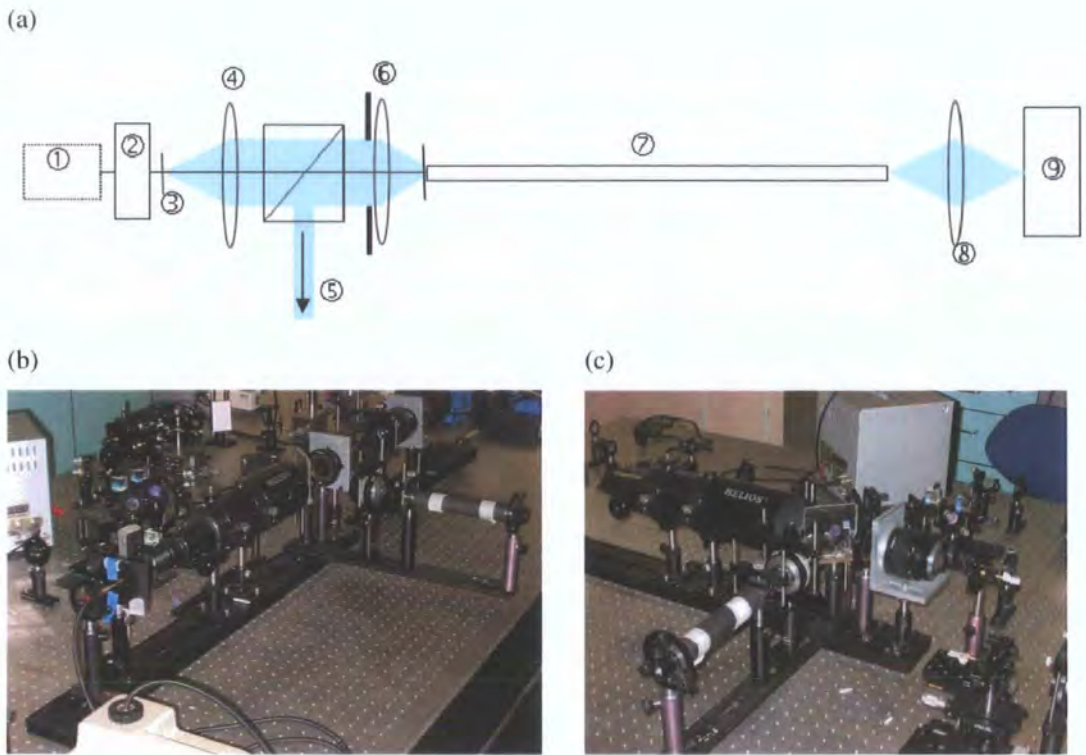


Figure 2.12(a) – Test apparatus for coupling integral - 633nm laser aligned along whole rig, ② White light source & 633nm filter, ③ Pinhole, ④ Collimating lens, ⑤ Beam splitter and microscope used to align fibre with pinhole image, ⑥ Iris used to set focal ratio of camera lens that feeds the fibre, ⑦ The fibre under test carefully mounted in Newport seven axis mounts to reduce fibre stress plus glass plate and index matching grease at fibre input, ⑧ Imaging optics used to collect the light output from the fibre and send it to the CCD, ⑨ The CCD camera; an SBIG, ST7.(b) the entire rig-(c) the fibre feed

The pinhole image placed on the fibre core acts as the diffuse source with  $\theta_m$  selected by altering the input focal ratio. With reference to Fig 2.11(b), the pinhole and its image are so small by comparison to the front and back focal lengths of the collimator/camera (ffl, bfl in the figure) that the rays emanating from all points on the pinhole passing through any given infinitesimal lens element reach the image at almost identical angles and hence, as per the model, the light coming from any given angle (lens infinitesimal) can be modelled as a plane wave. Now,  $P_o(\theta)/P$  takes an extremely complicated form (Snyder and Love equation 20-26) for the step index fibre and hence the output of Eq.(2.30) is computed numerically.

The fibre and rig were carefully aligned in angle with the back reflection off the glass plate used to reduce the angular uncertainty to  $50\mu\text{m}$  in  $85\text{mm}$ , the focal length of the feeding lens, 6. The aperture was set to an accuracy of  $\pm 20\mu\text{m}$  using a digital vernier calliper and iris (6) centration error was estimated at  $<100\mu\text{m}$ . The uncertainty in the focal length of the lens is estimated at a very generous  $1\text{mm}$ , since the component used was a high quality photographic  $f/1.4$  lens. Since angular uncertainties such as centration error can only work to decrease the focal ratio, the error bars are asymmetric in ordinate.

The uncertainty in throughput is due to the sum in quadrature of three terms. The photon noise, the uncertainty in the area of the iris used to normalise the throughput and finally a 5% uncertainty in the illumination of the iris; determined in a separate experiment.

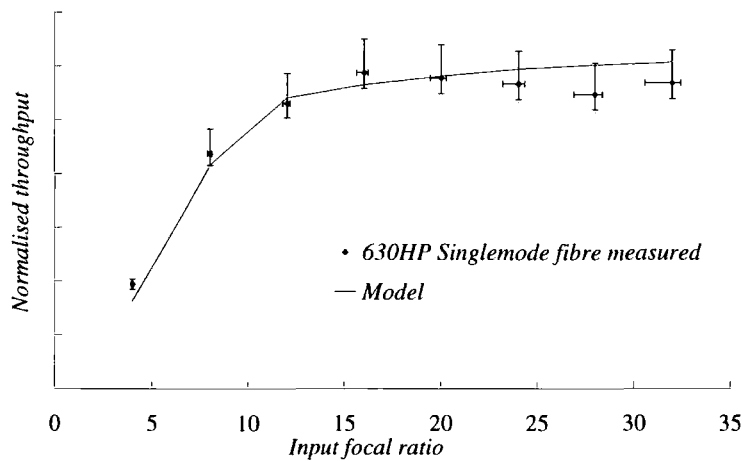


Figure 2.13 – Plot of relative coupling efficiency against input focal ratio – experimental and modelled – Eq(2.30).

The theoretical curve was calculated using the manufacturers stated core RI and fibre NA. The measured data are on a relative scale so the two data sets were normalised and show excellent agreement for all points except some small discrepancy at  $f/4$  where the model is expected to start to break down. This experiment is revisited in chapter 5 where the coupling integral, and various results based on it are experimentally validated with significantly smaller uncertainties but at much smaller  $\theta_z$ . This experiment does however, give us confidence in the behaviour of the coupling integral at high input angle.

## 2.5 Summary

In this chapter, the ray optical and electromagnetic modal models of step index optical fibres were derived and the two compared and shown to be equivalent at large  $V$ . This relationship will be revisited in Chapter 6.

Various tools and results were derived that will be useful throughout the rest of this work and the validity of the angular range of the coupling integral Eq. (2.23) tested experimentally.

## 2.6 References

- 1) 'Optical Waveguide Theory' A Snyder and JD Love, Kluwer (1983)
- 2) 'Optics', Hecht E., 3<sup>rd</sup> ed. Addison-Wesley (1998)
- 3) 'Single-mode fibre optics', J Jeunhomme LB, Marcel Dekker (1990)
- 4) L Ramsey, S Barden, ASP Conference series – Fibre optics in astronomy, 3 (1988)
- 5) 'The implications of image scrambling and focal ratio degradation in fibre optics on the design of astronomical instrumentation', CA Clayton, Astronomy and Astrophysics, Vol. **213**, no. 1-2, p. 502-515 (1989)
- 6) 'A method for determining the focal ratio degradation of optical fibres for astronomy', E Carrasco & I Parry, Mon. Not. R. Astron. Soc., 271, 1 (1994)
- 7) 'Electromagnetism', Grant and Phillips, John Wiley and Sons Ltd (3 Oct 1990)
- 8) 'Single-Mode Fibres' EG Neumann, Springer-Verlag (1988)

# Chapter 3

---

## *Photonic crystal fibres*

### **3.1 Introduction**

Photonic Crystal fibres (PCF) are a new generation of optical fibre that trap and guide light via a two-dimensional photonic crystal structure rather than the more traditional single (radial) dimension of step or graded-index fibres. PCFs guide light by one of two mechanisms, *photonic band gap* or *index guidance*. This chapter provides a rudimentary explanation of these two phenomena along with a discussion of those properties most relevant to astronomy.

Section 3.2 contains some physical background intended to gently ease the non-specialist reader into the more detailed explanations of photonic band gap and index guiding fibres in section 3.3 and 3.4, respectively. The coupling integral from Chapter 2 is revisited and applied to photonic crystal fibres in section 3.5.

### **3.2 Some physical background.**

Dense matter, such as glass for instance, is made up of a three dimensional array of atoms held together electromagnetically in a lattice structure. That is, dense matter at the sub-microscopic level is inherently lumpy so an obvious question to ask is ‘*how can a beam of light pass through such a medium without being scattered in all directions?*’

The answer to this problem can be explained with the aid of Fig. 3.1, which shows a beam of light incident on a block of a dense medium such as fused silica, for instance. The incident light wave excites each row of atoms in the material, which then reradiate (elastically and resonantly) and excite the next row, together with whatever energy is

left over from the incident beam<sup>[1]</sup>. The number of photons that are absorbed and reradiated in all directions by the atoms is so large that for even relatively modest input beam powers, we can imagine a spherical wavelet being emitted from each atom, with some phase relationship with respect to the incident beam. The scattered wavelets superpose in such a way that the incident beam is bent towards the surface normal, a process we all know as refraction and is allowed to propagate, as a beam, within the material. Macroscopically, we can then assign a refractive index based on Snell's law for beams of light at planar interfaces.

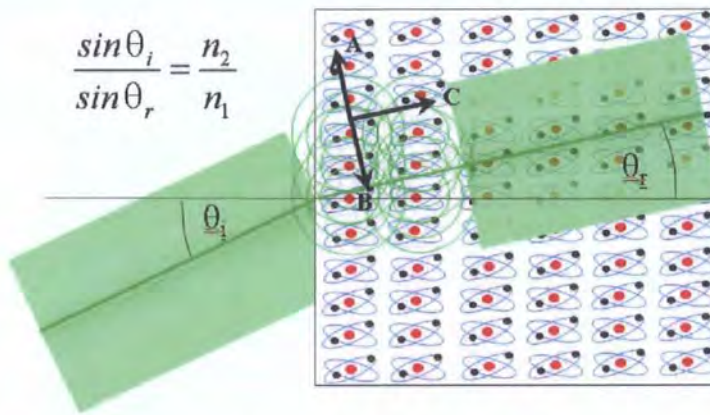


Figure 3.1 – A toy model (not to scale!) of the ensemble light scattering problem for a beam of light incident on a planar surface at angle  $\theta_i$ . The beam excites the first row of atoms in the dense medium which then reradiate and excite the next row, plus whatever energy is left over from the incident beam. The scattered wavelets superpose destructively in the A and B directions within the material and constructively in direction C. The beam thus propagates at angle  $\theta_r$ . We then associate a refractive index  $n_2$  to the dense medium and  $n_1$  to the vacuum outside the block, based on Snell's law, as shown in the figure. Incidentally, this is how we reconcile the fact that photons can only travel at speed  $c$  whereas the beam inside  $n_2$  is slowed to  $v = c/n_2$ . The wavelets travel at  $c$ , the resultant superposed beam travels at  $v$ . An optically opaque material, of course, does not reradiate wavelets from its atomic centres and the energy is absorbed by the atom. A process that gives rise to different coloured glasses by wavelength selective absorption, of course.

Photonic crystal fibres, like all waveguides, trap electromagnetic energy (microwaves, or visible or infra-red or ultra-violet light, for example) within some refractive index structure so that the energy can be usefully guided from one place to another. For instance, traditional, step index fibres, trap light by total internal reflection at the

boundary between the core and the lower refractive index cladding, whereas an air guiding photonic crystal fibre traps light in a core made from air surrounded by a photonic crystal by a mechanism known as a photonic band gap.

As we have seen in the previous chapter, the formalism associated with even the simple step index fibre is complex <sup>[2]</sup> and the situation is no better for photonic crystal fibres<sup>[3]</sup>. However, it is important to understand that *the guiding mechanism and behaviour of all dielectric electromagnetic waveguides can be thought of as due to the solution of the ensemble scattering problem.*

That is, regardless of what the waveguide is made from, glass or plastic or photonic crystals, or how it traps light, whether by total internal reflection or a photonic band gap, its behaviour manifests itself because of the way that light scatters within the waveguide structure. This is a useful baseline to bear in mind when lost in the fine detail of how photonic devices work, although, of course, we don't solve the entire ensemble scattering problem each time we want to understand how light interacts with blocks of material at macroscopic scales.

For instance, a Bragg grating can be thought of as one dimensional photonic crystal and we can certainly say that the wavelets scattered by the atomic centres superpose in the region of the grating for the Bragg wavelength only in the  $-z$  direction, leaving all other wavelengths constructively superposed only in the  $+z$  direction but of course the formalism used to describe a Bragg-grating is usually cast at a far higher level of physical abstraction than that of the atomic <sup>[4]</sup>.

In the case of the step index fibre (and index guiding photonic crystal fibres for that matter) the simplest level of explanation of the guiding mechanism is in terms of the refractive index, however even the notion of a macroscopic refractive index is itself based on the response of a particular block of material to electromagnetic energy. Snell's law for beams of light at planar interfaces is one example of this, see Fig 3.1. Indeed even the complicated (and non-constant) relationship between the refractive index and wavelength, known as material dispersion, can be thought of as occurring due to the highly frequency dependent response of the atomic oscillator.

*Macroscopically*, I will describe the operation of the photonic band gap and (modified) total internal reflection and the description of each is somewhat involved.

However despite the jargonistic nature of (photonic) fibre optical theory, it is useful to remember that both mechanisms are based on the same *sub-microscopic* physics of the ensemble scattering problem.

### 3.3 Photonic band gap fibres

In terms of the light scattering problem, the behaviour of the photonic band gap fibre is relatively simple. One should think of the photonic structure forming the cladding, Fig. 3.2(b), as a 2 dimensional Bragg type structure<sup>[4]</sup>.

Suppose we have arranged, by some means, that a plane wave exists, instantaneously within the photonic crystal fibre as shown in cross section in Fig. 3.2(a). On starting the clock, the component of the plane-wave in the (x-y) direction scatters within the (z-invariant) photonic crystal cladding structure and in much the same way as a 1D Bragg device reflects light at a single wavelength, the wavelets in the cladding structure superpose in the x-y plane to reject the light and reflect it back into the core region over a small waveband.

However, the plane wave has a non-zero component in the z-direction and hence the light is (a) trapped in the core region over a small waveband called the photonic band gap and (b) guided along the fibre in the z-direction.

More difficult to explain without resorting to the formalism, see section (3.3.1), is that the photonic cladding only rejects light from regions of space that have a lower *average* refractive index than that of the structure itself and hence *photonic band gap guiding* (PBG) fibres are characterised by a low index core and narrowband behaviour.

#### 3.3.1 - The photonic band gap

In order to explain how a PBG fibre guides light in more detail we look, initially, at a hexagonal periodic array of air holes in a solid substrate as shown in region **H** of Fig. 3.2. Imagine that the array is unbroken so that no core is present and the periodic structure is extended to infinity. We will discuss what happens when we introduce a defect or in other words a core to form a fibre or waveguide later in this section.

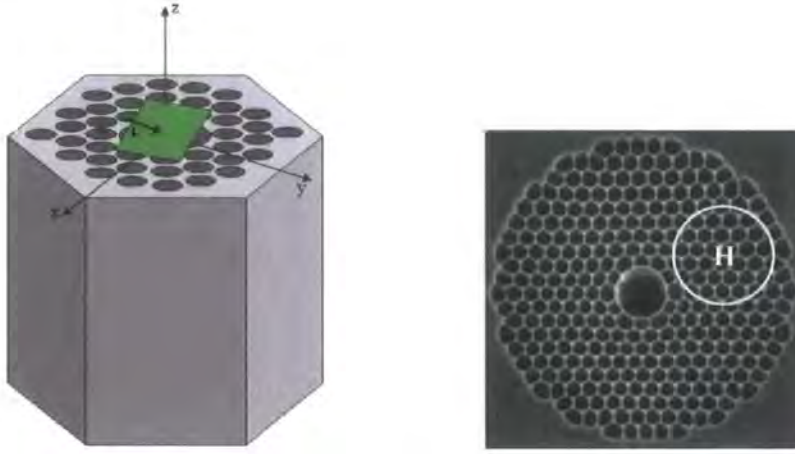


Figure 3.2. (a), Plane wave of wavevector  $\mathbf{k}$ , instantaneously ‘placed’ within an air guiding photonic crystal fibre. The top half of the fibre (i.e. in  $z$ ) is shown removed for clarity. (b) Cross section of an air guiding photonic band-gap fibre. *Crystal Fibre A/S.*

In a periodic medium solutions to the wave equation yield *Bloch* or *Floquet* modes which are the product of a plane wave of wavevector  $\mathbf{k}$  and a periodic function,  $U$  say, characteristic of the periodic refractive index structure. Any energy flowing within the crystal structure is, of course, being scattered amongst regions of differing refractive index; the Bloch modes occur due to the *coherent* nature of the scattering in the *periodic* medium.

For a 2D crystal structure taken as invariant in the  $z$ -direction (Fig. 3.2(b)), the field solutions can be expressed as

$$\mathbf{H}(\mathbf{r}) = \mathbf{H}(\mathbf{r}_{\parallel}) \exp(-ik_z z) = \mathbf{U}_{\mathbf{k}}(\mathbf{r}_{\parallel}) \exp(-i\mathbf{k}_{\parallel} \cdot \mathbf{r}_{\parallel}) \exp(-ik_z z) \quad (3.1)$$

where,  $\mathbf{r}_{\parallel}$  is the projection of  $\mathbf{r}$  onto the  $(x-y)$  plane<sup>[4]</sup>. It is possible to plot the dispersion diagram for all valid solutions of the time independent wave-equation,

$$\nabla^2 \mathbf{H}(\mathbf{r}) = -\omega^2 \mu_o \epsilon_o \epsilon(\mathbf{r}) \mathbf{H}(\mathbf{r}) \quad (3.2)$$

and valid solutions can be found by various techniques for instance the fully vectorial plane wave method in which valid  $\omega$  are the eigenvalues found for each value of  $\mathbf{k}$ .

However it is worth noting that, to date, none of the range of techniques that are available can claim superiority in all cases [3].

There are ranges of values of  $\omega$  in the dispersion space that are found to have no valid modal solutions for all non-degenerate values of  $k_{\parallel}$ .\*\*[4] These are *photonic band gaps*.[] Fig. 3.3 shows a schematic example for a  $z$  invariant crystal for one particular value of  $k_z$ . The black lines are valid values of  $\omega$  at each  $k_{\parallel}$ . Regions (a) and (d) are complete photonic band gaps since they exist for all non-degenerate  $k_{\parallel}$ , whereas (b) and (c) are partial band gaps. Complete band gaps are used to guide light of arbitrary  $k_{\parallel}$  in fibres and crystal waveguides.

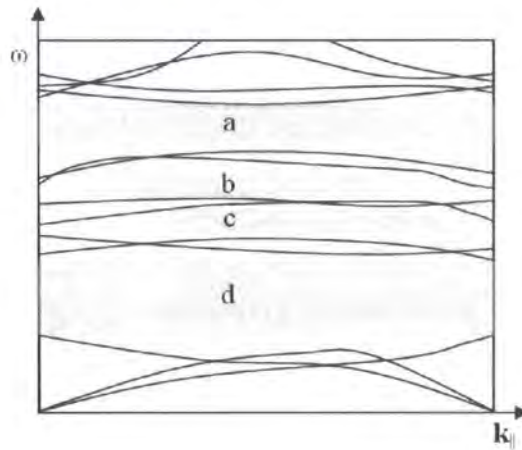


Figure 3.3 – A schematic dispersion diagram for a  $z$  invariant photonic crystal. (a) and (d) are complete photonic band gaps because the gap exists for all non-degenerate  $k_{\parallel}$ , with incomplete (b) and (c).

Looking at Fig. 3 a little more closely, the 2D waveguide under analysis is invariant in  $z$  and attention is then restricted to  $k_{\parallel}$ , i.e. the  $(x-y)$  plane. However, since Equations

\*\* Fig. 3.3 is a schematic example of a dispersion diagram for a hexagonal symmetry photonic crystal. The ordinate is in units of angular frequency,  $\omega$  and the abscissa is a subset of all possible wavevectors sufficient to describe the complete set of all possible wavevectors. A larger initial subset is defined using degeneracy arguments in  $\mathbf{k}$  due to the periodic nature of the crystal. For example  $|k_z|$  and  $(|k_z| + 2n\pi/a)$  are identical Bloch solutions for a Bragg stack (a 1d photonic crystal) infinite in  $(x-y)$  but periodic in  $z$  with spacing  $a$ , for instance. Symmetry and translational arguments in  $\mathbf{k}$ -space reduce the subset further with the final subset defined using only the boundary of the subset in  $\mathbf{k}$ -space. This is known as the irreducible Brillouin zone. The details can be found in reference [4].

3.1 and 3.2 are fully vectorial and the components of  $\mathbf{H}$  are coupled by Eq. 3.2 for  $k_z \neq 0$ , then a change in any component of  $\mathbf{k}$ , including  $k_z$  will effect the resulting allowed values of  $\omega$  for all non-degenerate  $\mathbf{k}_{\parallel}$ . Hence as  $k_z$  changes, the dispersion relation  $\omega$  against  $\mathbf{k}_{\parallel}$  in the  $(x-y)$  plane also changes and hence so do the extents of the band gaps. (One can think of many different plots similar to Fig. 3.3, one for each value of  $k_z$ ). Indeed new band gaps can be opened up by varying the  $k_z$  component of  $\mathbf{k}$  and hence it is possible to plot the extents of any existing band gaps as a function of  $k_z$  only. An example of this is shown in Fig. 3.4.

### 3.3.2 The waveguiding mechanism of PBG fibres.

For some core geometries a defect mode can exist whose dispersion curve falls within the PBG of the cladding, over some range of  $k_z$ , although it should be noted that the PBG's themselves are a property of the cladding only<sup>[3]</sup>. That is, with or without the core, the PBG's will exist within the cladding. In other words, the core allows the defect mode to exist at some  $\omega$ , for a given  $k_z$ , but no cladding mode can exist at this value (it is within a cladding band gap after all) and so the defect mode is confined to the core region by the cladding in the  $(x-y)$  plane of the fibre. But it has a non-zero value of  $k_z$  and so the energy is guided along the fibre.

The choice of ordinate in Fig. 3.4 requires comment. The *modal* (or *effective*) index is often used because it allows *material* refractive indices and *modal* indices to be plotted on the same axes. It is derived from the sinusoidal nature of the mode in  $z$ , see Eq. (3.1), and is given by  $n_{eff} = k_z/k = k_z c/\omega$ . In traditional fibre theory  $k_z$  is often labelled as  $\beta$ .<sup>[2]</sup>

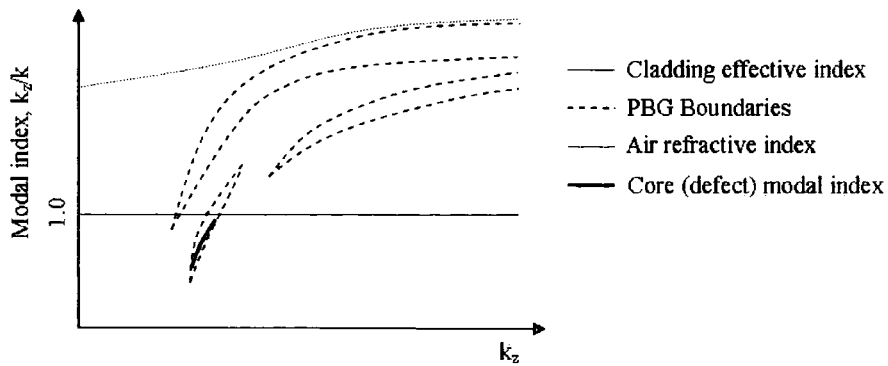


Figure 3.4 – A schematic example plot of  $\beta/k$  against  $\beta$  for a typical air core photonic band gap guiding (PBG) fibre. The PBG surrounding the dispersion curve for a defect mode (continuous line) is below the air line, showing that the fibre supports a guided mode trapped in the air core by a photonic band gap of the cladding structure. Note that  $k_z/k = k_z c/\omega$ .

It is possible for cladding PBG's to exist below the air-line. i.e. below values of  $k_z/k = 1.0$  and hence if the core is manufactured as an air gap with a defect mode within one of the sub airline PBG's then a mode guided in air can exist.

It is useful to assign an effective refractive index to the infinite crystal structure. This can be done for any crystal structure and hence is applicable to either PBG or index guiding fibres.

The lowest frequency mode supported within the (infinite and coreless) cladding structure occurs at  $k_{\parallel} = 0$  (i.e. the plane wave component of Eq. (3.1) travelling only in the  $z$  direction) and is known as the *fundamental space filling mode* (FSM)<sup>[7]</sup>. The ratio  $k_z/k$  at  $k_{\parallel} = 0$  is taken as the 'average' refractive index of the cladding structure. Notice from Fig. 3.4 that since the cladding curve is based on the lowest possible frequency mode then no PBG's can exist above this line. Furthermore, since for PBG guidance the modal index of the defect mode must also be less than that of the cladding then the PBG fibres are characterised by a core that has a lower refractive index than that of the cladding.

Since the defect mode falls within a PBG of the cladding structure we would expect, and find, that the mode field distribution is relatively well confined to the core region, although some energy does reside in the cladding. This might seem to be at odds with the fact that the cladding PBG is supposed to reject the light completely. The solution to this apparent quandary lies in the solution to the ensemble light scattering problem

whereby the scattered wavelets sum to zero deep within the cladding itself but with partially incomplete summation to not quite zero in the vicinity of the cladding/core boundary. In more mathematical terms the transverse part of the propagation constant  $k_{\parallel}$  in Eq. (3.1) becomes complex and the field falls off exponentially with distance within the photonic structure, from the air/photonic structure boundary [4].

### 3.3.3 Characteristics of PBG fibres.

Most commercially available PBG fibres are air guiding due to their low losses (transmission in air) and high power handling capabilities. The core sizes typically range from 4 $\mu\text{m}$  to 14 $\mu\text{m}$  for 400nm and 1550nm PBG's respectively and are therefore of similar general size as traditional step index single-mode fibres. Typically 90% of the guided light is in the air core so very high power lasers may still cause burning in the core/cladding boundary which is possibly an issue for laser pump light transport from observatory floor to launch telescope in laser guide star applications. Fig. 3.4 is somewhat typical of PBG fibres in general and so PBG guidance is characterised by narrowband performance, at least by astronomical standards. Typically low loss (<20db/km) guidance occurs over a few 10's of nm, although some commercially available fibres will transmit at <30db/km over 200nm. (e.g the Crystal Fibre A/S HC-1550-02).

## 3.4 Index guiding fibres

### 3.4.1 General principles

Index guiding fibres are characterised by an average refractive index of the core region higher than that of the cladding. By far the most common type of PCF is the large mode area or LMA fibre the cross section and mode of which is shown in Fig. 5(a,b). The guiding mechanism of these types of fibres is best understood at the level of the refractive index and Fig. 5(c) shows the refractive index of the core and effective index of the cladding of a typical LMA fibre.

All guided modes in a traditional step index fibre must satisfy relationship Eq. (2.6) and the higher core refractive index forces at least one index guided mode to appear between the core and cladding refractive indices. The cladding is seen to behave as a

region of homogeneous material with lower refractive index than the core<sup>[8]</sup> and *index guiding fibres are thus characterised by a core refractive index higher than that of the cladding.*

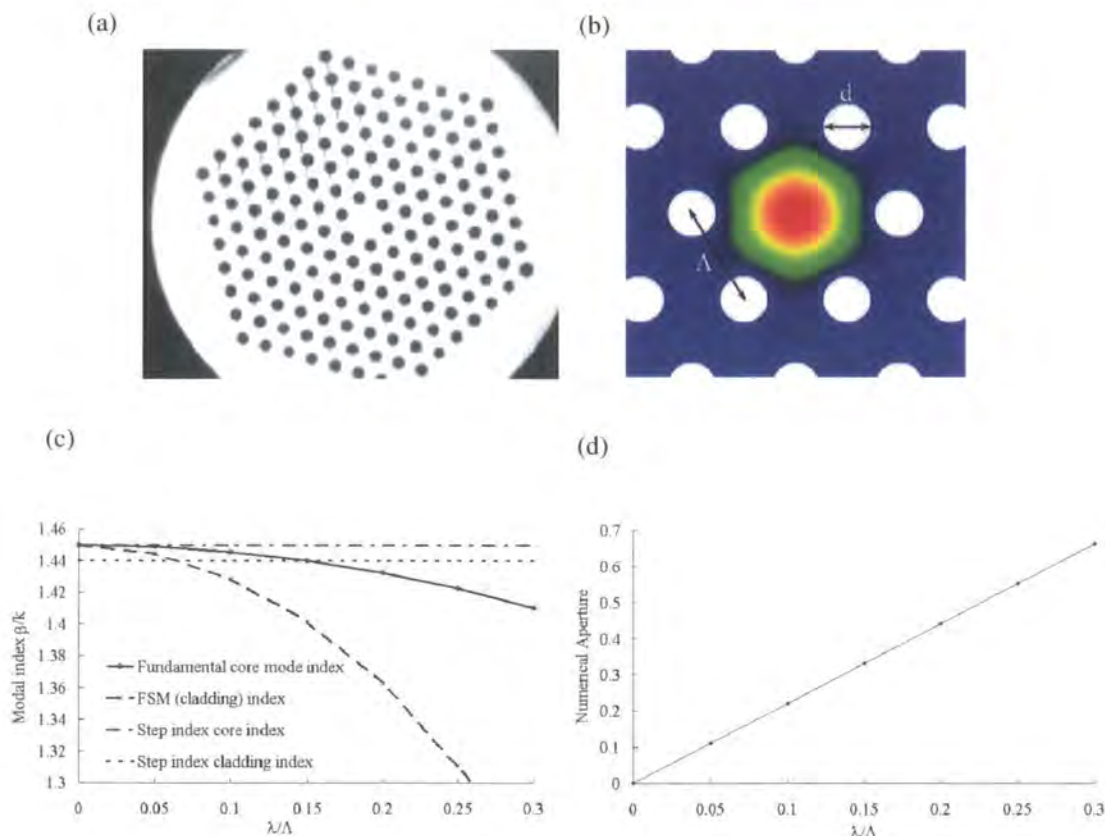


Figure 3.5 – (a) Cross section of an LMA fibre – Crystal Fibre A/S, (b) The geometric layout and mode field distribution, (c) Modal indices of the LMA fundamental core mode and fundamental space filling (cladding) mode as function of  $\lambda$  for a fibre of  $d/\Lambda = 0.40$ .<sup>[9]</sup> The core and cladding refractive indices of a step index fibre are shown (without material dispersion) for comparison. (d) The variation of numerical aperture  $\sqrt{n_{core}^2(\lambda) - n_{clad}^2(\lambda)}$  for the LMA data in panel (c).

The  $V$  value may be defined for an LMA fibre in much the same manner as a step index fibre with

$$V_{step} = ka\sqrt{n_{core}^2 - n_{cladding}^2} \tag{2.7}$$

$$V_{LMA} = k\Lambda\sqrt{n_{core}^2(\lambda) - n_{cladding}^2(\lambda)} \tag{3.3}$$

In the step index case for a given core radius  $a$  and numerical aperture  $NA = \sqrt{n_{core}^2 - n_{cladding}^2}$ , then  $V_{step}$  is proportional to  $1/\lambda$ . Any increase in  $a$  for the same  $\lambda$  will increase the number of modes that can, in some sense, fit within  $a$  and so as the value of  $V$  increases so the number of modes supported increases. In the lower limit, a single-mode cut-off at  $V_{step} = 2.405$  exists below which only the fibre fundamental mode can propagate.

In the LMA case  $n_{core}$  and  $n_{cladding}$  are computed from the fundamental mode of the fibre core and the fundamental space filling mode of the crystal structure and are plotted in Fig. 3.4(c). The variation in the difference between  $n_{core}$  and  $n_{cladding}$  causes  $V$  to become asymptotic (as  $\lambda$  varies) to a value that is a function of  $d/\Lambda$  [7].

It is found that for fibres with  $d/\Lambda < 0.41$  the  $V$  value becomes asymptotic to  $V_{LMA} = \pi$  [6] which is the single-mode cut-off for LMA fibres and so the fibre  $V$  value can never increase above the single-mode cut-off and the fibre becomes *endlessly single-moded* for all wavelengths.

Since coupling analysis into fibre modes depends solely on the mode field distribution a comparison of how step index and LMA fundamental transverse mode field distributions vary with wavelength of the guided light will lead on naturally to a discussion of how the properties of LMA fibres might be used to advantage in astronomy.

### 3.4.2 - Endlessly single-mode behaviour

The core and cladding indices of both step and LMA fibre types can be thought of as forming a potential well of height, NA and with width the same as the fibre core diameter. Figure 3.6.

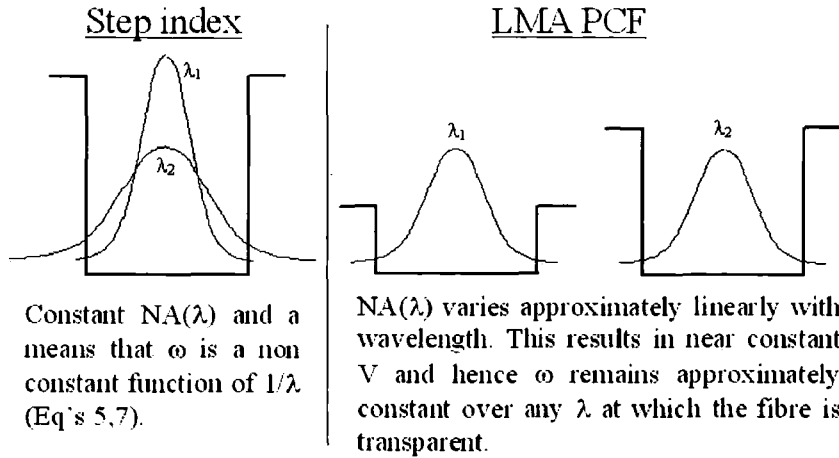


Figure 3.6 – The core/cladding indices can be thought of as potential wells with a width the same size as the fibre core within which the energy of the mode must reside

The fundamental mode field distribution can be approximated as Gaussian for both the step index,<sup>[10]</sup> and LMA fibres<sup>††</sup> and it can be shown that

$$\omega = f(V) = f(a, \lambda, n_{core}, n_{cladding}) \tag{3.6}$$

where  $\omega$  is the  $1/e$  radius of the electric field<sup>[11,12]</sup>.

In the step index case, the numerical aperture is constant with wavelength see Eq. (2.7) & Fig. 3.5(c) and for a constant core diameter  $\omega$  changes (in a highly non linear manner) with wavelength. However, in the LMA PCF case,  $NA(\lambda)$  scales nearly linearly with wavelength, Fig. 3.5(d), over a wide waveband. Hence  $V$  remains almost constant over this interval. This occurs at all  $\lambda$  such that  $A/\lambda > 3$  and the smallest commercially available  $A$  (Crystal Fibre A/S, LMA-8) is  $5.6\mu\text{m}$  which is capable of low loss transmission up to about  $1700\text{nm}$  and so an LMA fibre has a constant mode size, with negligible dependence on wavelength.

---

†† The LMA fibre mode is best approximated by a central Gaussian of  $1/e$  width  $\omega = \sqrt{2}$  from which are subtracted satellite Gaussians each of  $1/e$  width  $d/2$  centred on the inner ring of holes.<sup>[13]</sup> However, approximation by the central Gaussian only is valid since it is the dominant component of the mode field distribution<sup>[14]</sup>.

The useable single-mode spectrum of step index fibres is generally rather limited, in the low wavelength limit by the appearance of higher order modes and in the high wavelength limit by bend loss <sup>[15]</sup>. The bend loss manifests itself due to the larger fraction of energy transported within the cladding of the step index fibre at long wavelengths. For a given bend radius, at some radial distance from the fibre axis  $\delta r$ , Fig. 3.7, the mode field distribution tries to become superluminal and as  $R_b$  increases so  $\delta r$  must increase for the same loss at constant  $\lambda$ .

Practically, of course, this means that the spherical wavelets scattered from the atomic centres that make up the cladding material no longer superpose to create a coherent wavefront (the mode) and the light is radiated in all directions and is therefore lost to the guided mode.

As the wavelength increases, more and more energy in the Gaussian mode is transported in the cladding ( $\omega$  increases wrt to  $a$ ). Hence, for the same  $\delta r$  ( $\delta r_1 = \delta r_2$ ) and  $R_b$ , more energy is lost at higher  $\lambda$  as can be seen by comparing the shaded regions on the left and right hand sides of Fig. 3.7.

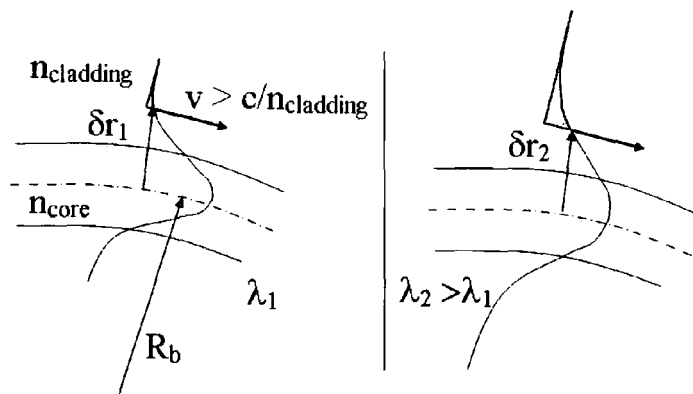


Figure 3.7 – The wavelength dependency of bend loss in optical fibre. Higher modal energy in the cladding implies higher bend losses for the same bend radius,  $R_b$ .

In any practical sense an optical fibre will have some bending along its length, even if of a very large radius  $R_b$ , but at long wavelengths even the very largest  $R_b$  can cause bend losses of the order of  $10^3$  db/km, high enough to effectively make the fibre opaque.

In the case of a PCF the increasing difference between core and cladding at higher wavelengths causes the mode to be rather better confined than for its step index counterpart and although a long wavelength bend loss limit does exist, it is generally at wavelengths at which the base material (typically fused silica) is no longer transparent.

The LMA, as noted, is endlessly single-moded and hence its attenuation spectrum is very broad in comparison to step index alternatives. Fig. 3.8(a) shows the measured single-mode attenuation spectrum of the LMA-8 fibre, (courtesy of Crystal Fibre A/S) and a comparison of this spectral range with typical commercially available step index fibres is shown in Fig. 3.8(b). The LMA-8 is capable, in principle, of replacing three or possibly four step index alternatives on this criteria alone.

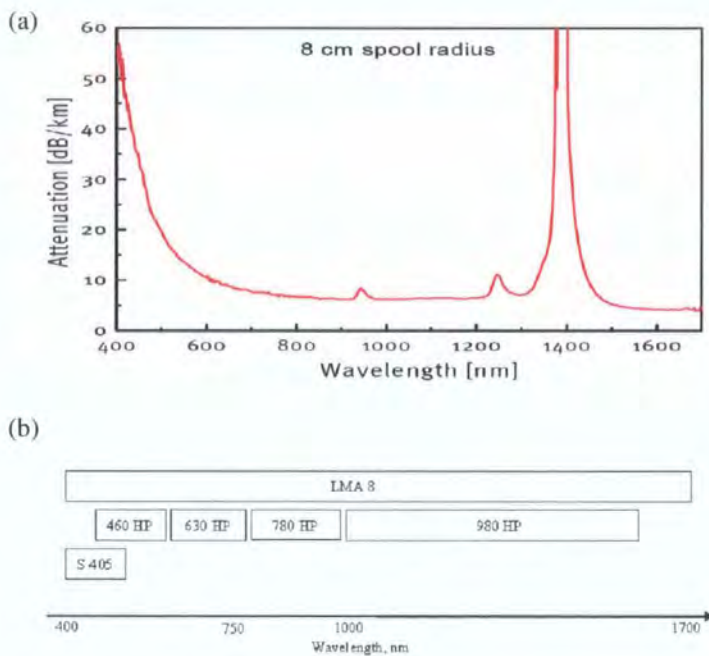


Figure 3.8 – (a) Attenuation spectrum (pass band) of an LMA fibre – Crystal Fibre A/S, (b) the useable pass bands of an LMA-8 in comparison to various step index single-mode fibres.

Despite its endlessly single-mode behaviour, from Fig. 3.8(a), the LMA does have a lower limit in its attenuation spectrum. This is a feature of only LMA type fibres and is also associated with bend loss<sup>[3]</sup>.

The relationship between the location of the bend loss edge, the characteristic size of the LMA fibre,  $\Lambda$ , and the transported wavelength,  $\lambda$ , is not simple but good a numerical fit of bend loss attenuation as a function of  $V_{LMA}$  and of  $V_{LMA}$  itself, in terms of easily specified fibre parameters and the wavelength of the light <sup>[16]</sup>, can be used to estimate the bend loss edge in the attenuation spectrum. See Fig. 3.9.

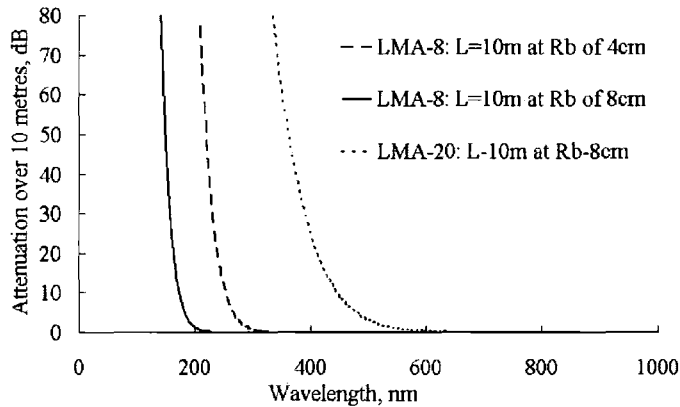


Figure 3.9 – Modelled bend loss edges for the LMA-8 and LMA-20 fibres. See text for discussion.

The figure shows the lower bend loss edges for the LMA-8 at  $R_b = 4\text{cm}$ ,  $8\text{cm}$  and the LMA-20 fibre at  $R_b = 8\text{cm}$  all over a  $10\text{m}$  length of fibre. The plot shows the dynamic position of the bend loss edge with changing  $R_b$  and this must be considered when designing the fibre run. For instance the LMA-8 can tolerate a value  $R_b$  of  $4\text{cm}$  or so with negligible bend loss at any  $R_b > 4\text{cm}$  at wavelengths lower than  $350\text{nm}$ . On the other hand, the LMA-20, which has a characteristic size of  $\Lambda = 13.2\mu\text{m}$  requires a minimum  $R_b$  of  $8\text{cm}$  for negligible losses at  $>650\text{nm}$  and it is this lower bend loss edge and its dynamic nature that forces a maximum core size on the LMA fibre for a given required waveband.

The core size of a step index fibre is typically rather small. This is due to the fact that the core/cladding refractive index difference is kept as small as possible to reduce scattering (and therefore losses) within the cladding. Therefore the core must be kept rather small in order for  $V < 2.405$  for some given wavelength. In the mid NIR,  $1550\text{nm}$  fibres have a typical diameter of  $10\mu\text{m}$ , but since the mode size scales with  $\lambda$  then this reduces to  $2\text{-}3\mu\text{m}$  in the lower VIS (measured to the  $1/e$  point). As already noted the smallest available LMA fibre (Crystal Fibre A/S, LMA-8) has a

characteristic size,  $\Lambda = 5.6\mu\text{m}$  which means a core diameter of  $2\omega = 2\Lambda/\sqrt{2} = 7.91\mu\text{m}$ , somewhat larger than the step index alternative in the same waveband.

However, the lower bend-loss edge prevents the use of larger core fibres for shorter wavelengths for instance we have already noted that the LMA-20 with its  $19\mu\text{m}$  core size is not really a satisfactory replacement for the LMA-8 unless the fibre is kept in a straight and stable configuration.

### 3.4.3 - Characteristics of index guiding (single-mode) fibres.

In summary, whilst step index single-mode fibres are characterised by a very small mode field size which scales in a non-linear manner with wavelength and a very limited attenuation spectrum, LMA PCF's exhibit a wavelength independent core size typically 2-3 times larger than the step index alternative at the same wavelength (for negligible dynamic bend losses) and a much broader attenuation spectrum with this fact alone making the LMA fibre much more attractive to astronomy.

### 3.5 The coupling integral revisited

The application of the coupling integral, as derived in Chapter 2, to photonic crystal fibres requires comment. As noted in the previous chapter, the modes of the fibre are either radiative or bound. However, near to cut-off, but  $U \geq V$ , the radiative field, the sum over all radiative modes, can be shown to closely approximate that of the bound mode but with some energy flow in the transverse direction <sup>[2]</sup>. Such 'lossy' modes, as they are known can be described using a complex propagation constant such that,

$$e_m(x, y)e^{i(\beta z - \omega t)} = e_m(x, y)e^{-\text{Im}(\beta)z}e^{i(\text{Re}(\beta)z - \omega t)} \quad (3.7)$$

Hence for  $\text{Im}(\beta) > 0$ , the propagating field is attenuated exponentially with distance; a lossy mode, whereas, if  $\text{Im}(\beta) = 0$ , the propagation constant is real and the mode propagates without attenuation along  $z$ . This loss is in addition to material absorption or scattering loss.

For LMA fibres of an arbitrary but finite number of rings of holes about the fibre core (defect),  $N_r$ , the rather curious situation arises in that there are **no completely bound modes**. Each ‘guided’ mode can to some degree propagate energy in the transverse direction and hence all modes of LMA fibres are lossy and are thus characterised by a complex propagation constant,  $\beta$ .<sup>[15]</sup> The magnitude of the transverse power loss can be shown to reduce exponentially with  $N_r$ <sup>[18]</sup> for fixed  $k_0A$ . ( $k_0$ , the free space wavelength).

Using the CUDOS package<sup>[19]</sup>, which is based on the multipole method<sup>[17]</sup>, Figure 3.10, shows the magnitude of the imaginary part of  $\beta$ .

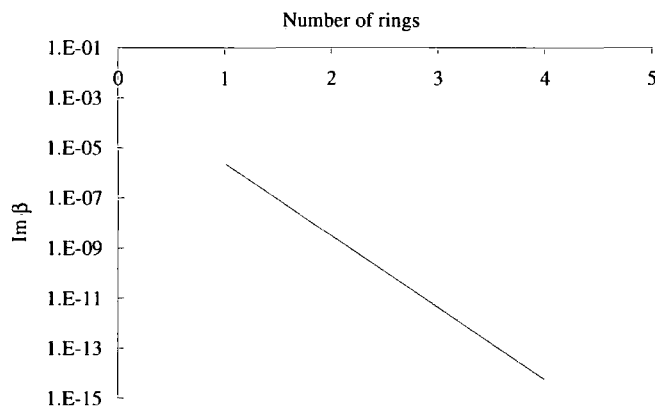


Figure 3.10 –  $\text{Im}(\beta)$  as a function of the number of rings holes surrounding the core for an LMA-8 type fibre.

Since  $\text{Re}(\beta) \sim 1.45$  in all cases shown and most commercially available fibres have 7 or more rings of holes  $\beta$  can be reasonably taken as completely real. Thence, bound mode power does not, approximately, travel in the transverse direction and Eq. (2.29) can be applied. Further, Ferrando *et al*<sup>[20]</sup> show that even for refractive index profiles requiring a fully vectorial analysis the modal orthogonality relation, Eq.(2.24) still holds. Finally, Mortensen and Dabirian<sup>[21]</sup> have shown that the loss due to the back reflection at the fibre end face for most commercially available LMA type fibres can be modelled as a planar Fresnel loss and finally, therefore, the coupling integral, Eq.(2.29) can also be applied to well bound LMA fibres.

### 3.6 Summary

This chapter has introduced the new breed of photonic crystal fibres and their properties, most relevant to astronomy, by comparison to the more traditional step index fibre. We have concentrated on single-mode fibres since, as chapters 4 and 5 will show, the LMA fibre provides significant performance advantages in fibre stellar interferometry.

### 3.7 References

- 1) 'Optics' Hecht E, 3<sup>rd</sup> ed. Addison-Wesley (1998)
- 2) 'Optical Waveguide Theory', A Snyder and JD Love, Kluwer (1983)
- 3) 'Photonic Crystal Fibres' A Bjarklev, J Broeng, AS Bjarklev, Kluwer (2003)
- 4) 'Photonic Crystals: Molding the flow of light', JD Joannopolous, RD Meade and JN Winn, Princeton (1995)
- 5) 'Inhibited spontaneous emission in solid-state physics and electronics', E Yblanovitch, Phys. Rev Lett. **58** p2059-2062 (1987)
- 6) 'Strong localisation of photons in certain disordered dielectric superlattices', John S, , Phys. Rev Lett. **58** p2486-2489 (1987)
- 7) 'Endlessly single-mode photonic crystal fiber' T Birks , J Knight J and P Russell, Opt. Lett. **22**, 961 (1997)
- 8) 'Properties of photonic crystal fibre and the effective index model', J Knight, T Birks, P Russell, J Sandro, JOSA A, **15** p748-752, (1998)
- 9) 'Modal cutoff and the V parameter in photonic crystal fibers', Mortensen NA, Folkenberg JR, Nielson MD and Hansen KP, Opt. Lett. **28**, 1879 (2003)
- 10) 'Single-mode fibre optics', Jeunhomme LB, Marcel Dekker (1990)

- 11) 'Gaussian approximation of the fundamental modes of graded-index fibers' D Marcuse, *JOSA* **68**, 103 (1978)
- 12) 'Mode Field Radius of Photonic Crystal Fibers Expressed by the V-parameter' MD Nielson, NA Mortensen, JR Folkenberg and A Bjarklev, *Opt. Lett.* **28**, 2309 (2003)
- 13) 'Effective area of photonic crystal fibers'. NA Mortensen and JR Folkenberg, *Opt. Exp.* **10**, 475 (2002)
- 14) 'Photonic crystal fiber design based on the V-parameter', MD Nielson and NA Mortensen, 2003. *Opt. Exp.* **11**, 2762 (2003)
- 15) 'Bandwidth comparison of photonic crystal fibres and conventional single-mode fibres' MD Nielson, JR Folkenberg, NA Mortenson and A Bjarklev. *Opt. Express* **12**, No.3 (2004)  
<http://www.opticsexpress.org/abstract.cfm?URI=OPEX-12-3-430>
- 16) 'Predicting macrobending loss for large-mode area photonic crystal fibres', MD Nielsen, NA Mortensen, M Albersen, JR Folkenberg, A Bjarklev, D Bonacinni. *Opt. Express* **12**, No.8 (2004)  
<http://www.opticsexpress.org/abstract.cfm?URI=OPEX-12-8-1775>
- 17) 'Multipole method for microstructured optical fibre. II Implementation and Results' BT Kuhlmeiy, TP White, G Renversez, D Maystre, LC Botton, C Martijn de Sterke, RC McPhedran. *J. Opt. Soc. Am. B* **19** , No 10 (2002)
- 18) 'Microstructured optical fibre: where's the edge?'. B Khulmey, *Optics Express* Vol **10**, No 22 (Nov 2002)
- 19) CUDOS - <http://www.physics.usyd.edu.au/cudos/mofsoftware/>

- 20) 'Full-vector analysis of a realistic photonic crystal fibre', A Ferrando, E Silvestre, JJ Miret, P Andrs, and M V Andrs, *Optics Letters*, Vol. **24**, Issue 5, pp. 276-278 (1999)
  
- 21) 'The coupling performance of photonic crystal fibres in fibre stellar interferometry', JCW Corbett, A Dabirian, T Butterley, NA Mortensen, JR Allington-Smith, *Monthly Notices of the Royal Astronomical Society*, **368**, 203–210, (2006)

# Chapter 4

---

## *Coupling starlight into PCF's- I*

### *Direct feed*

#### **4.1 Introduction**

Single-mode fibres are used in stellar interferometry as a means of convenient, coherent transport of starlight between multiple apertures.

A fibre stellar interferometer produces an interferogram as depicted in Fig 4.1. The optical path difference (OPD) is altered and the intensity at the output measured. At zero OPD the visibility of the fringes is measured. The visibility of the fringe is numerically equal to the magnitude of the complex degree of (spatial) coherence,  $\gamma$ , of the two apertures,  $A$  and  $B$ , i.e.

$$V = |\boldsymbol{\gamma}_{A,B}(0)| \quad (4.1)$$

where the bold type signifies the complex form of  $\gamma$ . The zero value denotes the fact that the *spatial* degree of coherence of apertures  $A$  and  $B$  is being measured at the same point in time – hence the need for significant path length compensation.

The phase of  $\gamma$  is associated with the offset of the fringe pattern from the zero point. In its simplest form the analysis is based on the van-Cittert Zernike theorem which states that the complex visibility (i.e. magnitude and phase) is numerically equal to the Fourier component of the image intensity on the baseline of the two telescope apertures. The measured visibility is then used to infer information about the object - e.g. the separation of a double star system, or the diameter of a single star. Discussion

of imaging ‘phase closure’ techniques and recording interferograms with multiple baselines <sup>[1]</sup> is well outside the scope of this chapter.

Typically the telescope PSF is fed directly into the fibre, as shown in the diagram, and since only a single electromagnetic mode can exist within the fibre and interferometric recombination occurs at the fibre output, the object image is spatially filtered and atmospheric degradation of the wavefront is reduced to an intensity variation in coupling into the fibre. The two photometric outputs,  $P_1$  and  $P_2$  and the interferometric output  $I$  can all be monitored in real time and the interferogram can be corrected in post processing. Examples of such instruments are FLUOR on the McMath solar tower on Kitt peak, VINCI on the VLTI at Cerro Paranal in northern Chile and, most ambitiously of all, the OHANA array connecting, Keck I, Keck II, Subaru, Gemini (North!), CFHT, IRTF and UKIRT. Also, an excellent treatment of this type of instrument is given by du Foresto <sup>[2]</sup>, one of the pioneers in the field.

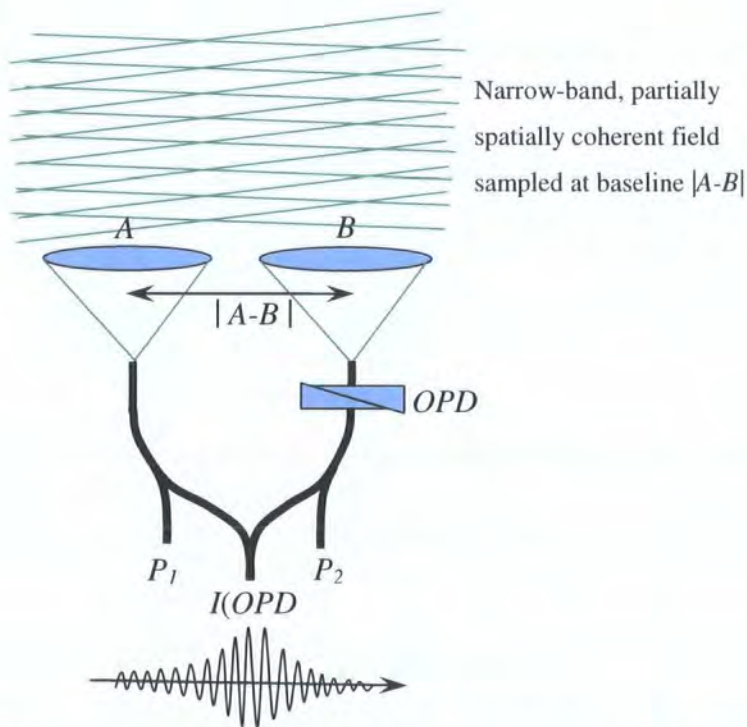


Figure 4.1 – Interferometric recombination using single-mode fibres.

A note on the form of the interferogram. The two telescopes form a Young’s slit pair and changing the OPD is akin to sampling different points of the characteristic diffraction pattern of fine fringe detail due to the slit spacing and modulating envelope due to the slit width. The visibility of fringes falls off with increasing OPD due to the

form of the modulating envelope *and* reduced temporal coherence due to the (inevitable) finite bandwidth.

As discussed in the previous chapter, step index fibres are characterised by a generally rather limited pass band<sup>[3]</sup> and very small core size, especially in the visible part of the spectrum. As Peryllioux notes<sup>[4]</sup>, this makes alignment to the multiple step index fibres required for various target pass bands quite challenging. The broadband, endlessly single moded behaviour of LMA fibre with its larger core size is, thus, of obvious interest to fibre stellar interferometry.

In this chapter we investigate the coupling efficiency of the PSF's of an obscured circular aperture and un-obscured square and hexagonal apertures under conditions of ideal seeing (section 4.2) and the atmospherically aberrated PSF of an obscured telescope pupil (section 4.3) into LMA type fibres of arbitrary characteristic scale,  $\lambda$ . In section 4.4 a new coupling scheme is proposed based on deliberate defocusing of the telescope PSF at the fibre end face.

#### 4.2 Coupling light in ideal seeing conditions

In this section we investigate the coupling efficiency into the LMA fibre under conditions of ideal seeing. This means that no aberrations are present in the plane wavefront at the telescope entrance pupil and this is done since it represents the best possible coupling efficiency.

We turn to the coupling integral Eq. (2.29) to compute the coupling efficiency of fields incident at the fibre end face from the telescope. Previous treatments<sup>[5,6]</sup> for step index fibres have allowed the Gaussian mode of the step index fibre to propagate to the telescope exit pupil and the coupling computed there for convenience. However, no simple Fourier transform relationship exists between the near and far fields of LMA photonic crystal fibres<sup>[7]</sup> therefore the coupling is computed, using Eq 2.29, at the end-face of the fibre. The integrations were performed numerically using a simple midpoint routine which yielded the most stable and accurate solutions, matching analytical results to within +/-1%. The mode fields were calculated using the multipole method<sup>[8,9,10]</sup>. The incident fields for the cases of annular, square and hexagonal apertures, respectively are found to be,

$$\mathbf{E}_c(x, y) = \frac{J_1\left(\frac{kr}{2F_T}\right)}{\left(\frac{kr}{2F_T}\right)} - \varepsilon^2 \frac{J_1\left(\frac{\varepsilon kr}{2F_T}\right)}{\left(\frac{\varepsilon kr}{2F_T}\right)} \quad (4.1)$$

$$\mathbf{E}_s(x, y) = \frac{\sin\left(\frac{\sqrt{2}\pi x}{\lambda F_T}\right)}{\left(\frac{\sqrt{2}\pi x}{\lambda F_T}\right)} - \frac{\sin\left(\frac{\sqrt{2}\pi y}{\lambda F_T}\right)}{\left(\frac{\sqrt{2}\pi y}{\lambda F_T}\right)} \quad (4.2)$$

$$\begin{aligned} \mathbf{E}_h(x, y) &= \frac{1}{2\pi^2 xy} \\ &\times \left\{ \frac{\sqrt{3}x}{\sqrt{3}x+y} \left[ \cos\left(\frac{\pi}{\lambda F_T} \frac{y-\sqrt{3}x}{1+\sqrt{2}}\right) - \cos\left(\frac{\pi}{\lambda F_T} \frac{2y}{1+\sqrt{2}}\right) \right] \right\} \\ &+ \left\{ \frac{\sqrt{3}x}{\sqrt{3}x-y} \left[ \cos\left(\frac{\pi}{\lambda F_T} \frac{2y}{1+\sqrt{2}}\right) - \cos\left(\frac{\pi}{\lambda F_T} \frac{y+\sqrt{3}x}{1+\sqrt{2}}\right) \right] \right\} \end{aligned} \quad (4.3)$$

which can be recognised as the analytical results of taking the Fourier transformation of the aperture at the telescope/lenslet pupil to yield the field in the end-face of the fibre,  $\mathbf{E}_i$ , when illuminated with an atmospherically unaberrated plane wave at normal incidence. See section 5.2 for further details.  $\mathbf{r} = (x, y)$  in the plane of the fibre end face, and  $r = |\mathbf{r}|$ . For off axis sources replace  $x$  and  $y$  with  $(x-\delta x)$  and  $(y-\delta y)$ .  $F_T$  is the feed focal ratio into the plane of  $\mathbf{E}_i$  defined in terms of the diameter for the circular aperture, across the diagonal of the square aperture and between opposing vertices (i.e the longest internal distance) of the hexagon.  $k$  is the local wavenumber magnitude between aperture and fibre and  $\varepsilon$  is the obscuration of the telescope exit pupil, such that  $\varepsilon \in [0.0, 1.0]$ . Constant phase and amplitude terms<sup>[11]</sup> in  $\mathbf{E}_{c,s,h}$  cancel in Eq (2.29) whereas the quadratic phase curvature term is negligible even over the largest of LMA fibre cores. All three terms are thus omitted from Eqs. (4.1-3)

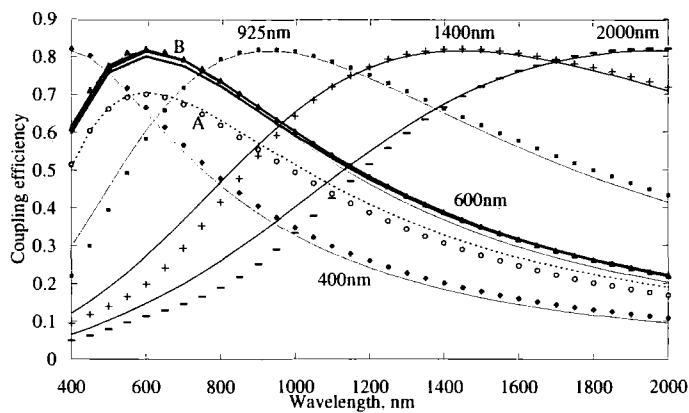
The fundamental mode of the LMA fibre does scale very slightly with wavelength and is also a polarisation doublet<sup>[12]</sup>. Since the photonic structure has a six-fold symmetry the boundary conditions at the silica/air-hole interfaces cause the field distributions of

the doublet to exhibit slight differences, however, the changes in coupling due to this and the wavelength scaling are of the order of  $<10^{-4}$  for all commercially available fibres, with  $\Lambda > 5\mu\text{m}$  and hence are ignored.

#### 4.2.1 On-axis coupling in ideal seeing

In this section we investigate the coupling efficiency of an on-axis source into an LMA fibre so that the telescope/lenslet PSF is centred on the fibre axis.

(a)



(b)

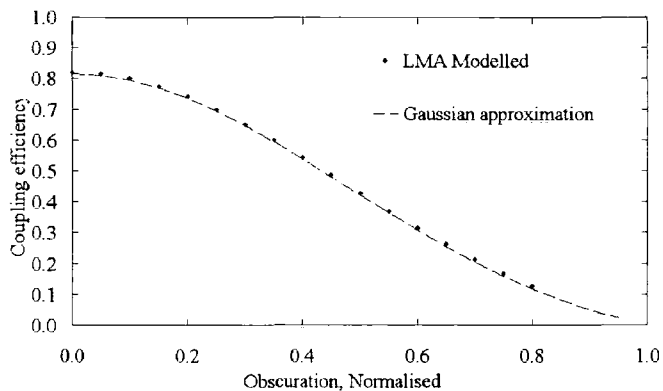


Figure 4.2 (a) The coupling efficiency of the fibre for circular, square and hexagonal lenslets. The continuous curves are the analytical results and the numerically calculated values shown as the data-points.[See text] Curves are shown for  $\lambda_{opt} = 400 \text{ nm}, 600 \text{ nm}, 925 \text{ nm}, 1450 \text{ nm}$  and  $2000 \text{ nm}$ . See text for further details. (b) The peak coupling efficiency of the obscured pupil as a function of obscuration,  $\epsilon$ .

The data-points in Fig.4.2(a) are of the spectral response of an LMA fibre to the obscured PSF, given by Eq.(4.1). Peak coupling, for the LMA fibre occurs only at one optimum wavelength,  $\lambda_{opt}$ , when the central lobe of the PSF and the mode of the fibre are best matched in distribution. The coupling decreases for  $\lambda \neq \lambda_{opt}$  due to the dependency of the size of the Airy pattern on  $\lambda$  and  $F_T$  compared to the essentially achromatic size of the LMA fibre mode. A flatter response can be made by using a step index fibre with its  $\lambda$ -dependent mode field size, see for instance the ideal seeing curve in Fig.4.6(b), but as noted in the introduction its attenuation spectrum is, generally, severely limited by comparison to the LMA case<sup>[3]</sup>.

The relationship between  $\lambda_{opt}$ ,  $F_T$  and  $\Lambda$ , the characteristic scale of the fibre used is given by the fit,

$$\lambda_{opt} = \xi \left( \frac{\Lambda}{F_T} \right) \quad (4.4a)$$

with

$$\xi = \begin{cases} 0.7911 \times \exp(0.6187 \times \varepsilon^{1.600}) & \text{Annulus} \\ 0.5964 & \text{Hexagon} \\ 1.2174 & \text{Square} \end{cases} \quad (4.4b)$$

where the obscuration,  $\varepsilon$  is fitted in the range from 0.0 to 0.6. Taking the useable pass-band to be 400-1800nm and  $\Lambda = 6.0\mu\text{m}$  and  $10.5\mu\text{m}$  of the Crystal Fibre A/S LMA-9-PM and LMA-16-PM fibres, respectively, the values of  $F_T$  in Eq. (4.4) range between  $\sim 2.6$  and  $\sim 21$ .

The mode field of the LMA can be approximated as a Gaussian out to the  $\sim 1/e^2$  point<sup>[13]</sup>. Shaklan and Roddier<sup>[4]</sup> have shown that the flux coupled into a single Gaussian mode in the image plane of an atmospherically unaberrated, perfect telescope can be computed exactly using Eq.(4.5), with the extension to arbitrary telescope obscuration, as given by Guyon<sup>[14]</sup>.

$$\rho(\delta r) = \frac{8}{\omega^2} \exp\left(-\frac{2\delta r}{\omega}\right) \left\{ \int dr \exp\left(\frac{r^2}{\omega^2}\right) I_0\left(\frac{2r\delta r}{\omega^2}\right) \right. \\ \left. \times \left[ J_1\left(\frac{\pi r}{\lambda F_T}\right) - \varepsilon J_1\left(\frac{\varepsilon \pi r}{\lambda F_T}\right) \right] \right\}^2 \quad (4.5)$$

where  $\delta r$  is the offset of the telescope PSF with respect to the fibre axis in the image plane of the telescope.  $I_0$  is the modified Bessel function of the first kind.  $\omega$  is the  $1/e$  width of the Gaussian mode field and Eq.(4.5) can be shown to be maximised for

$$\lambda = 1.4014 \left( \frac{\omega}{F_T} \right) \quad (4.6)$$

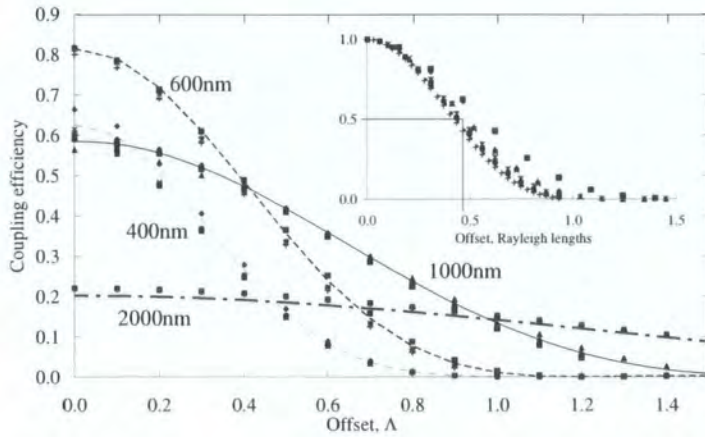
The continuous curves in Fig.4.4(a) are a result of the substitution of  $\omega = (0.5645 \lambda) \exp(0.6187 \times \varepsilon^{1.600})$  from Eq. (4.4), where  $0.5645 = 0.7911/1.4014$ , into Eq.(4.6) showing good agreement with the numerically computed data-points of the LMA case. This extends to the  $\varepsilon > 0$  case where the two curves labelled A are the numerically computed (data-points, Eq.(1),(4)) and analytical results (continuous curve, Eq.(8)) for the 25 per cent obscured pupil case, whereas panel (b) shows the maximum on axis coupling efficiency as a function of obscuration,  $\varepsilon$ .

Retaining the convention of numerically computed data-points and continuous curves computed using Eq. (4.5) in Fig.4, the bold curves marked B in panel (a) show that Eq. (4.5) can also be used to approximate the on-axis coupling efficiency of the hexagonal and square apertures. This can be understood on the basis that the coupling between the PSF and the mode of the fibre is dominated by the central lobe of the PSF which is similar enough in distribution to the circular case for Eq. (4.5) to provide a good approximation and so the spectral response is essentially the same as the annular aperture, except the small changes in peak coupling efficiencies which are ~82 per cent for the annular and hexagonal apertures and 80 per cent for the square aperture, subject also to the Fresnel loss. Section 2.4.1.

#### 4.2.2 Off-axis coupling in ideal seeing

The field of view (FOV) of a single-mode fibre is less well defined than for multi-mode fibres for whom the geometrical ray model is applicable. As the angle of incidence of the source plane wave increases in the telescope entrance pupil the resulting PSF moves off the telescope axis and with the fibre and telescope axes co-aligned, the coupling efficiency reduces in value.

(a)



(b)

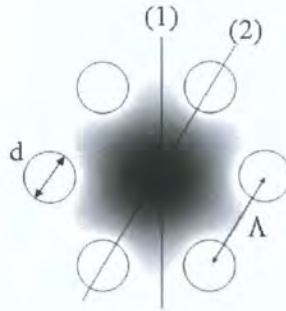


Figure 4.3 - A plot of the coupling efficiency as the PSF moves off the LMA fibre axis for various input wavelengths. The abscissa is in units of the characteristic width of the fibre,  $\Lambda$ , with the inset plot of  $\epsilon = 0.25$  and  $\epsilon = 0.40$  obscured annular pupils but with an abscissa in units of Rayleigh length ( $1.22F_T\lambda$ ) and normalised ordinate. The continuous curves shown represent the analytical result of Eq.(4.5) whereas the data-points are shown for the numerically computed cases of the circular, hexagonal and square PSF's moving over the PCF structure in directions (1) and (2) as shown in panel (b)

The single-mode field of view is thus defined by the input angle at telescope aperture at which the minimum acceptable coupling efficiency occurs. (Note that for non-zero input angles the incoming plane wave sees the telescope aperture as an ellipse, however, the range of input angles in astronomy is generally so small that any changes in the form of the PSF due this effect are generally ignored i.e. the aperture is assumed to be always circular)

Figure 4.3 is a plot of the field of view of the LMA fibre for the annular aperture, the square and hexagonal lenslets at rotations of 0, 15 and 30 degrees with respect to the photonic crystal structure. Numerical results are shown as data-points with analytical results shown as continuous curves. The Rayleigh length is defined as the distance  $1.22 F_T \lambda$  is the image plane. This is a highly convenient length scale, used throughout the thesis and should not be confused with the beam length in laser physics<sup>[18]</sup>.

The rotation(s) of the square and hexagonal apertures with respect to the LMA mode field cause changes in  $\rho_{max}$  of <0.3 per cent and so from this and the excellent correlation between square, hexagonal and circular, analytical and numerical results for both directions (1) and (2) at all input angles and wavelengths it would seem that the aperture shape and its orientation with respect to the highly non-azimuthally symmetric LMA mode, seems to have a minimal effect on the FOV. Further, as long as the correct substitution, from Eq.(4.4) is made, Eq.(4.5) seems to provide good quantitative results to within two to three percent for even the square and hexagonal apertures.

As Guyon<sup>[14]</sup> shows, the angular FOV for the coupling of an atmospherically unaberrated Airy pattern, from a telescope of primary diameter  $D_T$  into a step index fibre can be taken as approximately  $\lambda_{opt}/D_T$  and from the inset in Fig.(4.3a), the  $0.5\rho_{max}$  point is at  $2 \times 0.45 \times 1.22 \times \lambda_{opt}/D_T \approx \lambda_{opt}/D_T$  and hence this approximation can be used for the LMA case, fed with square and hexagonal lenslets, even over the very large 400nm-1800 nm waveband.

Notice that the FOV cannot be increased by choosing a larger  $\Lambda$ . Larger  $\Lambda$  implies smaller  $F_T$  for the same maximal coupling [see Eqs.(4.4)] and the linear trade off in one for the other ensures that the FOV at the telescope remains the same.

4.3 Coupling light with natural seeing

We now consider the case of PSF's aberrated by atmospheric turbulence. Several series of PSF's were generated using a Monte Carlo simulation and for each one the coupling integral was evaluated. For each PSF, the atmosphere was simulated as a randomly generated Kolmogorov phase screen <sup>[15]</sup> and the PSF was constructed using the far field approximation (by taking an FFT of the complex field in the telescope pupil). Perfect tip/tilt correction of the pupil phase was assumed, and the intensity in the telescope pupil was assumed to be uniform i.e. scintillation effects were not included.

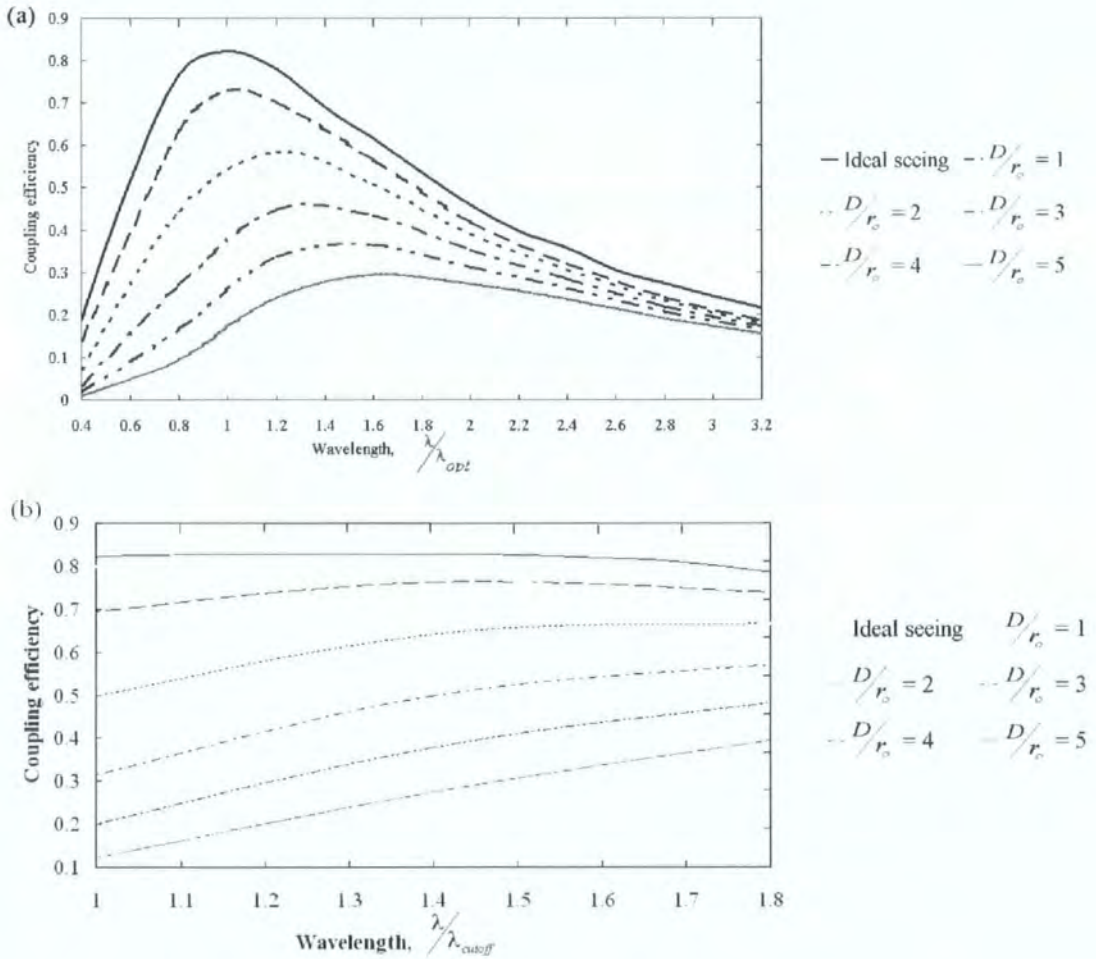


Figure 4.4 - Coupling efficiency against wavelength for various atmospheres (a) LMA fibre (b) Step index fibre of NA=0.13. Note the different x-axis scaling in each plot – For direct comparison see figures 4.5 and 4.6.

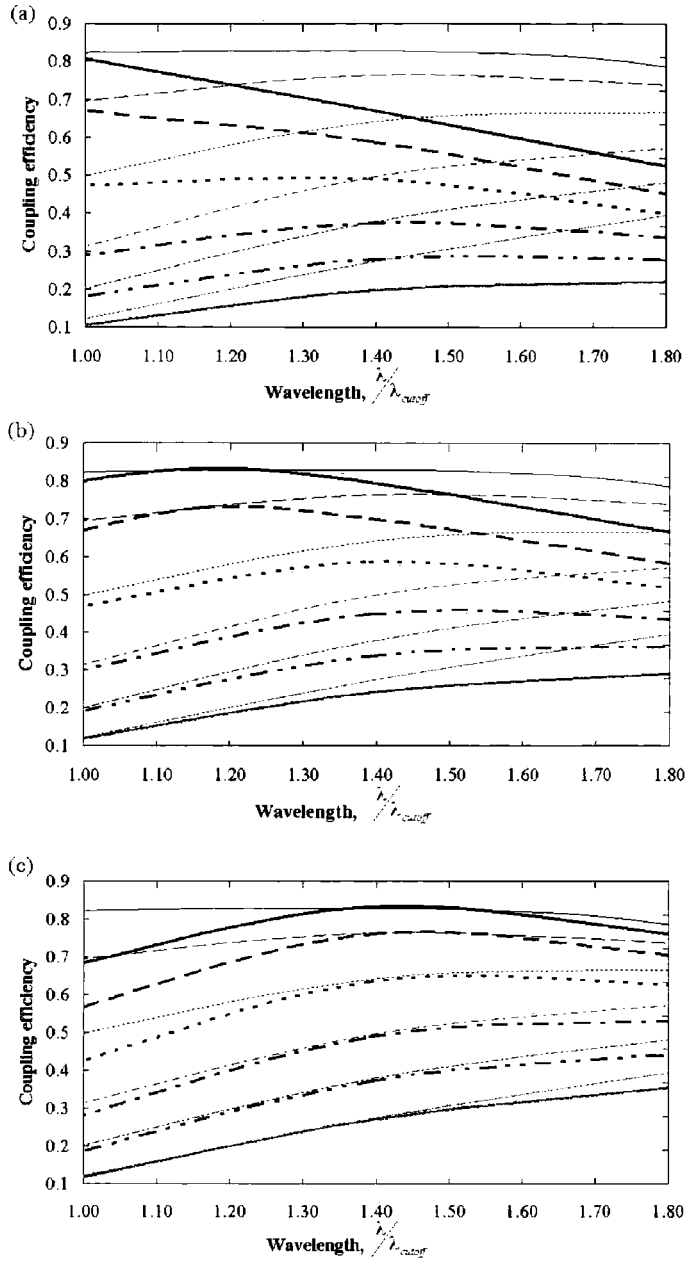
I have computed the expected theoretical maximum coupling efficiency into LMA and step index fibres (of numerical aperture,  $\Theta = 0.13$ ), for various values of  $D_T/r_0$ , where  $D_T$  is the telescope exit aperture diameter and  $r_0$  the Fried parameter<sup>[15]</sup> of the atmosphere. One thousand aberrated PSF's were computed per data point to yield a mean,  $\langle \rho \rangle$  and standard deviation,  $\sigma_\rho$ , coupling value.

LMA fibres are available in polarisation-maintaining (PM) form but with an almost identical mode field distribution to the non-PM fibres and this represents a significant advantage since the mode field distribution of step index PM fibres is typically non-rotationally symmetric, yielding a lower overall coupling from a circularly symmetric telescope. This analysis assumes a circular, non-PM step index fibre since this represents best case and some degree of PM performance can be induced in step index fibres using PM control techniques<sup>[16]</sup>.

Figure 4.4(a) shows the coupling efficiency against wavelength for the LMA fibre for various  $D_T/r_0$  with Fig 4.4(b) the same plot for the step index single-mode fibre for  $\lambda/\lambda_{cut-off} \in [1.0, 1.8]$ .  $D_T/r_0$  is specified at  $\lambda/\lambda_{cut-off} = 1.2$  in the step index case and at  $\lambda/\lambda_{opt} = 1.0$  in the LMA case. Note that the coupling response of the step index fibre is rather flatter than that of the LMA case. As we shall see this is due to the relative sizes of the passbands of the two fibre types and the relative scaling of the fibre-mode and incident telescope PSF with wavelength.

In order to properly compare the two fibre types the coupling responses must be plotted on the same axes as in Fig 4.5 for the case of a single step index and single LMA fibre and Fig 4.6 for the case of a single LMA fibre and multiple step index fibres.  $\lambda_A$  is the wavelength at which the atmospheric turbulence,  $D_T/r_0$ , is specified and  $\lambda_A/\lambda_{cut-off}$  is taken as 1.2 since many step index fibres have passbands that are limited to 1.05 to 1.35  $\lambda/\lambda_{cut-off}$ .

In order for the coupling responses to be plotted on the same axes, the peak step index fibre coupling wavelength, set using Eq. 4.6, was also set to  $\lambda/\lambda_{cut-off} = 1.2$ . Then three different  $\lambda_{opt}$  values, set using Eq.4.4(a), of  $\lambda_{opt}/\lambda_{cut-off} = 0.8 \lambda_A/\lambda_{cut-off}$ ,  $\lambda_{opt}/\lambda_{cut-off} = 1.0 \lambda_A/\lambda_{cut-off}$  and  $\lambda_{opt}/\lambda_{cut-off} = 1.2 \lambda_A/\lambda_{cut-off}$  are shown in Fig 4.5 panels (a), (b) and (c) respectively.



<i>LMA Fibre (Bold)</i>		<i>Step index Fibre</i>	
— Ideal seeing	<b>—</b> $D/r_c = 1$	— Ideal seeing	— $D/r_c = 1$
— $D/r_c = 2$	— $D/r_c = 3$	— $D/r_c = 2$	— $D/r_c = 3$
— $D/r_c = 4$	— $D/r_c = 5$	<b>—</b> $D/r_c = 4$	<b>—</b> $D/r_c = 5$

Figure 4.5 - Coupling efficiency against wavelength for step index and LMA fibres for (a)  $\lambda_{opt}/\lambda_{cut-off} = 0.8 \lambda_A/\lambda_{cut-off}$ , (b)  $\lambda_{opt}/\lambda_{cut-off} = 1.0 \lambda_A/\lambda_{cut-off}$ , (c)  $\lambda_{opt}/\lambda_{cut-off} = 1.2 \lambda_A/\lambda_{cut-off}$  where  $D_T/r_0$  is defined at  $\lambda/\lambda_{cut-off} = \lambda_A/\lambda_{cut-off} = 1.2$

The  $\lambda_{opt} / \lambda_{cut-off} = 1.0 \lambda_A / \lambda_{cut-off}$  and  $\lambda_{opt} / \lambda_{cut-off} = 1.2 \lambda_A / \lambda_{cut-off}$  cases are seen to be optimised in the ranges 1.10 to 1.30  $\lambda / \lambda_{cut-off}$  and 1.30 to 1.60  $\lambda / \lambda_{cut-off}$ , respectively, but the  $\lambda_{opt} / \lambda_{cut-off} = 0.8 \lambda_A / \lambda_{cut-off}$  case is a non optimal replacement for the step index fibre at any  $\lambda / \lambda_{cut-off} \geq 1.0$ , for any of the plotted  $D_T / r_0$ . Most commercially available step index fibres operate within the 1.05 to 1.35  $\lambda / \lambda_{cut-off}$  range, however some fibres, particularly some that operate in the NIR, have pass-bands in the range 1.00 to  $>1.80 \lambda / \lambda_{cut-off}$ . Therefore for the more restricted bandwidth step index fibre,  $\lambda_{opt} / \lambda_{cut-off} = 1.0 \lambda_A / \lambda_{cut-off}$  yields, generally, the most efficient coupling in any atmosphere, but for the broader range fibres,  $\lambda_{opt} / \lambda_{cut-off} = 1.2 \lambda_A / \lambda_{cut-off}$  should be used.

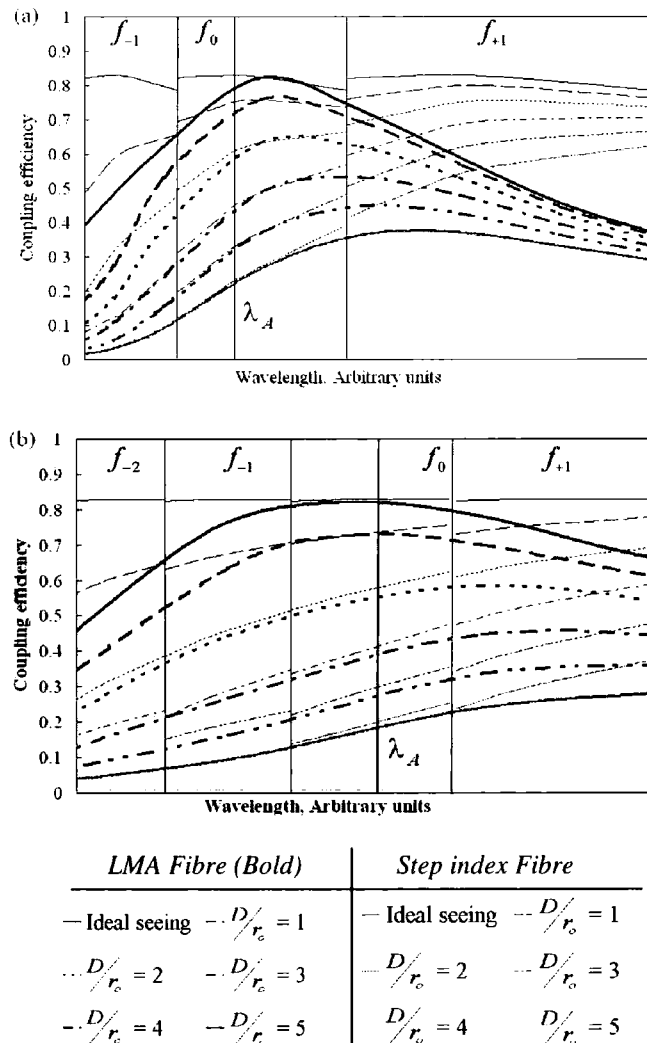


Figure 4.6 - Coupling efficiency against wavelength for a single LMA fibre and multiple step index fibres with pass-bands of (a) 1.00 to 1.80  $\lambda / \lambda_{cut-off}$  and (b) 1.05 to 1.35  $\lambda / \lambda_{cut-off}$ .

Note that whilst LMA fibre performance between 1.05 and 1.35  $\lambda/\lambda_{cut-off}$  is very similar to that of the step index alternative, the LMA fibre is a less desirable replacement for the broadband step index fibre in good seeing, although for  $D_T/r_0 \geq 2$  and  $\lambda_{opt} = 1.2 \lambda_A$  the LMA and step index characteristics are well matched over the entire 1.00 to 1.80  $\lambda/\lambda_{cut-off}$  range.

Figure 4.6(a) and 4.6(b) show how the coupling into a single LMA fibre compares with multiple step index fibres with useable passbands (a) 1.00 to 1.80  $\lambda/\lambda_{cut-off}$  and (b) 1.05 to 1.35  $\lambda/\lambda_{cut-off}$ , respectively. The pass-bands of the individual step index fibres,  $f_n$  are stacked sequentially in  $\lambda$  on the  $x$ -axes of Fig 4.6, without gaps, using

$$\lambda_n = \left(\frac{p}{q}\right)^n \lambda_{n=0} \quad (4.7)$$

for fibre  $f_n$ , where  $p$  &  $q$  are 1.80 & 1.00 and 1.35 & 1.05 for cases (a) and (b) respectively. The  $D_T/r_0$  values in the figure are specified at the  $\lambda_A$  point of the  $f_0$  fibre which again is specified at the point  $\lambda_A/\lambda_{cut-off} = 1.2$ .

In panel (a) the LMA fibre is optimised over the  $f_0$  step index fibre at  $\lambda_{opt}/\lambda_{cut-off} = 1.2 \lambda_A/\lambda_{cut-off}$  as in Fig 4.5(c) in order to try to maximise the LMA coupling with respect to the  $f_0$  step index coupling over the largest possible waveband and shows that since the LMA is not a good replacement for a single broadband step index fibre for  $D_T/r_0 < 2$  then its ability to replace many such fibres is equally poor. At  $D_T/r_0 \geq 2$  the performance of the LMA and the  $f_1$  step index fibre are approximately as inefficient as each other on the absolute coupling scale and so the LMA fibre can replace up to two step index fibres in this regime.

For the 1.05 to 1.35  $\lambda/\lambda_{cut-off}$  fibre more typically associated with the VIS, as in Fig. 3.8(b), the single LMA fibre with optimal  $\lambda_{opt}/\lambda_{cut-off} = 1.0 \lambda_A/\lambda_{cut-off}$  can be seen to be capable of replacing three step index fibres with near identical performance at  $D_T/r_0 \geq 2$  over fibres  $f_0$ ,  $f_1$  and  $f_2$ . For, fibre  $f_{+1}$  the  $D_T/r_0 \geq 2$  performance is better on the step index fibre and at  $D_T/r_0 < 2$  the LMA and step index performance in  $f_0$  is essentially identical but a drop in performance occurs for the LMA in  $f_1$ . However,

the generally reduced coupling in both of these cases might be acceptable on the basis of the single LMA fibre and its single set of fore-optics rather than the multiple instances of step index alternatives. Note also, that the mode field diameter (MFD) of, for instance the LMA-16 (Crystal Fibre A/S), optimised for use at  $>650\text{nm}$ , is  $15\mu\text{m}$ , approximately three times the size of even the largest commercially available step index fibre in the same waveband and so lower instrumental losses may be associated with the LMA fibre.

#### 4.3.1 Fibre feed focal ratio

The optimum feed focal ratio into the step index fibre was found to be  $f/4.3$ , regardless of  $D_T/r_0$  or  $\lambda$  for  $\Theta=0.13$ . (Similar to the  $f/5.1$  ratio found by Shaklan and Roddier<sup>[4]</sup> for an  $\Theta=0.11$  fibre).

The feed focal ratio into the LMA fibre depends on the application. For instance, taking fibre  $f_0$ , in figure 4.6(b) as the 780HP (Nufern) implies  $\lambda_{opt} = 807\text{nm}$ . In an application with a minimum desired wavelength of say  $400\text{nm}$  worst case, then the bend-loss characteristic<sup>[17]</sup> of the LMA fibre means that an LMA-8 (or polarisation maintaining equivalent) would be used, so from Eq. (4.4), with  $\varepsilon=0$ , a feed focal ratio of  $\geq 5.7$  would be required, with a slower input beam for  $\varepsilon > 0$  (e.g.  $F_T=6.1$  for  $\varepsilon=0.25$ ). However, if only a replacement for fibre  $f_0$  is required then a minimum of  $780\text{nm}$  implies, again by the bend-loss characteristic of the LMA fibre, the use of an LMA-16 and this means  $F_T \geq 10.75$ . So LMA fibres have the advantage of slower fore-optics requirements than the step index alternative, although the slower beam does require a higher degree of tip-tilt correction.

#### 4.3.2 Coupling variations with atmosphere

Figure 4.7 is a plot of the relative variation in efficiency,  $\sigma_\rho / \langle \rho \rangle$  at  $\lambda = 1.2 \lambda / \lambda_{cut-off}$  of  $f_0, f_{-2}$  and  $f_{+1}$  from Fig 4.6(b). The variance of fibre  $f_0$  increases with respect to the mean up to  $D_T/r_0 = 8$  where the resulting speckle pattern<sup>[15]</sup> has approximately equal mean and variance. The relative variance decreases with increasing  $\lambda$  since  $r_0 \propto \lambda^{6/5}$ <sup>[15]</sup>. These curves are plotted to highlight that the uncertainty at each wavelength is independent of the fibre type used even in the low  $D_T/r_0$  region of  $f_{-2}$  where the coupling efficiencies of the step index and LMA fibres are not well matched.

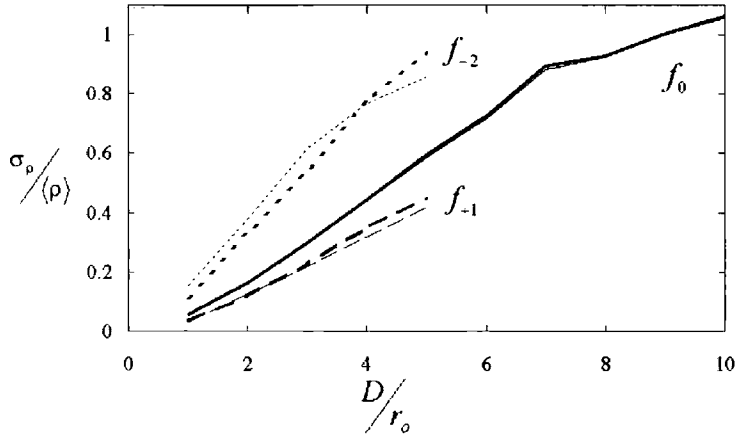


Figure 4.7 - The relative uncertainty at  $\lambda/\lambda_{\text{cut-off}} = 1.2$  of the step index fibres in Fig 4.6 (b) with the LMA values at the same wavelengths shown in bold. Key as per Fig. 4.5

Figure 4.8, shows that the field of view of the LMA fibre increases as the atmospheric degradation of the PSF increases. (The effect also occurs for the step index fibre, not shown). The inset is a normalised version of the main graph with the same abscissa shown to highlight the effect. The phenomenon occurs because as the amount of wavefront degradation increases the energy in the PSF spreads out in the image plane and the coupling of this 'wider' PSF is less sensitive to lateral offset with respect to the mode of the fibre. However, no real gain is made due to the significant decreases in coupling efficiency as the effect of the atmosphere increases.

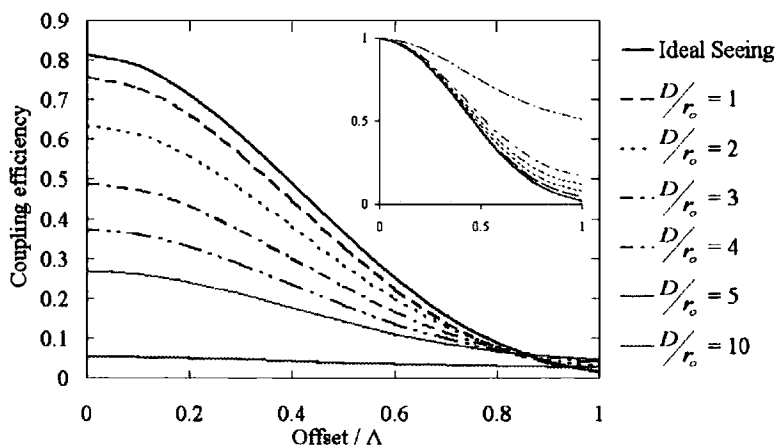


Figure 4.8 - The LMA fibre field of view as a function of  $D/r_o$  at  $\lambda/\lambda_{\text{opt}} = 1.0$ , with normalised version of the same data-set inset

The value of  $D_T/r_0$  is greatly increased for larger apertures and the coupling efficiency as a function of the number of corrected radial order (Zernike) modes is plotted in Fig 4.9 for  $D_T/r_0 = 20$  e.g. an 8m aperture in the mid NIR. The plot shows that at least 12 radial orders of correction are required in order to achieve >50 per cent coupling efficiency and hence fibre interferometry is not suited to large aperture telescopes without significant correction.

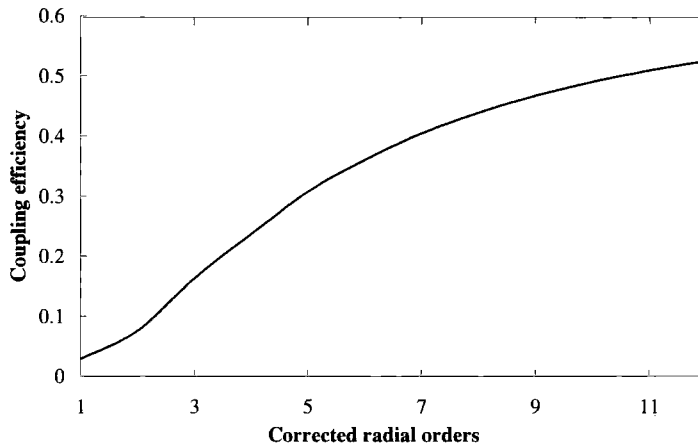


Figure 4.9 - Coupling efficiency at  $\lambda_{opt}$  with corrected (Zernike) radial orders for  $D_T/r_0 = 20$

#### 4.4 Defocused Airy results.

In this section the coupling efficiency of the telescope PSF into the near Gaussian fundamental mode is investigate as a function of the axial position,  $z$ . Linfoot & Wolf <sup>[11,18]</sup> have derived an analytical solution to the scalar field in the vicinity of the focus. Specifically at  $\pm z$  about the focal plane of the lens,

$$E_i(x, y) = De^{i\left(\frac{1}{2F_T}\right)^2 u} (C(u, v) - iS(u, v)) \quad (4.8)$$

where  $u = k_o(2F_T)^2 z$  and  $v = 2k_o F_T \sqrt{x^2 + y^2}$ .  $D$  is a constant and  $C$  and  $S$  are integral formulae for which Born and Wolf<sup>[11]</sup> provide an approximate analytical solution.  $k_o$  is the free space wavenumber and  $F_T$  the focal ratio of the telescope.<sup>7</sup>

Figure 4.10 shows what happens to the squared field as the position of the end face of the fibre is moved through and away from the focal plane.

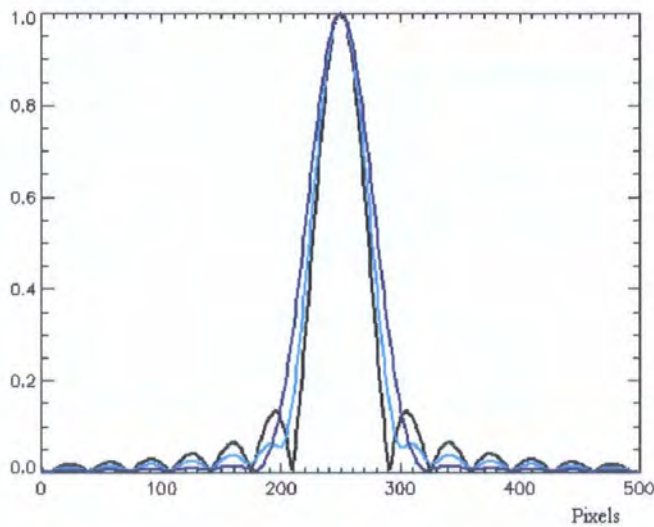


Figure 4.10 – PSF sections through their centres for (Black – at  $z = 0$ ), (Cyan – at  $z = -25\mu\text{m}$ ), (Blue –  $z = -50\mu\text{m}$ ),  $\lambda = 600\text{nm}$ ,  $\Lambda = 5.6$  (LMA-8). The  $x$ -axis is in pixels at an arbitrary physical scale.

Notice particularly the near Gaussian appearance of the image in the plane parallel to the focal plane but at  $z = -50\mu\text{m}$ . Figure 4.11 shows that the maximum theoretical coupling efficiency into an LMA fibre of an Airy pattern, 81%, can be increased, under certain circumstances, to  $\sim 98\%$ . ( $>99\%$  maximum coupling into a step index fibre is not shown).

<sup>7</sup> Incidentally, Born & Wolf consider Eq.(4.8) important enough to place a plot of it on the cover of the 7<sup>th</sup> (expanded) edition of Principles of Optics.

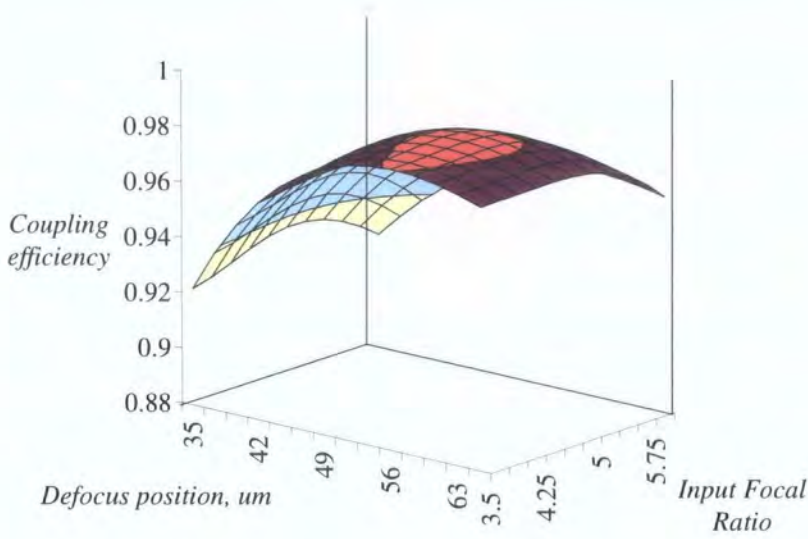


Figure 4.11 – The coupling efficiency as a function of input focal ratio and defocus position in the z (Axial) direction.  $\lambda_{opt} = 600\text{nm}$  and  $\Lambda = 5.6\mu\text{m}$  of the LMA-8 fibre.

From Eq.4.4  $F_T \lambda_{opt} = 0.7911\Lambda$  in the focal plane (Axial position = 0). From the pink region in Fig 4.11 the maximum coupling occurs for  $\sim f/4.5$  but taking  $f/5.0$  as a slower feed but with only an attendant  $1/10^{\text{th}}$  of a percent drop in coupling in comparison to the maximum means that the numerical constant in Eq.(4.4) must be reduced to, in this example,  $0.7911 \times (5.0000/7.3830)$  for the LMA-8 fibre at  $\lambda_{opt} = 600\text{nm}$ . The optimal defocus distance in this case is  $50\mu\text{m} = 10.0\Lambda$ . The wavelength coupling response is shown in Fig 4.12. Note the very high peak coupling value but the rapid fall-off in coupling for wavelengths about  $\lambda_{opt}$ .

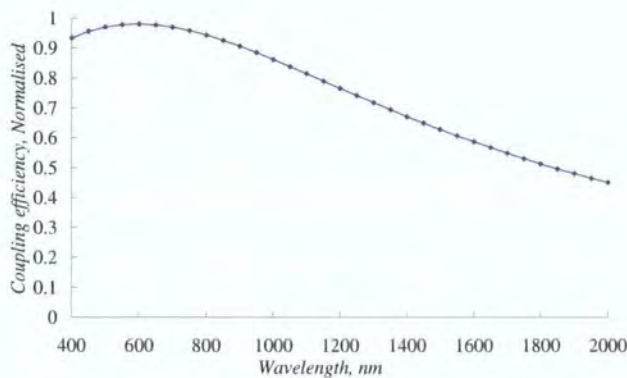


Figure 4.12 – The coupling efficiency against wavelength for an optimally defocused LMA-8 fibre fed at  $\lambda_{opt} = 600\text{nm}$ .

This analysis is taken no further here except to note that the increased speed of the telescope focal ratio required to match the de-focussed PSF with the LMA fibre still leaves its absolute value at  $>f/5$ . For larger fibres,  $\Lambda$  increases and therefore so does  $F_T$  even in the de-focussed regime. However, as found in section 4.3.1, the optimal feed focal ratio into step index fibres is typically quite fast ( $f/4.3$  for  $\Theta=0.13$  fibres) at focus and so implementing such a scheme is likely to be somewhat easier in the PCF case.

#### 4.5 Summary

The coupling efficiency of LMA PCFs in stellar interferometry has been examined. Despite the highly non-azimuthally symmetric component of the LMA fibre mode distribution, the Shaklan-Roddier formula for the coupling of starlight from the image plane of an arbitrarily obscured telescope is shown to be approximately applicable even for the PSF of hexagonal and square lenslets.

An atmospheric coupling comparison of LMA and step index fibres shows that an LMA fibre can be used either as a drop in replacement for single step index fibre whose passband is limited to  $\lambda/\lambda_{cut-off} < 1.35$ , with only marginal coupling losses by comparison or for multi fibre instruments as an excellent replacement for two fibres at  $D_T/r_0 < 2$  or three at  $D_T/r_0 \geq 2$ . The LMA is capable of replacing two broadband step index fibres with approximately the same coupling performance but only at  $D_T/r_0 \geq 2$ .

The LMA fibre is shown to require a slightly slower input focal ratio than the  $f/4.3$  of the step index fibres of  $NA=0.13$ , when replacing multiple single-mode step index fibres, but on replacing a single step index fibre the input focal ratio to the LMA fibre can be more than twice (i.e. slower) that of the step index, representing a considerable decrease in cost and complexity of the feed fore-optics.

Finally a deliberate defocus scheme was proposed and modelled and shown to increase the coupling efficiency to near unity for a 30% increase in the speed of the feeding optics in the diffraction limit. It was noted that the technique is rather better matched to the natural scales of LMA rather than step index fibres.

#### 4.6 References

- 1) 'An introduction to optical stellar interferometry', A Labeyrie, SG Lipson, P Nisenson, Cambridge, (2006)
- 2) 'Deriving object visibilities from interferograms obtained with a fiber stellar interferometer', V Coude du Foresto, S Ridgway, JM Mariotti, 1997, *Astron. Astrophys. Suppl. Ser.*, **121**, 379 (1997)
- 3) 'Bandwidth comparison of photonic crystal fibres and conventional single-mode fibres' M Nielson, J Folkenberg, N Mortenson and A Bjarklev. *Opt. Express* **12**, No.3 (2004)  
<http://www.opticsexpress.org/abstract.cfm?URI=OPEX-12-3-430>
- 4) Peryrilloux A, Pagnoux D, and Reynaud F, *Proc SPIE* **4838**, 1334 (2003)
- 5) 'Coupling starlight into single-mode fiber optics' S Shaklan, F Roddier, *Appl. Optics*, **27**, 2334 (1987)
- 6) 'Coupling of large telescopes and single-mode waveguides: application to stellar interferometry' C Ruilier, F Cassaing, *J. Opt. Soc. Am. A*, **18**, 143 (2001)
- 7) 'The radiated fields of the fundamental mode of photonic crystal fibers', Dabirian A., Akbari M., Mortensen N. A., *Opt. Express*, **13**, 3999 (2005)
- 8) 'Multipole method for microstructured optical fibre. I Formulation' T White, B Kuhlmeiy, R McPhedran, D Maystre, G Renversez, C Martijn de Sterke, L Botton. *J. Opt. Soc. Am. B* **19**, No 10 (2002)
- 9) 'Multipole method for microstructured optical fibre. II Implementation and Results' B Kuhlmeiy, T White, G Renversez, D Maystre, L Botton, C Martijn de Sterke, R McPhedran. *J. Opt. Soc. Am. B* **19**, No 10 (2002)

- 10) 'Symmetry and degeneracy in microstructured optical fibres'. M.J Steel, T.P White, C Martijn de Sterke, R McPhedran, L Botton. *Opt. Lett.* **26** No.8 (2001).
- 11) 'Principles of optics' Born and Wolf. 7<sup>th</sup> edition, Cambridge University Press.
- 12) 'Confinement losses in microstructured optical fibers' M Steel, T White, C De Sterke , R Mcphedran, L Botten, *Opt. Lett.*, **26**, 488 (2001)
- 13) 'Near-field to far-field transition of photonic crystal fibres: symmetries and interference phenomena'. N Mortensen and J Folkenberg. *Opt. Express* **10**, No 11 (2002) <http://www.opticsexpress.org/abstract.cfm?URI=OPEX-10-11-475>
- 14) 'Widefield interferometric imaging with single-mode fibres' O Guyon, *Astron. Astrophys.*, **387**, 366 (2002)
- 15) 'Adaptive optics in astronomy', Francois Roddier, Cambridge (1999)
- 16) 'Single-mode fiber **optics** in a long-baseline interferometer', S Shaklan, F Roddier, *Appl. Optics*, **26**, 2159 (1988)
- 17) 'Predicting macrobending loss for large-mode area photonic crystal fibres', M Nielsen, N Mortensen, M Albersen, J Folkenberg, A Bjarklev, D Bonacinni. *Opt. Express* **12**, No.8 (2004) <http://www.opticsexpress.org/abstract.cfm?URI=OPEX-12-8-1775>
- 18) 'Diffraction Images in Systems with an Annular Aperture', EH Linfoot & E Wolf, *Proc. Phys. Soc.* LXVI, I-B (1953)

# *Chapter 5*

---

## *Coupling starlight into PCFs - II*

### *Field lens feed*

#### **5.1 Introduction**

Since the mode of the LMA fibre is, to a good approximation wavelength independent in scale, the highly chromatic coupling of the Airy pattern into the LMA fibre mode was due to solely the chromatic scaling of the Airy pattern. (See Fig 4.2(a) for instance). However, a lenslet placed in the telescope image plane can be used to place an image of the exit pupil of the telescope on the fibre end face that also does not change scale with wavelength.

In this chapter we determine the coupling characteristics of a large mode area (LMA) photonic crystal, single-mode fibre when fed with an on-axis field lens used to place an image of the telescope exit pupil at the fibre input. Since, we know from section 3.5 that the coupling into the fibre is computed on an electromagnetic field basis, rather than the squared field, the optical model of the input field is presented in section 5.2. Section 5.3 then goes on to describe some of the basic characteristics of feeding single-mode LMA fibres with a field lens with a comparison of the direct and lenslet fed cases in section 5.4. Section 5.5 extends the case of a single lens feeding a single fibre to an array of SM fibres, possibly useful in high spectral resolution fibre fed spectroscopy and polarisation maintaining integral field spectroscopy. Section 5.6 describes the experimental steps undertaken to falsify the central result of section 5.3, also providing further verification of the coupling integral in general terms and specifically, its application to photonic crystal fibres.

## 5.2 The optical model

As noted in previous chapters, the coupling efficiency into a single mode fibre is governed by the electric field and hence we need to determine the *electric* field of the telescope exit pupil image. The generalised optical model used in this analysis is shown in Fig 5.1.

The field  $t$ , in the planar surface,  $S_1$  propagates the distance,  $d$  to the optical element ① which is monolithic in the  $(x-y)$  plane and is characterised by some positive value of optical power and a limiting, diffracting aperture assumed to be circular. The field passes through the lens and is then allowed to propagate the distance  $f$ , to the quadratic image surface,  $S_2$ .  $A$  is the infinite plane containing the fibre end-face.  $A$  and  $S_1$  are coincident at the  $z$ -axis and  $E_i$ , the field in the plane of  $A$  is given by Eq. 5.1,<sup>[1]§§</sup>,

$$E_i(u, v) = D \exp\left\{\frac{ik}{2f}\left(1 - \frac{d}{f}\right)(u^2 + v^2)\right\} \times \int_{-\infty}^{\infty} \int_{-\infty}^{\infty} t(\varepsilon, \eta) P\left(\varepsilon + \frac{d}{f}u, \eta + \frac{d}{f}v\right) \exp\left\{-\frac{ki}{f}(\varepsilon u + \eta v)\right\} d\varepsilon d\eta \quad (5.1)$$

Where  $k$  is the wavenumber magnitude in the region between ① and  $A$ .  $P$  is the aperture function which is the projection of the aperture stop of the system onto the  $(\varepsilon, \eta)$  plane and is unity inside the stop and zero valued otherwise.  $t(\varepsilon, \eta)$  is the transmittance of the input field.  $D$  is a constant phase term.

---

§§ This analysis is scalar and therefore the choice of  $E$  instead of  $H$  is arbitrary.

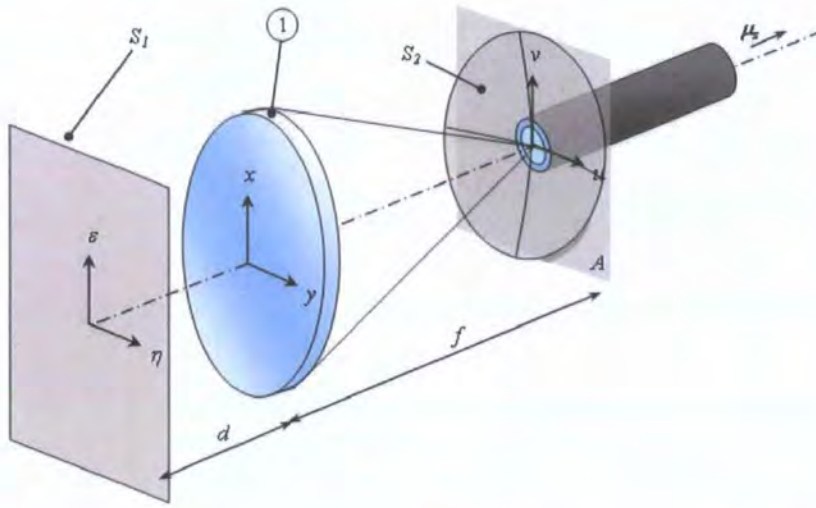


Figure 5.1 - The generalised optical model used in this analysis.

In the case of an Airy pattern fed into the fibre,  $d = 0$  and component ① is the telescope itself.  $E_i(u, v)$  then reduces to the Fourier transform of the aperture function of the telescope multiplied by  $\exp\left(\frac{ik_o}{2f}(u^2 + v^2)\right)$ . This is the spherical term commented upon in section 4.2.

In the lenslet fed case, it is usually found that telecentric foreoptics are required in order that off axis lenslets are not overfilled in angle. This is dealt with in some detail in section 5.6.1 of this chapter. For now, as Fig 5.2 shows, in the same way that a complete telescope, often comprising many different optical elements, can be reduced to a single lens for analysis, then a system that is telecentric in its image, can be reduced to a single lens and a stop in the front focal plane.

For this analysis note that  $|d| = |f|$  and further from the same figure, the aperture stop of the system is always the stop in the front focal plane. Therefore  $P = 1$  for all points in the image and Eq. (5.1) reduces to

$$E_i(u, v) = D \int_{-\infty}^{\infty} \int_{-\infty}^{\infty} t(\epsilon, \eta) \exp\left\{-\frac{ki}{f}(\epsilon u + \eta v)\right\} d\epsilon d\eta \quad (5.2)$$

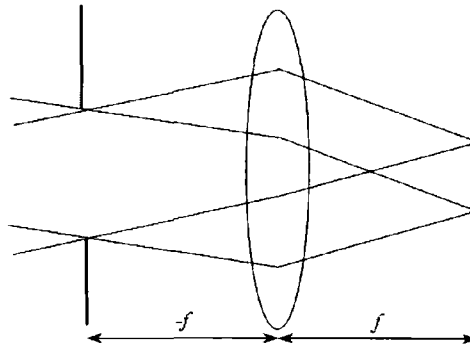


Figure 5.2 – The telecentric system can be modelled as a single lens, an image at focal length,  $f$ , and the aperture stop of the system in the front focal plane at  $-f$ .

Thus, in the lenslet feed case, the PSF of the telescope resides in  $S_1$ , with no spherical term present. Applying Eq. 5.1, now to the lenslet,  $d = 0$  and therefore  $P = 1$  for all points in the image, and a Fourier relationship between  $S_1$  and  $S_2$  exists. The telescope PSF in  $S_1$  is vignettted by the aperture of the lenslet and this effect causes diffractive features to appear in the telescope pupil image on the fibre end-face. Further, by the convolution theorem, since  $S_1$  is the multiplication of the telescope PSF and the pupil function of the lenslet then  $S_2$  can be taken as the convolution of the telescope pupil image and the PSF of the lenslet. Projecting  $S_2$  onto  $A$  then yields a multiplicative spherical term and the pupil image is taken as,

$$E_i(x, y) = \exp\left(\frac{ik_o}{2f}(u^2 + v^2)\right) h \otimes E_g \quad (5.3)$$

where  $E_g$  is the geometrical image of the telescope entrance pupil,  $h$  is the PSF of the lenslet in the  $(u, v)$  plane. Eq.(5.3) is the equation used to create the input fields throughout.

Finally, the following functional diagram is referenced throughout much of the rest of the chapter.

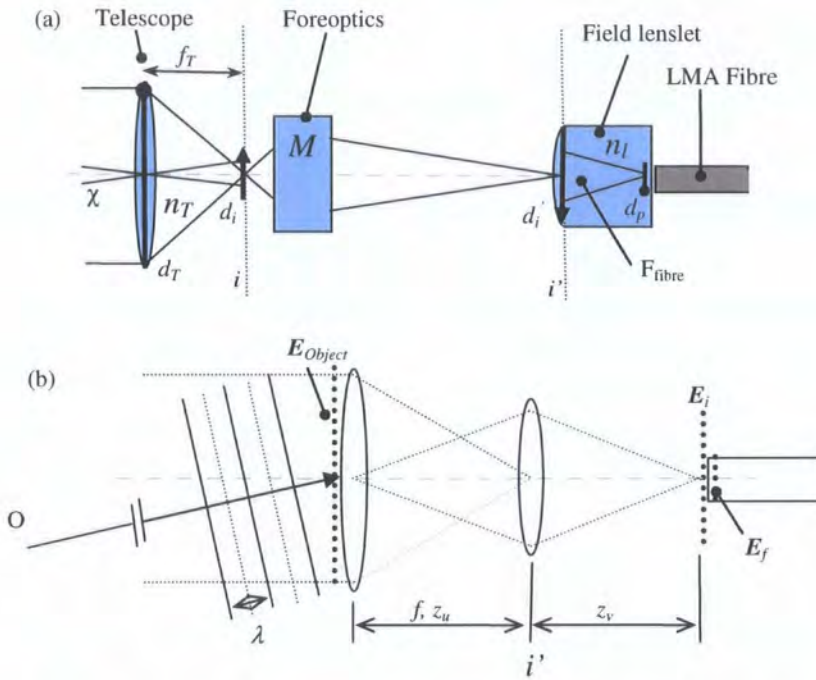


Figure 5.3 – (a) The optical model nomenclature, (b) the field nomenclature - In (b) the telescope lens is assumed to include the telecentric foreoptics.

### 5.3 Characteristics of the field lens feed

This section quantifies the coupling efficiency due to parameters such as pupil image scale, telescope obscuration, incident wavelength which are seen to affect primarily the maximum coupling value (Section 5.3.1). Changes in coupling due to increasing input angle at the telescope are then found and used to derive the field of view (FOV) of this configuration. (Section 5.3.3).

#### 5.3.1 On axis source

Figure 5.4 shows a 3D representation of the field magnitude of the fibre mode and an overplot of cross sections of the fibre mode and incident field, through their shared axis. The geometric image of the pupil,  $E_g$  of diameter  $d_p$ , Fig.5.3, on the end face of the fibre is shown as the un-diffracted case.

As the focal ratio of the lenslet increases or the wavelength increases for the same lenslet, the subsequent size of the lenslet PSF,  $h(p,q)$  with respect to  $E_g$  increases, as the cross sections in the figure show. The least and most diffracted cases in the figure are of an  $f/2$  lenslet at  $\lambda=400\text{nm}$  and an  $f/4$  lenslet at  $\lambda=2000\text{nm}$ , respectively, and so  $d_p$  is generally small enough, for any commercially available fibre, that the convolved pupil image,  $E_i(p,q)$ , Eq. (5.3) can be significantly affected.

The aperture of the lenslet will partially vignette the PSF of the telescope causing a loss in total throughput. However this does not effect the coupling efficiency *at the fibre* and hence is explained fully and quantified in sections 5.3.4 and 5.3.5 and ignored for clarity here.

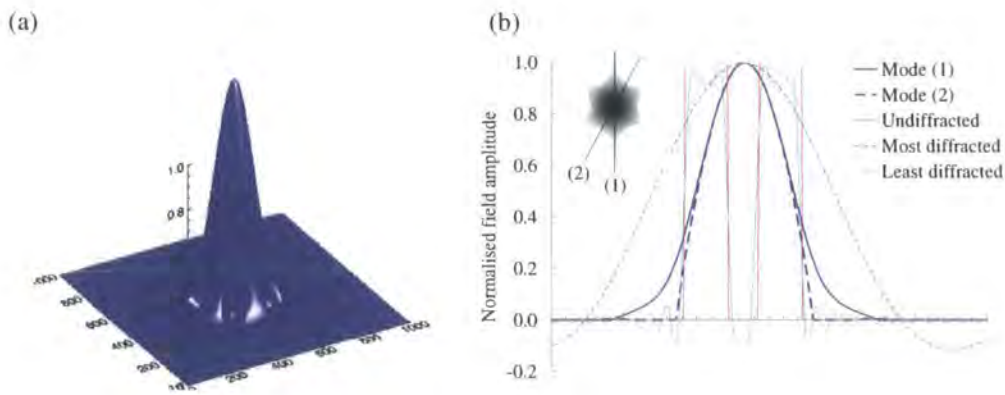


Figure 5.4 – (a)  $|E_f|$  shown in 3D, (b) cross section through the fibre mode and various images of the pupil at the end face of the fibre

Figure 5.5 shows the maximum coupling efficiency, due to an on axis source,  $O$  in Fig 5.3, as a function of telescope exit pupil image size,  $d_p$ , telescope obscuration and lateral offset of the pupil image with respect to the mode field of the fibre. These figures represent maximum coupling efficiencies since off axis sources couple less efficiently due to the phase mismatch between  $E_i$  and  $E_f$ . (Section 5.3.3).

In Fig. 5.5(a), the maximum coupling values change between the least and most diffracted cases due to the effect of  $h(p,q)$  as it scales with respect to  $E_g$ . The least diffracted curve peaks at  $1.33\lambda$  with the most diffracted image of interest, taken as  $\rho_{\max} > 50\%$ , showing a very weak dependence on image diameter, due to the dominance of the lenslet PSF over the image scale in these cases.

Increasing obscuration reduces coupling as shown in Fig – 5.5(b), as the mismatch between the missing central portion of the primary image and the centrally located mode becomes more severe. Fig. 5.5(c) shows that the coupling is highly sensitive to lateral alignment of the pupil image and the fibre mode. A drop in maximum coupling efficiency of approximately 10% occurs for only a  $0.25\lambda$  lateral shift and for an LMA-8 fibre this equates to an alignment precision between fibre and lenslet axes of  $\sim 1.6\mu\text{m}$  rising to a few microns for the LMA-20. Alignment tolerances of this order are discussed by Liu *et al* <sup>[2]</sup> and whilst technologically challenging, are possible.

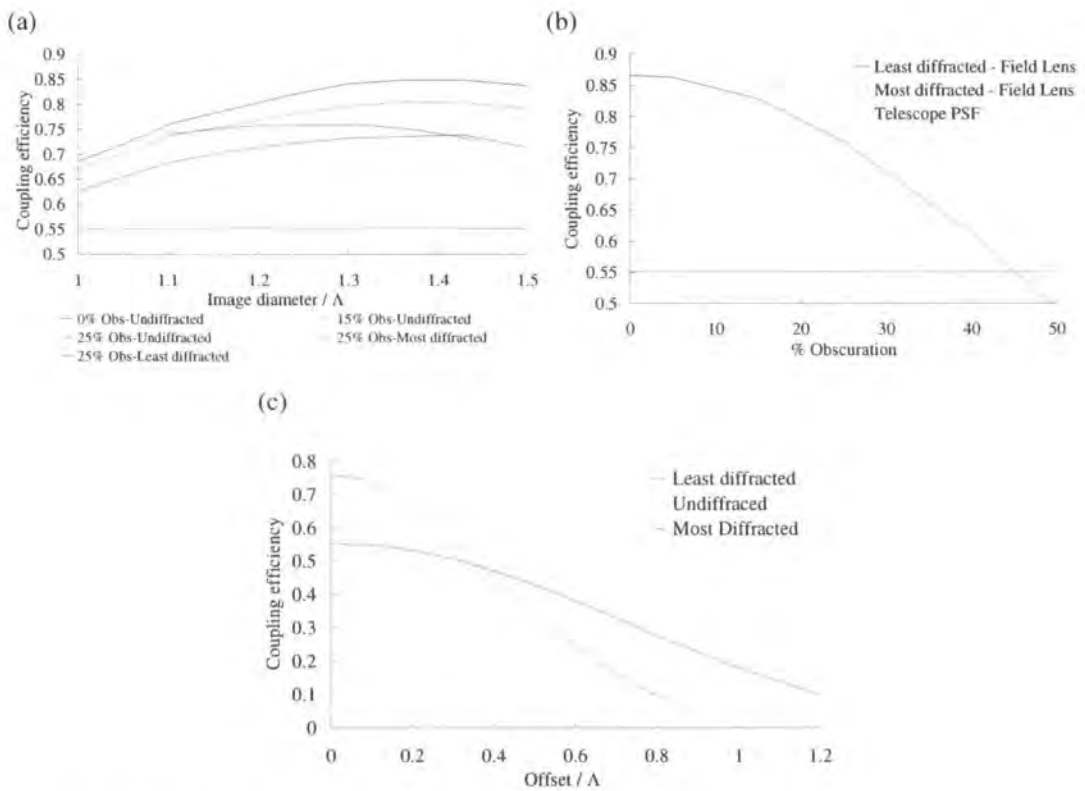


Figure 5.5 - (a) Maximum coupling,  $\rho_{\max}$  (i.e. on axis  $O$ , in fig 2) characteristics as a function of pupil image scale, (b)  $\rho_{\max}$ , as a function of telescope obscuration, (c)  $\rho_{\max}$ , as a function of pupil offset for geometric, diffracted and badly diffracted cases. For a lenslet not in contact with the fibre, these values must be reduced by the Fresnel coefficient as noted in section 5.2.

The values of maximum (on-axis) coupling efficiency with wavelength for various feed focal ratios into the pupil image are investigated with comparison to the direct feed case in section 5.4.

### 5.3.2 Gaussian apodisation

Gaussian (amplitude) apodisation of the pupil image was attempted in order to increase the coupling efficiency into the LMA mode which, itself, can be approximated as a Gaussian in the region inside the holey structure<sup>[3]</sup>. Figure 5.6 shows the result of increasing the Gaussian half width of the apodising screen with respect to the diameter of the pupil image,  $d_p$  (each pair of curves) and of increasing the size of  $d_p$  wrt to the static mode field of the LMA fibre (the three sets of curves). Both the transmission and coupling curves are asymptotic to the  $x$ -axis and hence Gaussian apodisation works to reduce the overall coupling.

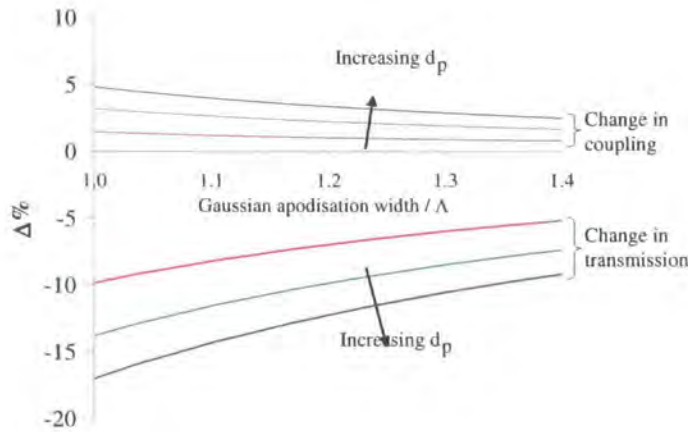


Figure 5.6 The effect of Gaussian pupil apodisation on the overall throughput,  $\Delta\%$ . The three curve sets are for increasing values of  $d_p$ , the diameter of the geometrical pupil image,  $E_g$  on the end face of the fibre wrt to the static mode field of the LMA fibre.

### 5.3.3 Off axis source.

Referring to Fig 5.3, the pupil of the telescope illuminated by an off-axis source,  $O$ , and its *geometrical* image on the fibre end face can be modelled (in one arbitrary polarisation state, along the  $y$ -axis, say) as a flat obscured disc,  $P$ , modulated by a cos term in  $\lambda, n, \theta$  the angle *at the fibre* associated with the off axis source  $O$  and  $y$ , the distance from the telescope axis, yielding a term  $P \cdot \exp(ikny\theta)$ . Variables,  $y$  and  $\theta$  are then linearly related and the much reduced magnitude of  $y$  across the extents of the image w.r.t. to the enormous values of  $y$  in the telescope pupil can be matched by the exact reciprocal scaling in  $\theta$  for the same value of the exponential term. This is simply

an expression of the conservation of etendue for the telescope exit pupil and its (geometrical) image due to the invariance of  $\lambda$  in all space (subject to bulk changes in refractive index,  $n$ ).

As  $\theta$  increases a phase mismatch between the fibre and incident fields occurs which causes the coupling efficiency to fall off in the manner shown in Fig.5.7. The fibre coupling field of view is then defined as the angle at which the coupling efficiency,  $\rho_f(\theta)$  falls below some absolute value.

As noted in the previous section, the PSF of the telescope will be vignetted, even at  $\theta = 0$ , by the lenslet aperture and indeed one can view this process as giving rise to the diffraction in the pupil image on the fibre end face<sup>[1]</sup>. Further, the amount of energy lost to this process will, of course, increase as the telescope PSF is displaced in  $i'$  wrt to the lenslet, for off axis sources and so the total field of view can be expressed as

$$\rho(\theta) = \rho_f(\theta) \cdot \rho_s(\theta) \quad (5.4)$$

where the subscripts  $f$  and  $s$  refer to the fibre coupling efficiency and vignetting the loss due to the lenslet aperture stop.

Any constant amplitude terms in  $E_i$ , for instance the amplitude of  $h$  or  $E_g$ , cancel top and bottom in Eq. (2.29) and the power relationship between  $E_{Object}$  and  $E_f$  is lost leaving only  $\rho_f$ , the *ratio* of the powers in  $E_i$  and  $E_f$ . For instance if  $\rho_f = 0.5$  then 50% of the energy incident at the end face of the fibre is coupled into the fibre. The power ratio between  $E_{Object}$  and  $E_i$  is then given by  $\rho_s$  and the total throughput from telescope entrance pupil to fibre mode by Eq. (5.4). The separation of the two terms on the *RHS* of Eq. (5.4) is therefore justified and further, whose individual derivations are physically relevant and instructive. See sections 5.3.4/5.  $\rho(\theta)$  itself is investigated in section 5.4.

#### 5.3.4 Coupling due to the fibre, $\rho_f(\theta)$

Figures 5.7(a) and 5.7(b) show the  $\rho_f(\theta)$  characteristics for coupling into an LMA-8 and LMA-15 fibre.

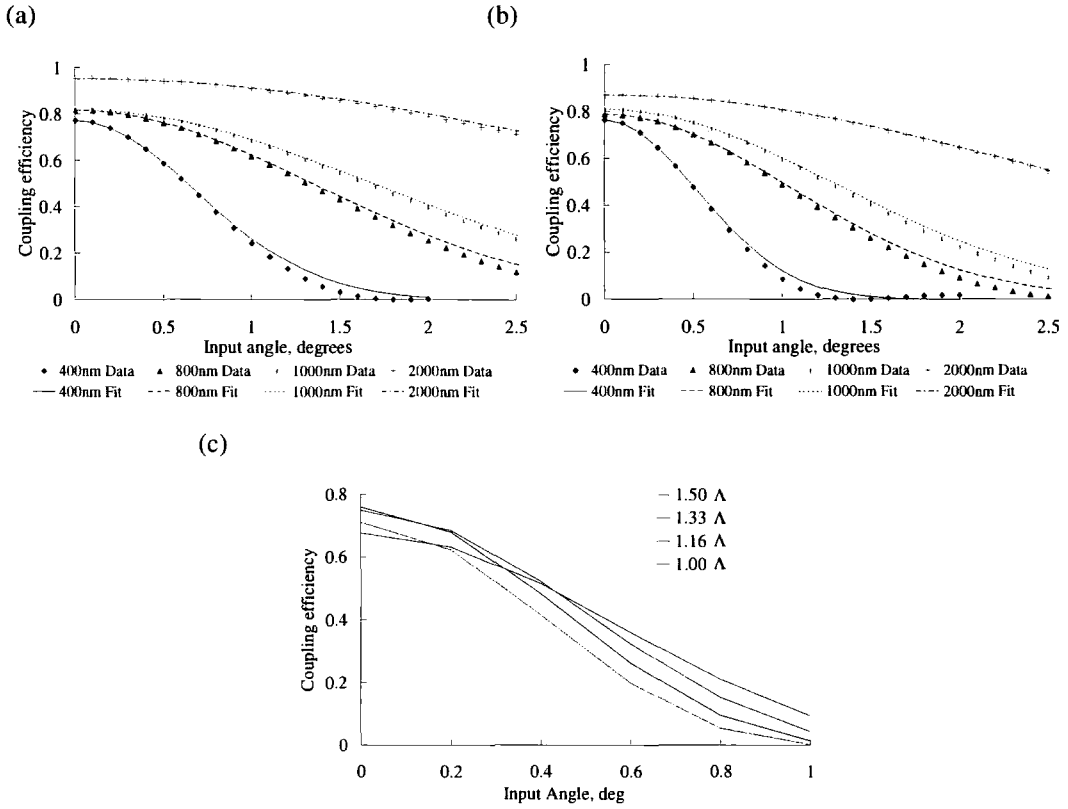


Figure 5.7. Coupling efficiencies as a function of input angle for (a) LMA-8, (b) LMA-15 for  $d_p = 1.33\Lambda$  and (c) as a function of  $d_p$ . All angles are given in degrees at the fibre end face and all wavelengths in nm.

A fit to the curves, accurate to a few percent for  $\rho > 0.3$ , is overplotted in Fig 5.7, given by

$$\rho_f(\theta) = \rho_{max} \cdot \exp \left[ - \frac{\left( \theta \cdot \frac{n_l}{n_{core}} \right)^2}{2 \left( \zeta \left( \frac{\lambda_o}{n_l \Lambda} \right) \right)^2} \right] \quad (5.5)$$

where,  $\rho_{max} = \rho_f(\theta=0)$  is the maximum coupling value,  $n$  is the refractive index at the fibre end face,  $n_{core}$  is the refractive index of the fibre core,  $\Lambda$  is the characteristic length of the photonic structure in the fibre,  $\lambda_o$  is the free space wavelength and  $\zeta$  is a numerical constant of value 13.832 when  $\theta$  is in degrees. As noted in section 5.3.1,  $\rho_{max}$  changes due to the wavelength dependent scaling of  $h$  with respect to  $E_g$ .

Figure 5.7(c) is a plot of  $\rho(\theta)$  for various pupil image sizes,  $d_p$ , on the fibre end face. From the plot,  $\rho(\theta)$  can be increased/decreased slightly with a corresponding decrease/increase in image size. However, since  $\rho_{max}$  also affects the effective FOV, see equation 5.8 below, then the combination of  $\rho_{max} \times \rho(\theta)$  is found by inspection to yields the largest FOV when  $d_p = 1.33\lambda$ .

In terms of the fractional loss of efficiency  $\gamma$ , where  $\{\gamma \in [0.0, 1.0]: \gamma < \rho_{max}\}$ , Eq.(5.5) can be rearranged to yield,

$$\theta = \frac{n_{core}}{n^2} \zeta \left( \frac{\lambda_o}{\Lambda} \right) \sqrt{-2 \ln \left( 1 - \gamma / \rho_{max} \right)} \quad (5.6)$$

and since  $F = 1/2\theta$  and converting from radians to degrees the associated focal ratio at the fibre,

$$F_{fibre} = \frac{90n^2 \Lambda}{\zeta \pi n_{core} \lambda_o \sqrt{-2 \ln \left( 1 - \gamma / \rho_{max} \right)}} \quad (5.7)$$

Now that we have typical values for the required geometric pupil image size and feed focal ratio to the fibre we can calculate the fibre field of view *on the sky* for the given telescope configuration. In Fig 5.1, the conservation of etendue can be used to derive the angular scale between the telescope exit pupil and its geometrical image such that

$$\frac{nd_p}{n_T d_T} = \chi F_{fibre} \Rightarrow \chi = \left( \frac{n}{n_T} \right) \frac{d_p}{F_{fibre} d_T} \quad (5.8)$$

Equation (5.8) is the angular relationship between fibre and sky and holds regardless of the fact the image on the end face of the fibre is diffracted. Substituting in  $F_{fibre}$ , the critical focal ratio associated with a maximum coupling loss of  $\rho_{max} - \gamma$ ,  $d_p = 1.33\lambda$

and converting units of the angular un-obscured Rayleigh length,  $L_R = 1.22\lambda_o / nd_T$ , yields,

$$\chi / L_R = \left( \frac{n_{core}}{n_T} \right) 0.5263 \sqrt{-2 \ln \left( 1 - \gamma / \rho_{max} \right)} \quad (5.9)$$

Equation (5.9) is an extremely interesting result since it says that when feeding the single-mode LMA fibre with a field lens, Fig 5.3, the **sample size on the sky is independent of the size of the fibre core**, associated with the characteristic size of the fibre,  $\lambda$ . This result can be understood on the basis that a larger core implies a larger  $|y_{max}|$  in  $\exp(ikny\theta)$  and therefore requires a smaller  $\theta$  for the same value of this term. Therefore as the core grows, the maximum input angle (for the same  $\lambda$ ) gets proportionately smaller and hence  $\chi$  remains constant.

The image plane ( $i$  to  $i'$ ) magnification of the foreoptics,  $M_f$  can also be computed

using  $M_f = d'_i / d_i = d'_i / \chi f_T$  where  $f_T$  is the focal length of the telescope and substituting in (5.9) yields,

$$M_f \equiv \left( \frac{n_T}{n} \right) \frac{d'_L}{1.33\lambda} \left( \frac{F_L}{F_T} \right) \quad (5.10)$$

$d'_L$  is the total aperture size in metres of the lenslet of focal ratio  $F_L$ , where the approximation that the minimum focal ratio into the pupil image on the end face of the fibre is that of the lenslet itself, since  $z_v \ll z_u$  in Fig.5.3.

So to keep  $M_f$  to a reasonable figure, say  $\leq 10$  and assuming that  $F_L \geq 2$  then for an LMA-8 fibre,  $d_L \leq 260\mu\text{m}$  for  $F_T = 7$  and  $d_L \leq 600\mu\text{m}$  for  $F_T = 16$ , assuming that  $n = 1.00$  and  $d_L \leq 600\mu\text{m}$  for  $F_T = 7$  and  $d_L \leq 1400\mu\text{m}$  for  $F_T = 16$  for the LMA-20. So significant foreoptics magnifications are required to implement the pupil imaging scheme with a macroscopic field lens with lower  $M$  required for smaller lenslets of course.

### 5.3.5 Coupling due to the lenslet, $\rho_s(\theta)$

As the telescope PSF moves over the plane of  $i'$  it is stopped by the finite aperture of the field lens and this creates an extra term  $\rho_s$  in the off axis coupling efficiency.  $\rho_s$  can be computed for any aperture using,

$$\rho_s = \frac{\int_{\text{Aperture}} |E(\mathbf{r} - \delta\mathbf{r})|^2 d\mathbf{r}}{\int_{\infty} |E(\mathbf{r})|^2 d\mathbf{r}} \quad (5.11)$$

which is simply the ratio of energy passed through the lenslet as a fraction of the total field energy, where  $E$  is the Airy pattern as specified by Eq 4.1, and  $\delta\mathbf{r}$  is the offset in  $i'$  of the centre of  $E$  from the telescope axis, dropped from the denominator since integrated over the infinite plane.

## 5.4 Comparison of direct and field lens coupling

In this section we bring together the effects of  $\rho_f$  and  $\rho_s$  on the coupling into the fibre using a field lenslet and compare these results with the case where the telescope PSF is fed directly into the fibre.

$S$ , the sampling constant, is defined in the following manner. From the conservation of etendue,  $\chi d_T = 1/F_l d_f n_l$  where  $d_T$  is the telescope primary diameter,  $d_f$  the image diameter at the fibre end face,  $n_l$  and  $F_l$  the lenslet refractive index, (e.g. 1.45 if the lenslet is in contact with the fibre end face) and focal ratio, respectively and  $\chi$ , the field of view of the lenslet on the sky. The use of the conservation principle is valid here since the expression is constructed solely from geometrical parameters. Defining  $d_l = S \times 1.22 F_T \lambda$  substituting these two expression into each other and rearranging yields,

$$F_l = \frac{1.33 \Lambda n_l}{1.22 S \lambda} \quad (5.12)$$

Hence the  $S=1$  case Nyquist samples the diffraction limited PSF out to the Rayleigh length,  $1.22F_T\lambda$ . This choice is entirely arbitrary of course and any desired measure of PSF width can be chosen by simply altering the value of  $S$ . Note that since Eq.(5.12) is the sample size of the lenslet then it is natural that it should have no dependence on  $\gamma$  or  $\rho_{\max}$ .

The smallest  $S$  and hence the largest effect of Eq.( 5.12) occurs for the smallest  $A$ . Figure 5.8(a) is an overplot of  $\rho_s$  and  $\rho_f$  for the LMA-8 fibre with  $F_L = 2$ , with a telescope obscuration of 25%. Looking first at the on-axis,  $\theta = 0$  values, the fibre coupling  $\rho_f \sim 96\%$  at 2000nm is due to the excellent match of the  $f/2$  PSF at this wavelength and the fibre mode however, the value of  $\rho_s$  at this wavelength is 76% yielding the total coupling of  $\sim 73\%$ . However, at 400nm  $\rho_f$  has a value of  $\sim 75\%$  but a  $\rho_s$  of 96% and so as the fibre coupling,  $\rho_f$  increases with increasing wavelength, the maximum (on-axis) lenslet coupling,  $\rho_s$  decreases at approximately the same rate leaving  $\rho(\lambda)$  in Fig.5.8(b) *essentially flat across the whole of the visible–NIR*.

Compare this with the coupling characteristics of the direct feed case plotted with the field lens curves in Fig.5.8(b) where the shape of the coupling curve is due to the wavelength dependent telescope PSF coupling into the wavelength independent mode field of the LMA fibre. From Fig 5.8(b), the maximum lenslet and direct feed coupling efficiencies are approximately the same for different values of the telescope obscuration.

The fibre mode of a step index fibre is also wavelength dependent and it is possible to arrange a relatively flat response with a direct feed however, the attenuation spectrum of a typical step index fibre that is single-moded at 400nm is very limited<sup>[3]</sup> whereas the LMA fibre has low attenuation over the whole visible & NIR range and so *only the LMA fibre, when fed with a lenslet can be used to couple the entire visible-NIR with a single fibre*.

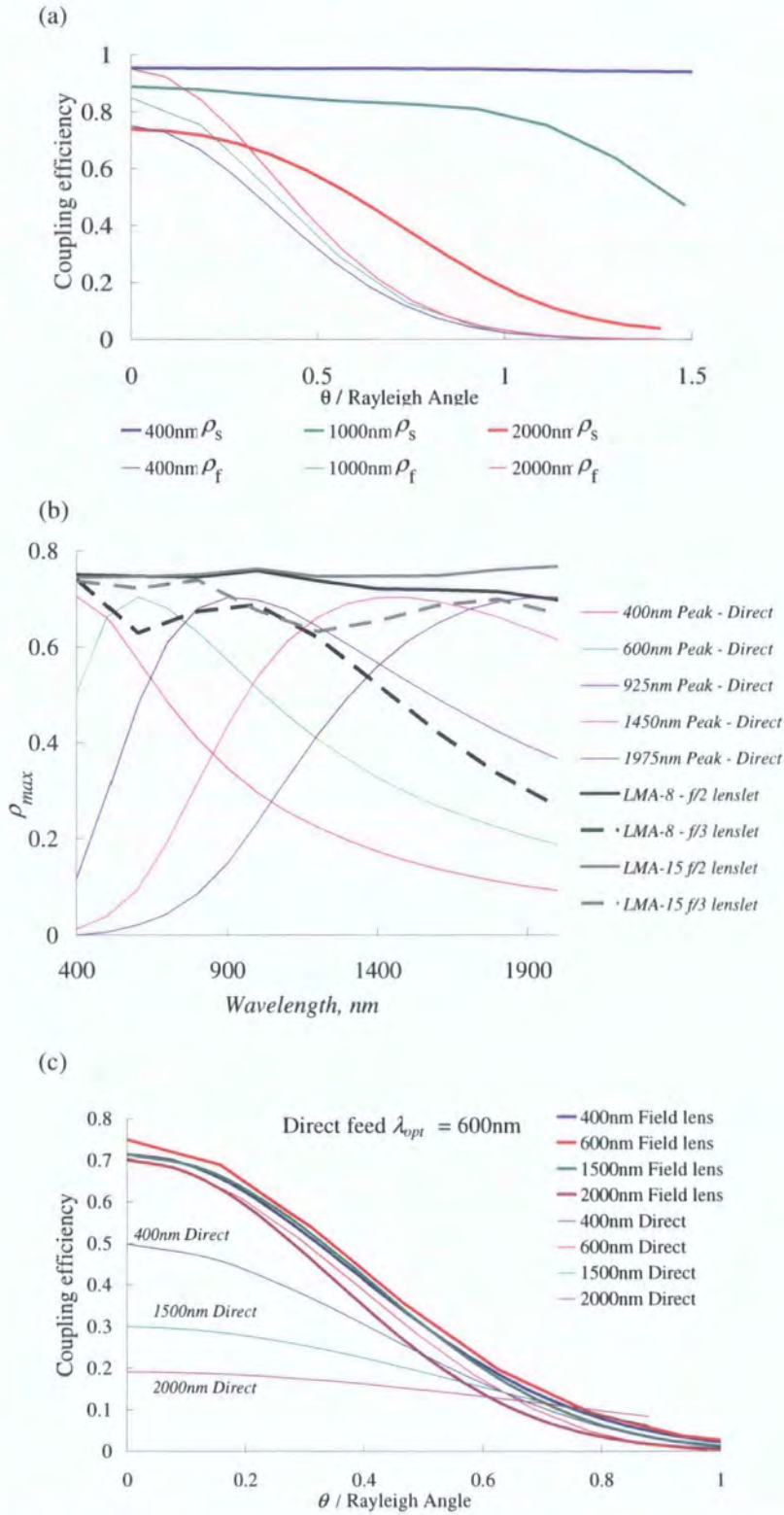


Figure 5.8 (a) A plot of  $\rho_f$  and  $\rho_s$  for  $F_L = 2$  and an LMA-8 fibre. (b) The spectral response of lenslet and direct feed (on-axis) coupling into an LMA fibre for a 25% obscured pupil (c) Comparison of direct and lenslet feed FOV for  $\rho$  against  $\theta$ . All wavelengths quoted in nm.

Note from Fig 5.8(b), that the  $f/3$  lenslet causes  $\rho_s$  to fall off in the NIR for the LMA-8 but with the slower lenslet having little affect on the LMA-15.

Figure 5.8(c) is a plot of the direct feed FOV optimised for maximum coupling at 600nm and of the case of a lenslet feed as given by Eq. (5.14). The lenslet-fed FOV is constant at the same maximum value of  $\lambda/d_T$  as the direct feed case as shown by the good agreement between the lenslet feed and 600nm direct fed curves. This is also the same FOV as the direct feed into a step index fibre<sup>[4]</sup>.

The reason for the constant FOV of the lenslet feed can be seen in Fig 5.8(a) where  $\rho_s$  becomes more restrictive in angle at higher  $\lambda$ , whereas  $\rho_f$  becomes more restrictive at lower wavelength. These two terms trade off one another in Eq.(5.4) to yield the curves in the Fig 5.8(c).

The FOV of the direct feed increases for higher  $\lambda$  when defined on a relative scale of some fraction of  $\rho_{max}$  but at the significant cost of nearly  $1/4$  of the peak throughput of that associated with the optimum wavelength (600nm in this case) and so the lenslet feed into an LMA fibre makes the entire visible-NIR simultaneously accessible with a both constant FOV and high throughput.

### 5.5 Single-mode fibres in integral field spectroscopy?

Since the LMA fibre can be fed with a field lens then we see immediately that contiguous sampling of the focal plane of the telescope can, for the first time, be achieved with single-mode fibres. Why is this important? Polarisation maintaining (PM) LMA fibres are available with a mode distribution almost identical to the non-PM case thereby, also for the first time, allowing the possibility of polarisation maintaining integral field spectroscopy. Further, a small bundle of single mode fibres fed with a contiguous lenslet array thence reformatted into a slit would provide 100% image scrambling<sup>[5]</sup> and no modal noise – Chapter 7. This is possibly an extremely important step forward in very high (spectral) resolution spectroscopy and this is covered in more detail in Chapter 7.

Further to this single-mode fibres are likely to play an important part in feeding light from the telescope to the proposed<sup>[6]</sup> photonic instrumentation. Chapter 1. However,

significant challenges are associated with the contiguously (single-mode) sampled field, some of which are introduced in the next sections.

### 5.5.1 Telecentric requirement

Before dealing with specific examples, some explanation of how arrays of single-mode fibres can be expected to behave on telescope. The field of view of each lenslet in a contiguous array is shown for telecentric and non-telecentric cases in Fig 5.9.

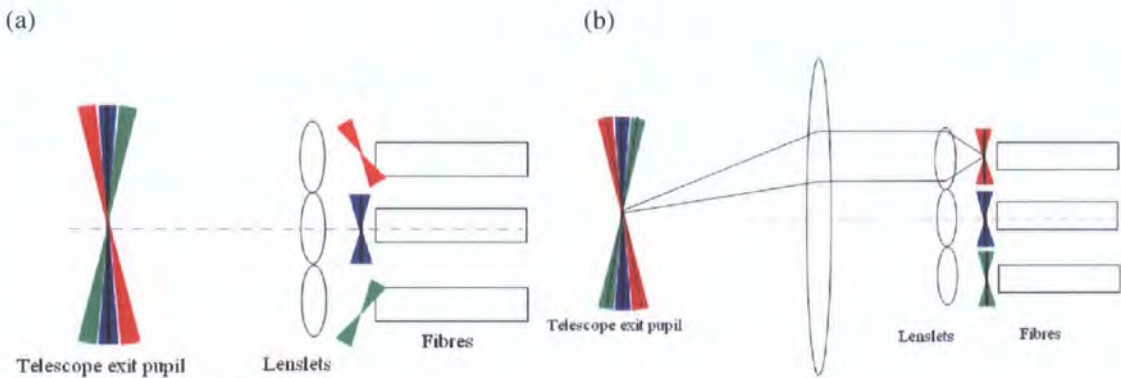


Figure 5.9 – (a) Fibres fed in a non-telecentric mode, (b) Fibres fed telecentrically.

From Eq. (5.5) the coupling falls off significantly with increasing angle. Fig 5.9 then shows the need for telecentric foreoptics is of paramount importance when sampling extended fields using single-mode fibres, since the coupling of off axis lenslets gets progressively worse with off axis distance in the non-telecentric case. The field tilts shown are directly related to the speed of the input focal cone at each fibre so that for far enough off-axis, the numerical aperture of the fibre is exceeded. The pupil image is also progressively de-centred from the fibre further and further off-axis.

### 5.5.2 The coupling of multiple lenslets

In this section the coupling efficiency is investigated when the telescope PSF falls on more than one lenslet. Looking at Fig 5.10, the energy in the dotted region couples into fibre A on its axis with efficiency as given by the crossed point on the green coupling efficiency trace for fibre A. However, some of the telescope PSF energy resides over the fibre B lenslet. To fibre B, the PSF appears to be centred, off-axis at angle  $\theta$ . However, by similar triangles,  $\theta$  is also given by the angular separation of B

with respect to A. Therefore the coupling efficiency into fibre B can be found by simply extending the coupling efficiency curve for A over the region covered by fibre B, taking the value on the curve at the axis of fibre B. The cross-hatched region of the PSF thus couples in with efficiency given by the encircled value on the green curve. As the PSF moves off the axis of fibre A the coupling curve moves with it yielding the coupling curves as shown in panels (b) and (c). Therefore when computing the coupling in these cases we need only show the coupling curve out to the centre of the  $n^{\text{th}}$  lenslet of interest, where  $n$  is the number of lenslets required to sample the PSF.

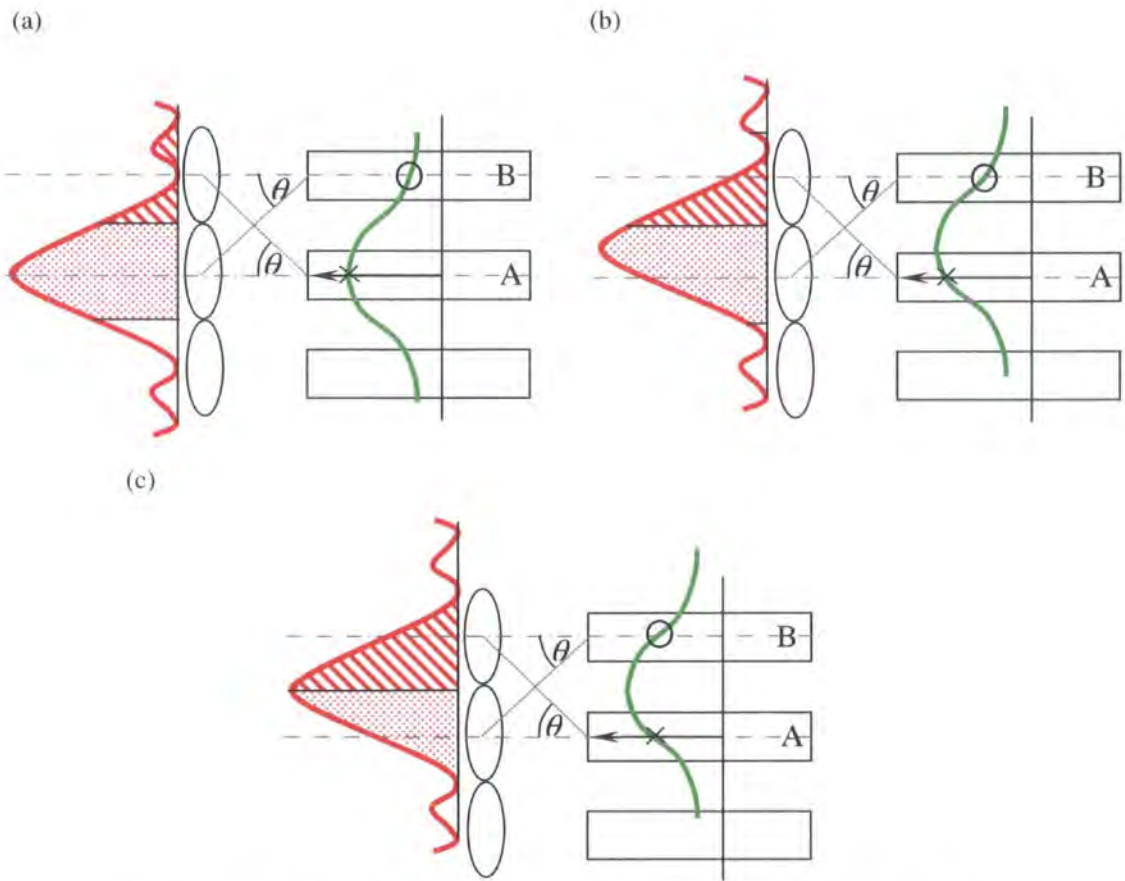


Figure 5.10 – The coupling curve for fibre A can be extended beyond the lenslet boundary to yield the coupling value into fibre B (a) PSF on axis ( $\rho_x \gg \rho_0$ ), (b) PSF moves off axis ( $\rho_x > \rho_0$ ), (c) PSF sampled by lenslets A and B, ( $\rho_x = \rho_0$ )

### 5.5.3 The effect of slower lenslets

As either the wavelength increases or the speed of the lenslet is reduced, the size of the lenslet PSF increases with respect to the geometrical image. Furthermore, as the angle

of the source,  $O$ , changes in the field of view of the fibre, the cosine term in  $P.exp(ikny\theta)$  changes and as can be seen from Fig.5.11 under certain circumstances, the PSF of the lenslet and the cosine term beat with each other causing dark rings to appear in the field of view.

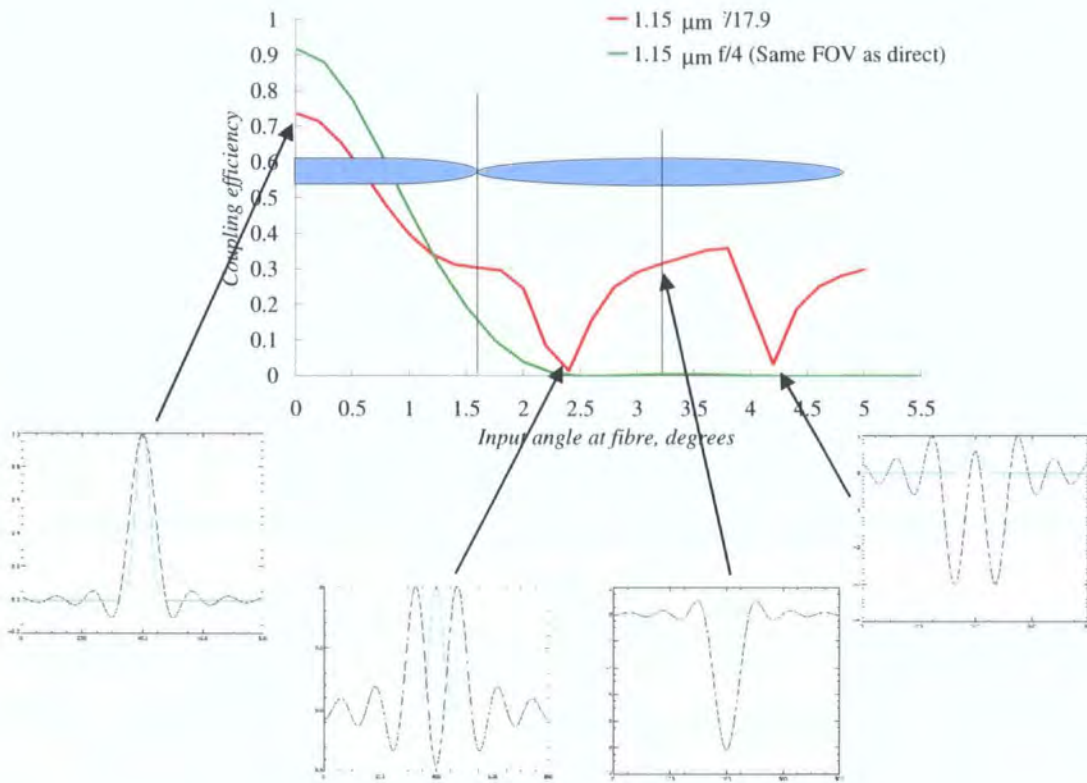


Figure 5.11 – The coupling response of  $f/4$  and  $f/17.9$  lenslets. The  $f/19$  lenslets are shown on the diagram. The wavelength used was  $1.15\mu\text{m}$ . Note the efficient coupling when the image is well confined to the central region around the fibre mode and poor coupling when spread out. The images are normalised in abscissa and on an arbitrary pixel scale in ordinate.

The image appears to be an Airy pattern because it is dominated by the PSF of the lenslet. Notice that regions of high coupling in the figure are associated with the Airy-like appearance of the image, whereas the regions of low coupling occur when the convolution of geometrical image and lenslet PSF yield an increased spread. Note that the geometrical image width is not changing here. The energy within the badly diffracted image is concentrated towards the image centre (with an Airy-like appearance) in regions of high coupling.

The green curve applies to an  $f/4$  lenslet which easily allows the whole PSF through the lenslet aperture (MOS mode), and the red curve,  $f/17.9$ , where the diffraction limited PSF is Nyquist sampled out to the Rayleigh length,  $1.22F_T\lambda$ . Note the greatly increased field of view of the  $f/17.9$  case (albeit with the inclusion of the dark rings) due to the insensitivity of the image to angle when the convolution is dominated by the lenslet PSF.

#### 5.5.4 Single-mode sampling

From the results of the previous sections (5.6.2/3) it seems intuitively correct that more than one single-mode fibre will couple in more light than a single fibre. However, it turns out that this is not always the case. In the diffraction limited case, only a single plane wave component resides in the telescope entrance pupil and thence only a single isolated Airy pattern exists in the telescope image plane. From the results of sections 5.3.1/2 and Chapter 4, in the diffraction limit, the maximum possible coupling into a single fibre is  $\approx 82\%$ . However, in the Nyquist sampled case of Fig 5.10(c), each 42% part of the PSF (1/2 of the energy within the first dark ring in the Airy pattern) will couple in at  $\approx 35\%$  with a total efficiency of  $42\% \times 2 \times 35\% = 29\%$ . The total coupling varies slightly between the three cases in Fig 5.10 but the overall average is  $\approx 35\%$ .

Therefore, *in the diffraction limit, if light collection is all that is required then a single SM fibre is more efficient than a SM array*. However, if imaging is required (e.g. for PM IFS) then the increased field of view is achieved at the cost of throughput. This general comment is necessary because we are in the diffracted regime, where the conservation of etendue, a ray optical result, is not observed.

Figure 5.12 shows what happens as the diffraction PSF is over and under-sampled. The sampling is altered by changing the speed of the lenslet feeding the fibre for a fixed fibre core size.

In the over-sampled case, the overall coupling does not increase due to the reducing coupling value associated with the slower lenslets – Fig 5.17 (a) -. In other words, as the lenslet focal ratio increases so does the width of the lenslet PSF and the overall image width becomes poorly matched to the fibre core.



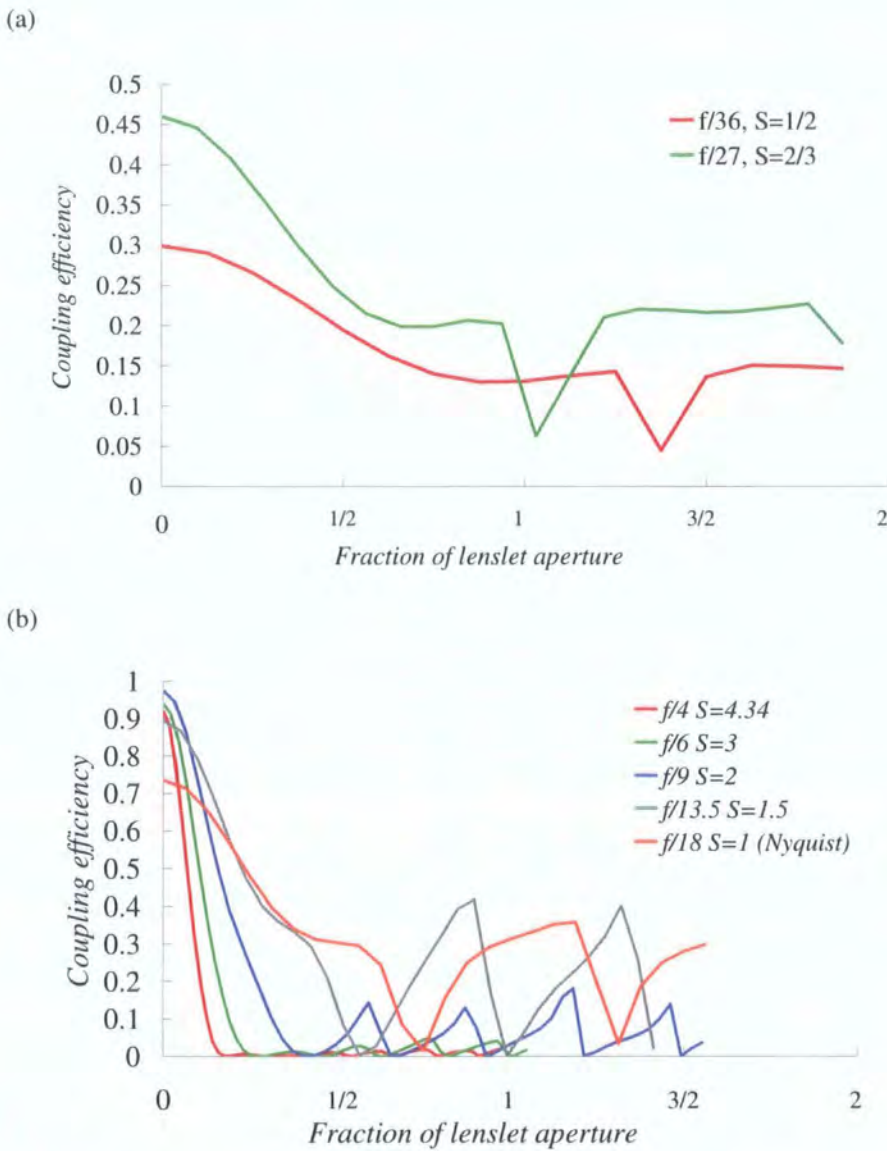


Figure 5.12 (a) Coupling efficiency against illuminated fraction of lenslet aperture for an over-sampled diffraction limited telescope PSF, (b) The under-sampled case,  $\lambda = 1.15\mu\text{m}$ .  $S=1$  indicates the Nyquist sample.

Note that due to Eq.(5.12), and noting that  $d_p=1.33\lambda$ , the curves shown in figures 5.11 and 5.12 are completely general. e.g. the LMA-20,  $\lambda = 1.15\mu\text{m}$ ,  $S=1$ ,  $F_l=18$  curve is identical to the LMA-20,  $\lambda = 800\text{nm}$ ,  $S=1$ ,  $F_l = 25.7$  or LMA-8,  $\lambda = 1.15\mu\text{m}$ ,  $S=1$ ,  $F_l=7.7$ , curves.

In the under-sampled case, the field of view changes as shown in Fig 5.12 (b). The coupling efficiency depends strongly on the position of the telescope PSF with respect

to the lenslets. e.g. in the  $S=4$  case, where the full width of the lenslet is  $1.22F_T\lambda \times 4$ , the maximum coupling, of 92% is on axis but for Airy patterns at other points in the field of view the coupling is zero. The  $S=1$  case is dealt with above but note that the dark rings in the field of view are far less severe than in the  $S=4$  case, with various intermediate cases in between.

In the atmospherically-aberrated case, many plane wave components are populated, with various energies, within the telescope entrance pupil, with the resulting degraded PSF. The SM coupling efficiency of even modestly degraded PSF's is rather poor – Chapter 4 - but the coupling efficiency of each of the diffraction limited PSF's that go to make up the degraded PSF would remain as shown in Fig 5.12. However, it is a major exercise to compare the coupling of aberrated PSF's into arrays of SM fibres with that of the single SM fibre case and this is commented on further in Chapter 8.

## 5.6 *Experimental considerations*

Equation 5.5 lends itself to direct experimental falsification and this is the primary aim of this section. The polishing work undertaken to prepare the LMA-20 fibre tested is described in section 5.6.1. The experimental apparatus and subsequent results are then described in 5.6.2.

### 5.6.1 *Fibre Preparation*

As with any optical fibre used in astronomical instrumentation, high quality preparation of the end face of the fibre is of paramount importance to reduce scattering of the incident light by surface defects. Reduction of end-effect induced FRD and the losses due to scattering of light into radiation modes are two examples for multimode fibres but the problem is particularly acute for single mode fibres since there is only the single supported mode to couple into. Hence, even small amounts of light scattered from defects can severely affect the fibre's transmission since there are no other (transmitted) modes to scatter into.

End face preparation of optical fibre typically involves first cleaving the fibre and then polishing. There are various cleaving techniques the most common of which are score and break, whereby the fibre's outer (cylindrical) surface is scored and then the fibre placed under tension until it snaps at the defect and the ultrasonic blade technique, whereby the fibre is held firmly either side of an ultrasonically vibrated blade. Whilst the cleaving technique yields a high surface quality, for high throughput applications such as astronomy and telecommunications further end preparation is required.

Polishing, is an abrasive process that works to reduce the characteristic length of the surface defects left by cleaving to much less than the smallest wavelength of the coupled radiation intended for the fibre. The polishing process is often automated but for this work both the step index and LMA fibres were polished, by hand, using the puck and figure-of-eight technique with various grades of polishing paper and finishing with a final polish using colloidal silica.

This technique involves securing the fibre inside a hypodermic needle which is then held within a puck. The tip of the fibre protrudes by a very small distance from the hypodermic and is therefore in contact with the paper. The puck is moved over the abrasive paper and the fibre polished with papers of progressively smaller grit size.

Polishing of the step index fibre was routine but the LMA cross section consists of a regular hexagonal array of holes that form the photonic crystal structure. Liu *et al* comment<sup>[1]</sup> that holey fibres need to be collapsed whilst polishing in order that the holes do not fill up with spoil from the process. Panels (a) and (b) of Fig 5.13 are an example of this. However, in the interests of finding a low cost option it was found that a short period of immersion in ultra-sonicated water will clear most of the filled holes after hand polishing with only minimal damage to the hole profile at the surface – Fig 5.13(c) shows this clearly by comparison to panel (b);

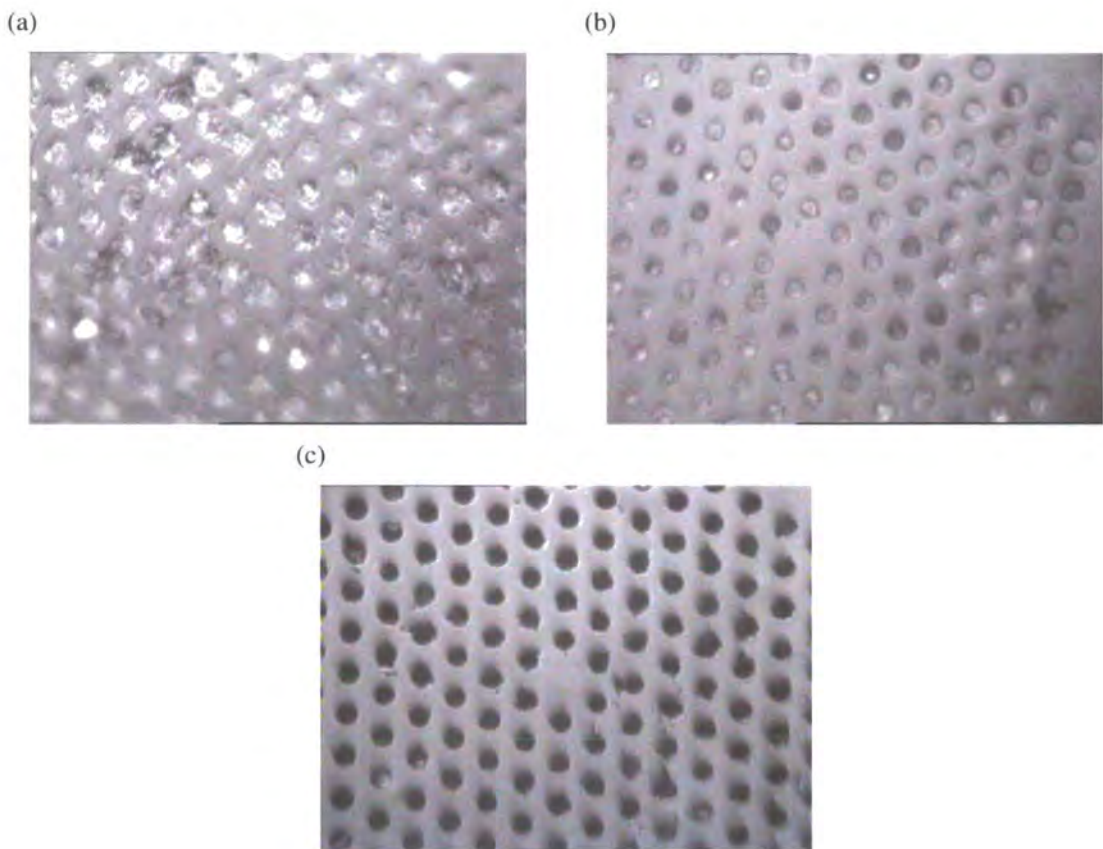


*Figure 5.13 - Various images of the end face of the LMA fibre (a) After polishing with 300nm grit polishing paper (b) After polishing with colloidal silica (c) After short period of ultrasound showing some light damage to holes but with nearly all holes free from debris.*

The immersion time was two to three seconds in the centre of the ultrasonic bath. Any more than this, removed the spoil from the holes, but also damaged the fibre structure. The above results were recorded with ultra-sonication after polishing (with various

grades of paper) was complete. An improvement to the process may be to gently ultrasound the fibre end between each successive grit size to try to reduce the amount of damage done whilst still removing the spoil. The LMA fibre tested was polished to the same standard as panel (c) with results in good agreement with manufacturers spec for numerical aperture and expected far and near field spatial profile and thus this finessing was not attempted due to time constraints.

Despite the high general surface quality due to polishing, occasionally a small piece of debris can get caught in the active polishing area and score or pit the surface. These defects can be significant enough to require a complete re-polish or even a new cleave/repolish which can be extremely time consuming for multiple fibre systems. However, small defects in the surface of the end face of a fibre can often be made invisible to the incoming light by index matching them out with an appropriate grease, with RI matching that of the fibre core. Spread between the core and a glass plate (itself of the same RI) the glass plate now acts as a high quality optical end face of the fibre. This is a standard technique that can lead to significant time savings in fibre preparation since minor surface defects can be left without the further polishing required to remove them.

However, when used on the LMA fibre photonic crystal fibre, it was, perhaps not surprisingly, found that the index matching grease can find its way into the holey, photonic structure with significant effects on the measured far-field pattern. A large variation in output from one application of the grease to another was observed, with some quite pronounced differences in the far-field.

Taking  $z = 0.0$  at the fibre output end face, Fig 5.14 panels (a) and (b) show the far-field outputs at axial distances  $z = 2.5\text{mm}$  and  $z = 8\text{mm}$  far-field, respectively, of the LMA fibre with no index matching grease or glass plate. The shape of the field is as expected<sup>[2]</sup>, a central Gaussian with the six satellite lobes visible on panel (a) but invisible on panel (b) on the linear scale of these pictures. (Note that the lobes do not disappear at large  $z$ , however, the ability to detect them against a non-zero background and CCD dark count does diminish as their peak value decreases as  $1/z^2$ ).

Panels (c), (d) & (e) show the  $z = 8\text{mm}$  far-field patterns for three separate experiments where the index matching grease and glass plate were applied. Panel (e) highlights the fact that it is possible to use the grease and get relatively unperturbed results (compare with panel (b)), however panel (c) has a very different spatial

distribution with much more energy encoded in the satellite spots (with peak values of ~30% of the peak value of the central Gaussian). Panel (d) shows an intermediate result with a non-radially symmetric distribution.

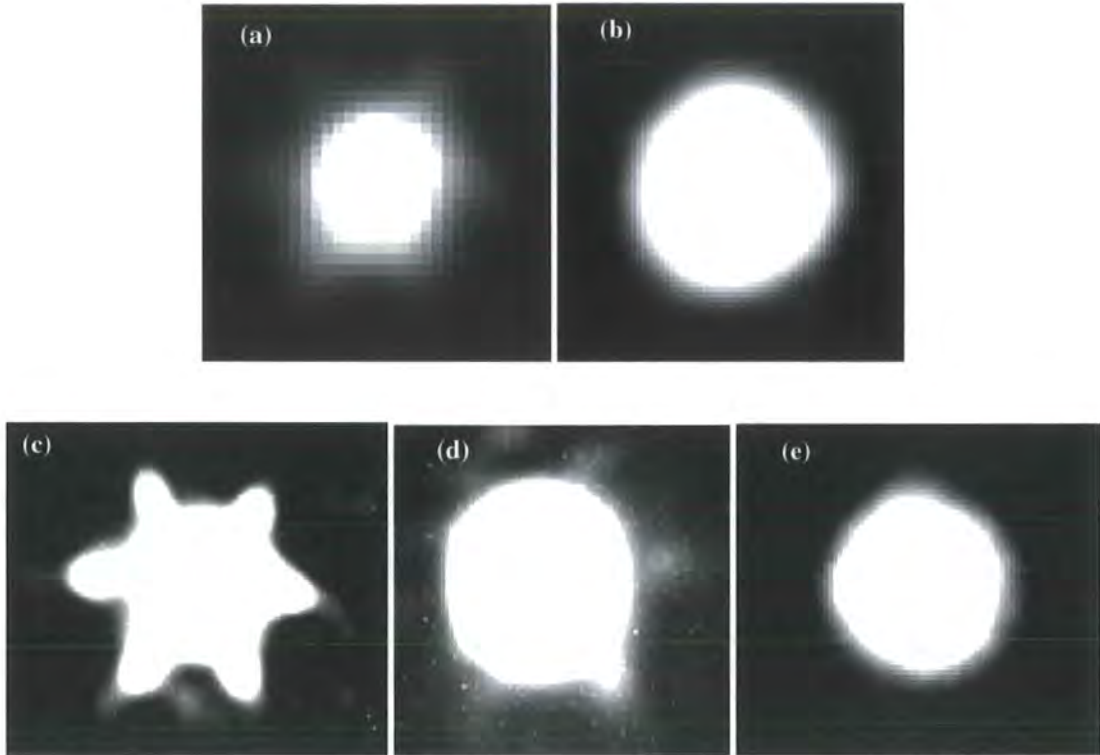


Figure 5-14 – (a) The  $z = 2.5\text{mm}$  distance far-field pattern of the LMA fibre with no index matching grease or glass plate – the six expected<sup>[2]</sup> satellite lobes are just visible (b) the  $z = 8.0\text{mm}$  distance far-field pattern of the LMA fibre with no index matching grease or glass plate – (c), (d) & (e) examples of the 8mm far-field pattern with index matching grease and glass plate applied to the output end face of the fibre. All images at linear intensity scale but not same spatial scale.

This work does not undertake a detailed theoretical analysis of these results. However, Mortenson *et al* <sup>[3]</sup>, have modelled the near field distribution of the single supported fibre mode as a central Gaussian from which six smaller (width and magnitude) Gaussians, centred on the inner ring of holes, are subtracted. The subsequent far-field matches the observed Physics well and is a consequence of the interference between these different Gaussian elements as the total field propagates. It is not difficult to imagine then that holes that are filled or part filled and cause significant changes to the

modal field distribution at the fibre end face might have significant effects in the far-field.

With so much variation measured in the far-field output and no way of controlling how many holes are filled, part filled and to what depth, the best advice for hand-polished fibres seems to be to polish to a standard high enough not to require the index matching technique or in the case where a lenslet needs to be bonded to the fibre end face, to buy the fibres hermetically sealed (not tested).

### 5.6.2 *Experimental investigation of the LMA fibre.*

The apparatus constructed to verify Eq. (5.5) is shown in Fig 5.15. A 100 $\mu\text{m}$  diameter 'telescope' with 'lenslet' was used to feed the fibre as shown in the schematic Fig 5.15. The source of illumination is described below and was incident from the left. The whole telescope mount was pivoted directly below the telescope pupil so the input angle could be adjusted using the micrometer shown.

Some uncertainty in the centre of rotation of the stage with respect to the telescope must exist and so the image of the telescope pupil was placed directly on the CCD and the intensity as a function of tilt angle measured. Also the experiment was conducted at a range of angles either side of the measured angle of maximum coupling in order to experimentally locate the zero angle point. The variation in intensity was found to vary by no more than 2% across the range of angles tested and is subsumed into the uncertainty in the abscissa along with 5 times reproduced throughput values. Hence the abscissa error depends on estimates of both the *repeatability*, describing effects such as output power variation in the light source and the photon noise of the detector, and the *reproducibility*, describing the apparatus ability to reproduce the same experimental results, such as micro shifts in the pivot position for example.

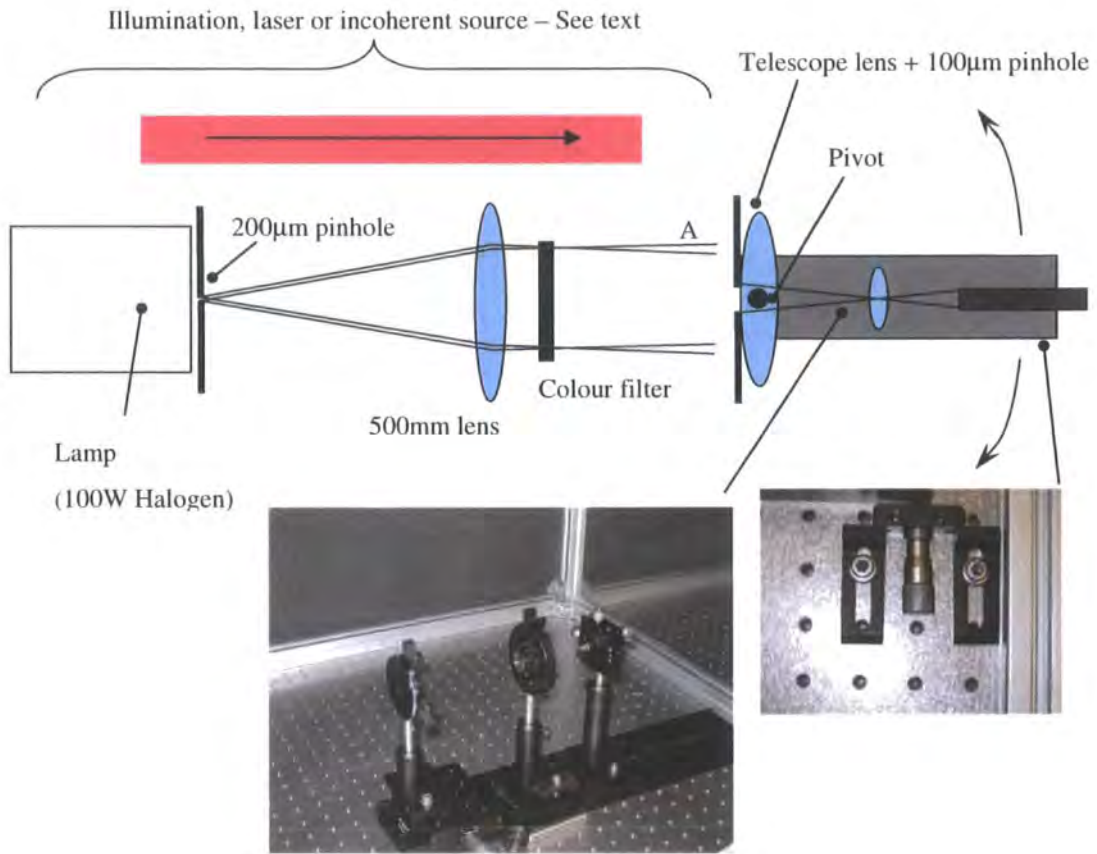


Figure 5.15 - Schematic of the test apparatus

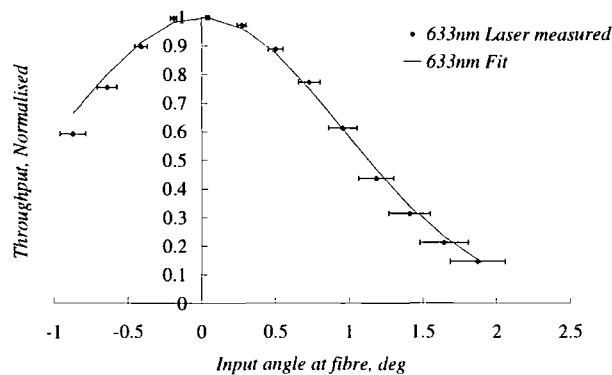
The conservation of etendue between telescope and image at the fibre end face yield an angular ratio between them of 5.7 and an estimated uncertainty of  $\pm 10\%$  is applied to this to allow for variation in the optics. The uncertainty in the ordinate is then given by the sum in quadrature of this term and the angular uncertainty associated with the micrometer precision and the uncertainty in the distance between the micrometer and the pivot.

The experiment was done in two parts, the first using lasers to illuminate the telescope, the second an incoherent system designed to approximate a small range of input plane waves.

In the first instance, the telescope was illuminated with a 4mW, 633nm, HeNe laser. The beam was expanded to a Gaussian half width of approximately 15mm yielding an excellent approximation to a plane wave over the central 100µm of the beam. A range

of input angles at the telescope aperture were set and the output recorded by placing the entire output far-field of the LMA-20 used throughout the test directly onto the CCD of the Q-imaging Retiga EX, also used throughout. The variation in throughput as a function of angle and the associated value according to Eq 5.5 are both plotted in Fig 5.16(a), with a repeat experiment, using a 532nm diode laser but nonetheless subject to a similar beam quality over the 100 $\mu$ m pinhole, plotted in panel (b).

(a)



(b)

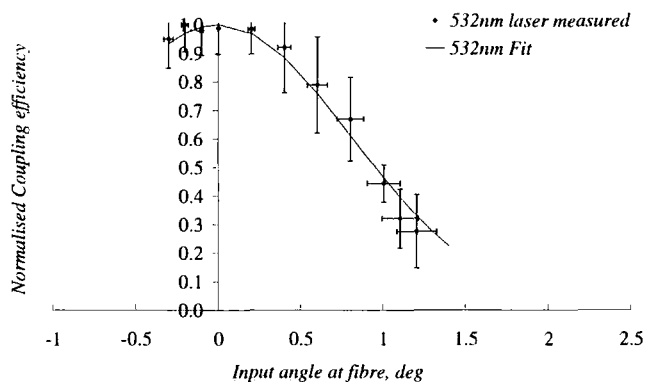


Figure 5. 16 - (a), 633nm laser illumination, (b) 532nm laser illumination

The small uncertainty in the abscissa in the 633nm case was due to the excellent stability of the laser and apparatus reproducibility in angle. The rather larger uncertainty in the 532nm case is due to the fact that this wavelength resides on a very steep bend loss edge in the attenuation spectrum of the LMA-20 fibre, see Fig 3.9, for example. Even micro-movements of the fibre, due to say, the air conditioning in the

room, have a significant effect. It proved extremely difficult to reduce this effect to an insignificant level and the large error bars on panel (b) reflect this.

In order to confirm, further, the form of Eq. (5.5), a 905nm laser filter was purchased, somewhat more cheaply than a 905nm laser. Hence, a white light source, feeding the filter was setup to feed to the telescope as shown in Fig 5.15.

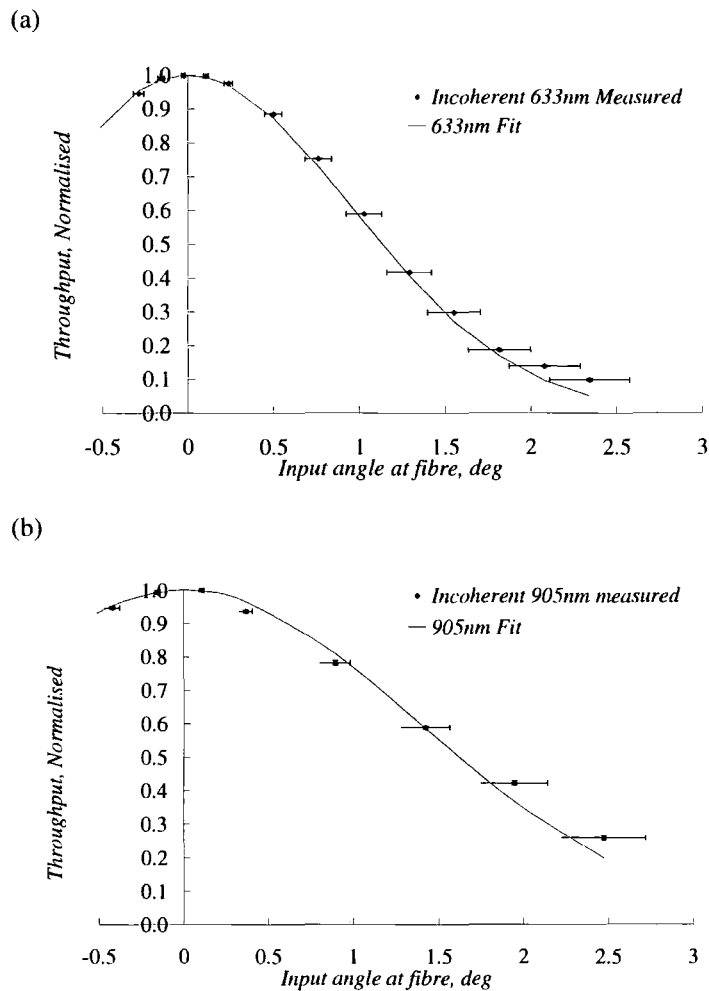


Figure 5.17 (a) 633nm incoherent illumination, (b) 905nm incoherent illumination.

The apparatus was set up using a 633nm laser line filter and the pinhole reduced in size until the angular range at A was enough for the incoherent 633nm data to match the data recorded using the 633nm laser and of course, the fit according to Eq. (5.5).

The single-sided angular range at point A in the diagram is  $100\mu\text{m}/500\text{mm} \sim 0.043^\circ$  at the fibre.. This is shown in Fig.5.17(a). Once this was achieved, the 633nm filter was replaced with the 905nm filter and the data in Fig.5.17(b) were recorded.

To summarise, Eq. (5.5) has been tested experimentally over a 373nm bandwidth over the mid to upper VIS and lower NIR and found to be in good agreement with the data. This experiment also lends further support to the validity of the coupling integral, at least at low angles.

The absolute throughput of the 905nm and 633nm incoherent data were compared and differed in value by less than 3%. This is well in line with the maximised coupling across the range for the lenslet feed. However, it is possible for two wavelengths separated by only 272nm to yield roughly the same coupling value – see the direct feed curves in Fig 5.8(b) for instance and so whilst encouraging, this results does not prove the model. However constraints on both budget and time prevented further work in this area. This is commented upon further in chapter 8.

## 5.7 Summary

The LMA fibre is characterised by a large mode field that can be taken as constant in size and distribution with wavelength in this application allowing high efficiency coupling of starlight over a much broader wavelength range using a lenslet than the direct feed case.

Step index fibres, with their wavelength dependent mode field, can be used to flatten the direct feed response over an octave or so – Chapter 4, but generally have severely limited attenuation spectrum by contrast to the LMA case. The maximum field of view of the lenslet fed LMA fibre has been shown to be approximately the same as the direct feed step index and LMA fibre cases.

The lenslet feed scheme now allows, for the first time, single-mode integral field spectroscopy with single-mode fibres. However, single-mode fibres behave very differently to multimode fibres and some of these differences have been discussed. Significantly it is more efficient to couple light into a single SM fibre, than into an array when Nyquist sampling in the diffraction limit.

Finally Eq.(5.5) was experimentally verified in the range 532nm to 905nm and out <3 degrees of tilt in the wavefront. This also validates the coupling integral out to these angles and when applied to photonic crystal fibres.

## 5.8 References

- 1) 'Introduction to Fourier Optics' JW Goodman McGraw-Hill (1996)
- 2) 'Design and fabrication of a coherent array of single-mode optical fibres for the nulling coronagraph'. D Liu, B Levine & M Shao. Proc. SPIE 5170 Techniques and Instrumentation for detection of exoplanets. (2003)
- 3) Near-field to far-field transition of photonic crystal fibres: symmetries and interference phenomena'. N Mortensen and J Folkenberg. Opt. Express **10**, No 11 (2002). <http://www.opticsexpress.org/abstract.cfm?URI=OPEX-10-11-475>
- 4) 'Wide-field interferometric imaging with single-mode fibres'. Olivier Guyon. A&A **387**, 366-378 (2002)
- 5) TR Hunter and LW Ramsey, "Scrambling properties of optical fibres and the performance of a double scrambler," PASP 104, pp. 1244-1251, 1992
- 6) J Bland-Hawthorn, A Horton, 'Instruments without optics: an integrated photonic spectrograph', SPIE (2006), *in press*

# Chapter 6

## *Multimode fibres to single-mode arrays*

### 6.1 Introduction

OH-suppressing fibres have recently been reported<sup>[1,2]</sup> that convert a multi-mode fibre (MMF) into an array of single-mode (SM) fibres on which can be imprinted fibre Bragg gratings. The single mode array (SMA) is then re-fused into a MMF yielding a multi-moded fibre device capable of suppressing certain wavelengths such as the atmospheric OH lines with single-mode performance. Fig. 6.1. Analysis of these fibres provides useful information for the fibre manufacturers and instruments scientists alike and yields another example of the importance of the ray and EM models of optical fibres in astronomy.

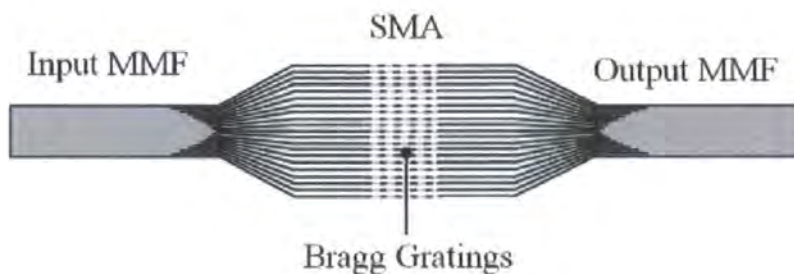


*Figure 6.1 - The input MMF transforms into the SMA array on which the Bragg gratings are encoded. The reverse transition then reforms the SMA into the output MMF*

Despite the demonstration of a 19 mode device<sup>[1]</sup>, manufacture of these devices with 100's rather than 10's of modes in the SMA is currently very challenging and is likely to remain so in the near term. Therefore we again appeal to the ideas laid down in Section 2.4 in order to determine the distribution of power within the input multimode step index fibre (MMF) when used to transport starlight in an astronomical instrument when fed (a) by the telescope point spread function (PSF) and (b) when fed with an image of the telescope exit pupil via a lenslet in the telescope image plane. This model is then used to predict how many modes are required in order to remain useful to astronomy.

The fibre model itself is presented in section 6.2 with the direct and lenslet fed cases dealt with in section 6.3 and 6.4, respectively.

## 6.2 *The fibre model*

### 6.2.1 *From the MMF to the SMA*

The single mode array made from  $M$  single-mode cores can support  $M$  modes<sup>[1]</sup> which under the assumption of a strictly adiabatic transition, are transposed into the array from the fibre in order of increasing  $U$  within the MMF. e.g. looking at Fig 2(a) in order of  $HE_{11}$ ,  $TE_{01}$ ,  $HE_{21}$  (Odd + Even),  $TM_{01}$ ,  $EH_{11}$  (Odd + Even),  $HE_{31}$  (Odd + Even),  $HE_{12}$ , etc... at  $V > 4.2$  However, the  $U(V)$  curves can sometimes be seen to cross near the cut-off region, e.g. near  $U=V$  in Fig.6.2(b) - and so it is not strictly possible to assume, using the weakly guiding model, that an SMA supporting  $M$  modes will couple the lowest  $M$  modes of the MMF. However, at any given value of  $V$  only approximately 8 per cent of the supported modes are near cut-off<sup>[3]</sup> and hence it is safe to assume sequential transfer of modal indices with an uncertainty of <8 per cent or so when the number of supported or populated modes is greater than  $M$ , which does not affect the efficacy of this analysis.

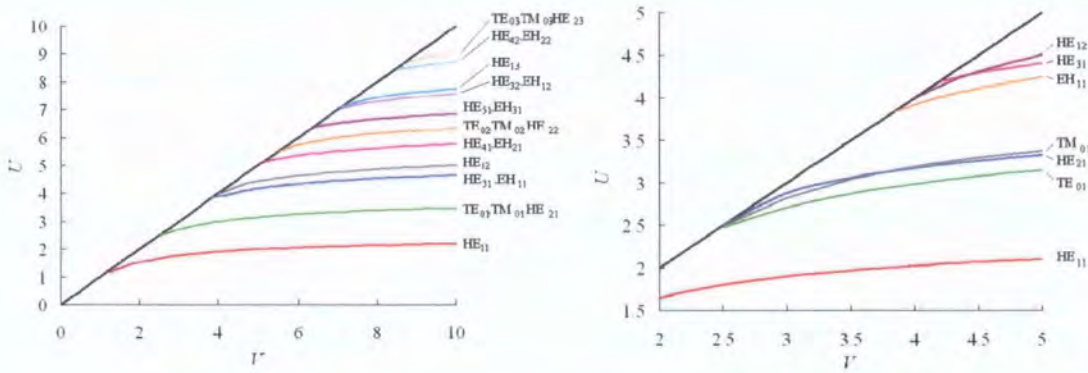


Figure 6.2 – Modal parameter spaces for (a) weakly guiding, (b) strongly guiding circular fibres. Panel (a) reproduced from section 2.3.3

6.2.2 The geometrical, ray optical, model

Borrowing from Chapter 2, it was stated that for  $U \gg 1$  each value of  $U$  can be associated with a unique characteristic ray angle,  $\theta$ ,

$$U = \frac{2\pi n_{core} \sin \theta}{\lambda} = V \frac{\sin \theta}{\sin \Theta} \tag{6.1}$$

azimuthal with respect to the fibre axis and hence  $\theta \in [0, \Theta]$ . The commonly used formula for the number of supported (bound) MMF modes,  $N$  for a given  $\theta_{max}$ , is also based on the  $U_{max} \gg 1$  approximation<sup>[4]</sup> and is given by,

$$N = \frac{U_{max}^2}{n} \tag{6.2}$$

where  $n$  is an integer who's value depends on how the modes of the fibre are counted and  $U_{max}$  is the highest populated  $U$  within the fibre, by the illumination. The number of modes within the fibre is constant of course but there is more than one way to classify a ‘mode’ and  $n$  is determined in the following manner.

For instance, Eq.6.2 applies to the fully vectorial mode designation when  $n=2$ . The linearly polarized, *LP*, modes of the fibre are the sum of all four vectorial fields at

each  $l, m$  to yield the  $LP_{l-1, m}$  modes and so the number of  $LP$  modes is reduced to  $N=U_{max}^2/8$ . Inspecting Fig 6.2(a) we see that in the  $l = 0$  and  $l = 1$  cases one and three vectorial mode(s), respectively, are approximately associated with a single  $\theta$  but for all  $l > 1$ , there are two vectorial modes per  $\theta$  and the number of modes in the input optical fibre, is well approximated by  $N = U_{max}^2/4$ . Since this is how the modes of the feeding MMF are transferred into the SMA then the  $n = 4$  case also applies to the SMA. – i.e. the SMA must be made from at least  $n = 4$  cores to support all of the modes in the MMF.

Looking at Fig.6.2(a), we see that at the cutoff  $U_{cutoff} \approx V$  for any  $V$  and thence replacing  $U_{cutoff}$  with  $V$  in Eq.6.2 yields the total supported (bound) modes within the numerical aperture of the fibre. Further, since we start with the electromagnetic field model and seek correspondence with the geometrical ray model, at  $U_{cutoff}$ ,  $\theta_{cutoff} \approx \Theta$  and the maximum supported angle within the fibre is very nearly the numerical aperture itself. The fractional error associated with Eq's.6.1 & 6.2 is  $1/U$  [4,5].

### 6.2.3 The general effect of $M < N$

In this subsection we investigate, in general terms, the effect of there being fewer supported modes within the SMA than are supported within the input MMF.

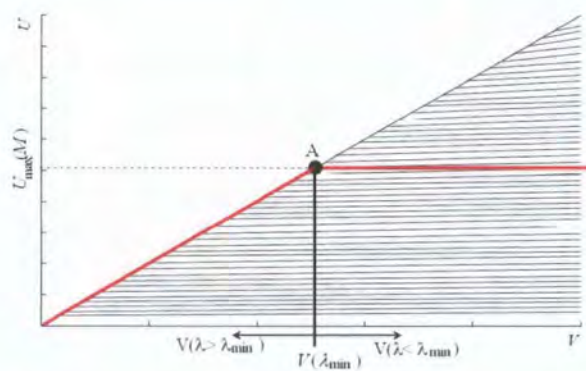


Figure 6.3 – Schematic plot of the MMF  $U(V)$  showing  $U_{max}$  associated with the  $M$  modes supported within the SMA.

For a given fibre,  $a$  and  $\Theta$ , the  $V$  parameter scales inversely with wavelength, Eq.2.7. At point A in Fig 6.3  $V = U_{max} = U_{cutoff}$  and from Eq.6.1  $\theta_{cutoff} = \Theta$ . At all  $\lambda > \lambda_{min}$  the

line  $V = U_{cutoff}$  is accessible and so therefore is the numerical aperture of the fibre. However, for all  $\lambda < \lambda_{min}$  the maximum value of  $U$  transmitted by the SMA remains as  $U_{max}$  but  $V$  still scales inversely with  $\lambda$  and again by Eq.6.1 then  $\theta_{max}$  also becomes inversely proportional to  $\lambda$ . In other words the numerical aperture of the fibre becomes wavelength dependent. The on-sky consequences of this effect are discussed in sections 6.3 and 6.4.

### 6.2.4 The coupling calculations

In the EM case the coupling integral, Eq.2.29 was used with Eq.4.1 in the Airy feed case and Eq.5.3 in the lenslet fed case. Both cases are assumed to have circular aperture only.

As in previous chapters, a  $1000^2$  grid was used where appropriate, however, some of the higher order modes required larger matrices in order to adequately sample the fine structure of some higher modes near to the fibre axis. Note that all coupling integral results match their physical analogues well even at the highest mode orders, e.g. Fig 6.10, showing the effectiveness of this approach.

## 6.3 Airy pattern coupling

### 6.3.1 Ideal seeing

In this section we compare the predictions of the ray geometrical and the electromagnetic coupling models. Fig 6.4

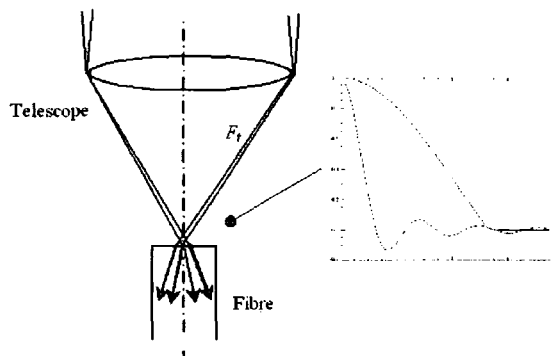


Figure 6.4 - The geometrical ray model and inset the Airy pattern  $\text{Re}(E_{xg})$  and fibre fundamental mode for the case of  $(w/a)=0.3$ , where  $w$  is given by Eq.(6.3) and  $a$  is the fibre core radius.

We first re-define the  $V$  parameter in terms of the Rayleigh length,  $w$ , of the unaberrated telescope PSF which in the scalar optical approximation is given by,

$$w = 1.22 F_T \lambda \quad (6.3)$$

where  $F_T$  is the telescope focal ratio. Re-arranging and substituting into Eq 2.7 yields,

$$V = \frac{2.44\pi\Theta F_T}{\left(\frac{w}{a}\right)} \quad (6.4)$$

which describes the fibre and telescope together. However, Eq. 2.7 is a special case of Eq. 6.1 and since  $\theta = 1/2F_T$  then,

$$U_{F_T} = \frac{1.22\pi}{\left(\frac{w}{a}\right)} \quad (6.5)$$

where  $U_{F_T}$  describes the part of the  $U(V)$  space occupied by  $F_T$  from the telescope.

Figs 6(a)–(c) are the MPDs of an Airy pattern coupling into the fibre when the PSF is the on-the-fibre axis, 20 per cent (of the fibre core radius) off-axis and 60 per cent off-axis. The ordinate is expressed as SMA mode number, where 1 = HE<sub>11</sub>, 2 = TE<sub>01</sub>, 3 = HE<sub>21</sub>, 4 = TM<sub>01</sub>.....

With the coupling into an individual mode,  $\rho_i$  given by Eq. (2.29), the total guided power,  $\rho_{Total}$  within a fibre supporting  $N$  modes, due to an illuminating field  $E_i$ , is given by  $\rho_{Total} = \sum_{i=1}^N \rho_i$ . For  $U_{max} \gg 1$  the modes of the MMF asymptotically approach a set of plane waves of discrete angular spectrum<sup>[5]</sup> and so the sum should be recognized as yielding the magnitudes of a Fourier-like series decomposition of  $E_i$ , but in the basis of the modes of the fibre. As we shall see, this likeness has a significant impact on the MPDs for various  $E_i$ .

The Fourier transform of an Airy pattern is a top hat so the form of the MPD's should not be surprising. As the Airy pattern moves off-axis the Fourier transform would include a modulating cosine term so that the MPD puts more power into modes within the top hat envelope as the offset from the fibre axis increases.

Again appealing to the Fourier series analogy and focusing only on the numerical value of  $(w/a)$ , as this quantity decreases, smaller spatial frequencies in the image field  $E_i$  appear which require higher order modes within the fibre to couple into, as can be seen from Eq. 6.5. Fig. 6.5(d) shows that indeed this is the case. Note the linear population of the cumulative curve as appropriate to a top hat 'modal transform'. The number of modes required to couple the light in efficiently is given, from Fig. 6.5(d), by the fit  $M_{min} = 4.0881(w/a)^{-1.9698}$  and substituting this into Eq.(6.5) yields

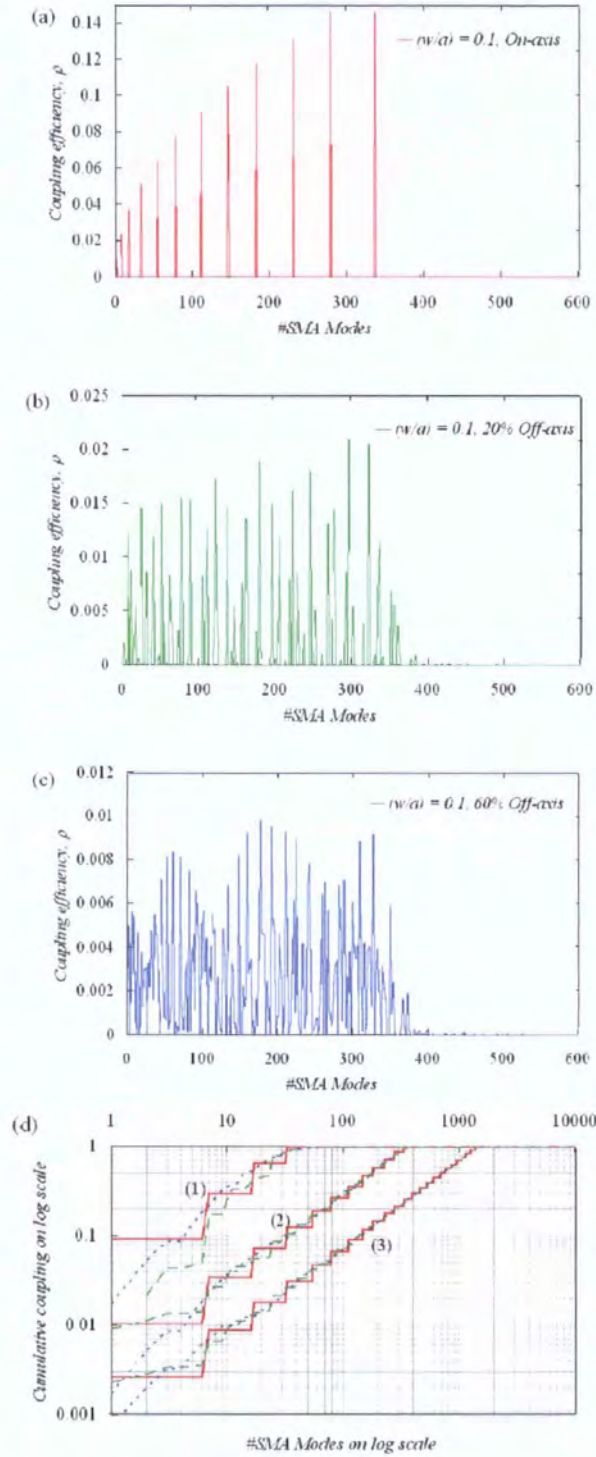


Figure 6.5 - (a)-(c) The MPD of the three cases of on-axis and 20 per cent and 60 per cent off axis, respectively (d) The minimum number of modes required to couple an un-aberrated Airy pattern into the fibre on a log-log scale. (1)  $(w/a)=0.3$ , (2)  $(w/a)=0.1$ , (3)  $(w/a)=0.05$ . Notice that the width of the distribution is a function of  $(w/a)$  only - (solid line)-On axis, (dashed line)-20 per cent off axis, (dotted line) - 60 per cent off axis

$$M_{min} \approx \frac{U_{F_T}^2}{4} \quad (6.6)$$

which shows that the electromagnetic and geometrical coupling models agree well, certainly to within  $1/U$ .

The case  $(w/a) > 0.3$  is not considered because of the increasing loss associated with the vignetting of the PSF by the fibre core. At  $(w/a) = 0.3$  the loss is 4 per cent on-axis, although this is much higher in the aberrated case of course - see below. In the aberrated case we would be more likely to derive some width estimate based on the FWHM of the aberrated PSF, also, in a *real* application, in order to avoid recording significant background. However, in the unaberrated, background-less analysis,  $(w/a)_{max} = 0.3$  and then from Eq.(6.5),  ***$V \approx 13$  is then the minimum value of the  $V$  parameter for effectively lossless coupling of an on-axis Airy pattern into multimode fibres.*** Further, the maximum fractional offset of the centre of the incident PSF in Fig 6.6 is 60 per cent of the fibre core radius since the coupling efficiency starts to fall off significantly beyond this point for  $(w/a) = 0.3$ .

### 6.3.2 $M$ , transmission and field of view

What are Eq.'s (6.5, 6.6) actually telling us about how many modes must be supported within the SMA for lossless overall transmission? From Eq.(6.4),

$$\lambda = \left( \frac{(w/a)}{1.22} \right) \left( \frac{a}{F_T} \right) \quad (6.7)$$

Since the number of modes in the SMA,  $M$ , will be limited by manufacturability, I plot the straight lines of  $\lambda$  against  $(a/F_T)$  for various  $(w/a) = 2/\sqrt{M}$ , in Fig.6.6, up to the limit of  $(w/a) = 0.3 \Rightarrow M = 45$

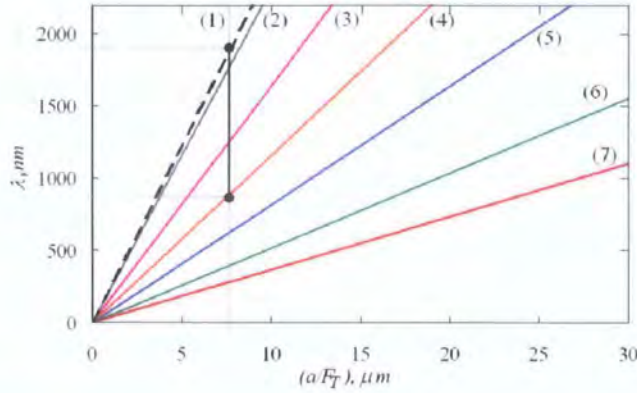


Figure 6.6 - A plot of the accessible wavelength range for the number of modes supported within the SMA and  $(a/F_T)$ . (1)  $M=45$ , (2)  $M=50$ , (3)  $M=100$ , (4)  $M=200$ , (5)  $M=400$ , (6)  $M=1000$ , (7)  $M=2000$ .

The graph shows that simultaneous access the entire 800nm-1800nm range typically associated with OH line emissions, a minimum of 200 modes is required. If the shortest desired wavelength,  $\lambda_{min}$  (with respect to the upper desired wavelength, in this case 1800nm) can be increased, then the number of modes required is also reduced as described by Eq.(6.7). Notice, from Fig 6.6, that an all purpose astronomical fibre capable of transmitting between 365nm and 2 $\mu$ m with full -OH suppression would require about 2000 modes in the SMA array.

In the specific cases of *J* and *H* band coupling, the ratio  $(a/F_T)$  would be selected to accommodate the higher wavelength at  $(w/a) = 0.3$  (the  $M = 45$  dotted line on Fig 6.6), 1.33 $\mu$ m for *J* and 1.78 $\mu$ m for *H*, and then the number of modes needed to couple the lower end of the waveband computed, also using Eq. 6.7, resulting in  $M_{1.15\mu m} = 57$  modes and  $M_{1.49\mu m} = 66$ .

Since Leon-Saval *et al* demonstrated a 19 SMA mode fibre array device<sup>[1]</sup> then if the 200 supported modes from the above example were taken as a reasonable extrapolation in the near to mid term and made into a fibre this would mean  $(a/F_T) \approx 7\mu$ m and for  $F_T = 8$  then  $a=55\mu$ m, or a 110 $\mu$ m core diameter fibre.

Wavelengths above the top dot, on Fig.6.6, imply that  $(w/a) > 0.3$  which means that the energy of the Airy pattern is vignetted by the fibre core and falls off in a highly non-linear manner, both as  $\lambda$  increases and as the Airy pattern moves about on the fibre

end-face. Below the lower dot is the region at  $\lambda < \lambda_{min}$  in Fig. 6.3 where not enough modes are supported within the SMA to fully transmit all of the energy of the PSF. Notice that each of the on-axis through to 60 per cent off axis cumulative curves in Fig.6.5(d) are almost identical at each  $(w/a)$  even on the sloped part of the curve relating to the region below the dot on the vertical line in Fig.6.6. Hence, the field of view of the MMF on the sky is unaffected by the truncation of the MMF modes by the SMA in the Airy pattern feed case whereas the transmitted power becomes inversely proportional to  $\lambda^2$  for wavelengths less than the lower limit set by Eq.6.8, with

$$T = \left( \frac{\lambda_{min}}{\lambda} \right)^2 \quad \lambda < \lambda_{min} \quad (6.8)$$

### 6.3.3 Airy pattern coupling - Natural seeing

We now examine the effect, on the MPD, of coupling atmospherically degraded PSF's. From the results of section 6.3.1, in designing an OH-suppressing fibre system there is a trade-off between the need to decrease  $(w/a)$  to collect more energy and to reduce the number of modes,  $M$ , by increasing  $(w/a)$  since  $(w/a) \propto 1/\sqrt{M}$ . Fig.6.7 shows that the geometrical model is still applicable even under conditions of natural seeing that yield a speckle pattern in the telescope image plane. The reason for this is that regardless of how badly aberrated the PSF is, it is still the Fourier transform of the telescope exit pupil. Thence, regardless of how poor the seeing might be, the narrowness of the modal transform will always be limited by the limiting aperture of the telescope exit pupil.

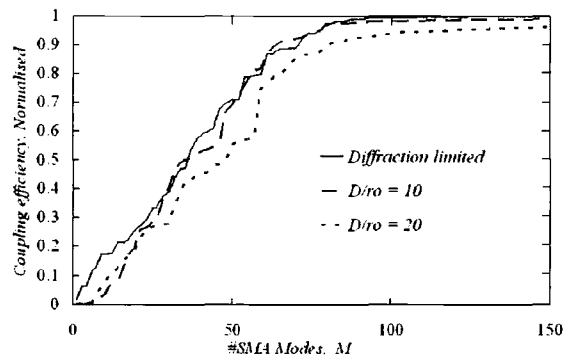


Figure 6.7 - A comparison of the MPD's of the diffraction limited,  $D_T/r_0 = 10, 20$  cases, where  $D_T$  is the telescope primary diameter and  $r_0$  the Fried parameter

Figure 6.8 is the same as Fig.6.6 but under conditions of natural seeing typically found on 4m and 8m class telescopes as in chapter 4. For each telescope/atmosphere, 1000 PSFs were generated using a Monte Carlo simulation, and for each one the coupling integral was evaluated. The atmosphere was simulated as a randomly generated Kolmogorov phase screen and the PSF was constructed using the far field approximation (by taking a fast Fourier transform (FFT) of the complex field in the telescope pupil). Perfect tip-tilt correction of the pupil phase was assumed, and the intensity in the telescope pupil was assumed to be uniform, that is, scintillation effects were not included. The geometrical relationship Eq.6.7 remains valid in conditions of natural seeing, but now the PSF is spread further out in the image plane due to the atmospherically degraded wavefront in the telescope entrance aperture. Therefore only some fraction of the energy in the PSF will couple into the fibre core of radius,  $a$ , with the remaining energy incident on the fibre cladding/buffer and therefore not transmitted by the fibre. As noted above, there is a trade-off between the need to minimise  $(a/F_T)$  to minimise  $M$  and to maximise  $(a/F_T)$  to reduce vignetting loss.

Figure 6.8(a) and 6.8(b) show that 84 per cent enclosed energy of  $\geq 800\text{nm}$  is only available to the 4m 7rz corrected telescope in  $r_o=15\text{cm}$  seeing. The rz figure is the maximum corrected radial zernike mode order. The 8m telescope can only reach significantly into the 1000nm-2000nm band with  $M>1000$  for this same 84 per cent throughput. The 50 per cent panels (c)-(d) show that  $M<200$  starts to match the performance of the 8m telescope for 12rz correction and 800nm in 15cm.  $M<100$  matches the 4m case well for 800nm in 15cm seeing. Panels (e)-(f) show that  $M<200$  and  $\geq 800\text{nm}$  yields  $>30$  per cent coupling on all but the 1rz 8m in poor ( $r_o=10\text{cm}$ ) seeing.

The amount of AO correction applied is indicated by the number of radial Zernike orders corrected, rz. For instance the 7rz and 12rz cases are high order corrections as typically found on 4m and 8m class telescopes, respectively, whereas 1rz is interpreted as tip-tilt only correction.

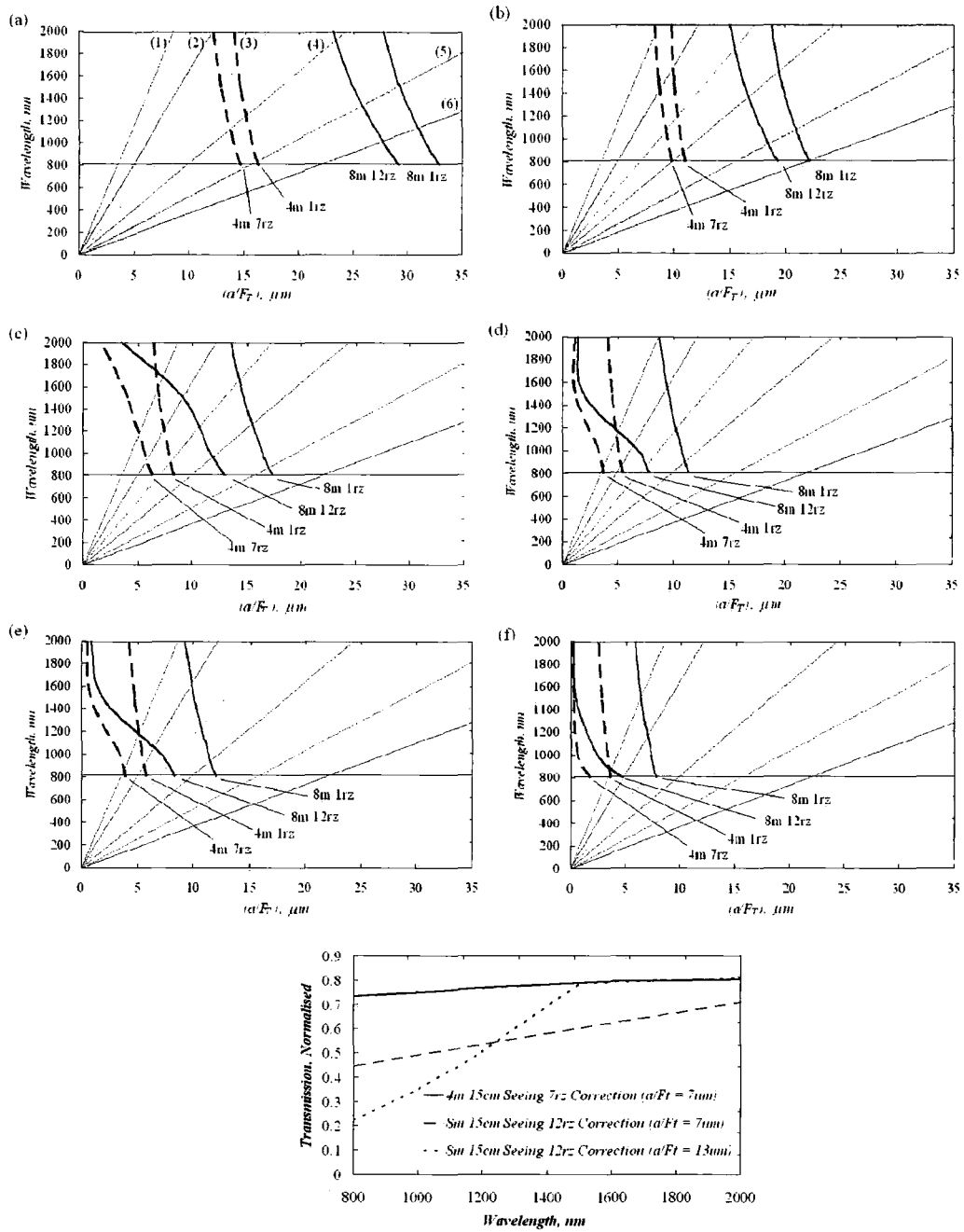


Figure 6.8 - The black lines in this figure represent (a) 84 per cent Enclosed energy within the fibre core diameter for  $r_o=10\text{cm}$  seeing (specified at 500nm), (b) 84 per cent Enclosed energy within the fibre core diameter for 15cm seeing, (c) 50 per cent Enclosed energy within the fibre core diameter for 10cm seeing, (d) 50 per cent Enclosed energy within the fibre core diameter for 15cm seeing, (e) 30 per cent Enclosed energy within the fibre core diameter 10cm seeing, (f) 30 per cent Enclosed energy within the fibre core diameter for 15cm seeing. The key is  $M = 50, 100, 200, 400, 1000$  and  $2000$ . 1rz is tip-tilt only corrected and 7rz and 12rz 7 and 12 radial orders of correction on 4m and 8m class telescopes, respectively, (g) Typical transmission spectrum of truncated fibres.

It would seem therefore that in the Airy pattern feed broad-band case (800nm-1800nm) the OH fibre suppression technique is rather better matched to 4m diameter telescopes with good AO correction than for larger apertures. Greater than 70 per cent coupling should be possible on 4m class telescopes in seeing of 15cm or better for  $M \geq 200$  and  $\lambda > 1000\text{nm}$ . However, from panels (b) and (d), the 8m class telescopes are accessible to  $M=200$  fibres if  $\lambda_{min}$  is kept to  $>1500\text{nm}$  by increasing  $(a/F_T)$ . To highlight this further, Fig.6.8(g) shows the theoretical transmission spectrum due to SMA truncation for various fibre devices. That is, the transmission as a function of wavelength for various fixed  $(a/F_T)$ . The 8m,  $(a/F_T)=7\mu\text{m}$  and 8m,  $(a/F_T)=13\mu\text{m}$  cases highlight that the larger fibre can be used to couple more light in for the same 'size' PSF but by Eq.6.7 this then increases  $\lambda_{min}$  to, in this case, 1500nm at  $(a/F_T)=13\mu\text{m}$ . For  $\lambda < \lambda_{min}$  the transmission falls off as a product of Eq.6.8 and the vignetting loss.

#### 6.4 Pupil Coupling

Fibre-based integral field spectrographs generally feed an array of fibres with a lenslet array, contiguous in the telescope image plane. If OH-suppressing fibres can be made cheaply enough, they might also find use in this application. The lenslet places an image of the telescope exit pupil on the end-face of the fibre, and in this section we investigate the properties of OH-suppressing fibres when illuminated in this way.

##### 6.4.1 Negligible spherical term - Ideal seeing

In the first instance we shall ignore any effects due to the projection of  $S_2$  onto  $U$ , in Fig 5.1 and assume that the spherical term is negligible as would be the case for very large  $f$  with respect to the fibre diameter, such as in many FRD experiments<sup>[6,7]</sup>. Figure 6.9 again highlights the decomposition relationship between the MPD and  $E_i$  since the 'modal transform' of the pupil function appears to very similar to an Airy pattern. Indeed, by increasing the obscuration the well known reinforcement of the first Airy minima occurs as  $\lambda$  increases<sup>[8]</sup>.

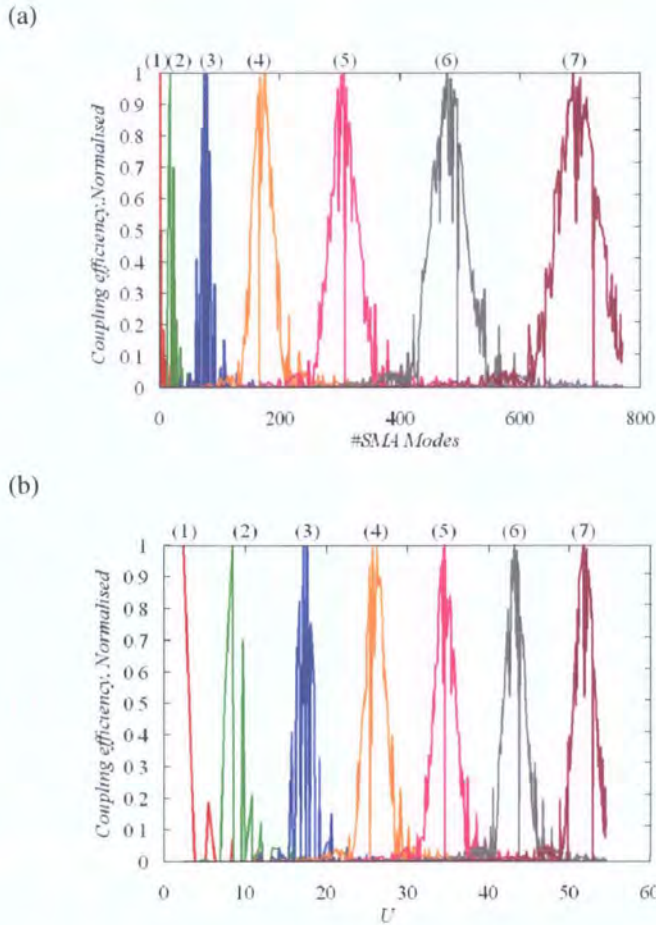


Figure 6.9 - (a) The variation in MMF MPD labelled on a scale of the SMA mode number (section 6.2.2), as the source moves off axis (1) On axis, (2)  $2^\circ$ , (3)  $4^\circ$ , (4)  $6^\circ$ , (5)  $8^\circ$ , (6)  $10^\circ$ , (7)  $12^\circ$ , (b) The variation in MMF MPD as a function of  $U$ , as the source moves off axis.

By ignoring the spherical term we can immediately align the ray optical model with the full electromagnetic field coupling analysis as shown in Fig.6.9(a,b). Here the fibre is illuminated with pupil images of an infinitely distant point sources at various equally spaced points from on-axis to the furthest possible physical extent, in this case the numerical aperture of the fibre at 0.22. The geometrical image  $E_{xg}$  is then given by

$$P.\exp(iknx\theta) \quad (6.9)$$

for pupil function  $P$  which takes value unity within the extent of the pupil image and zero otherwise. As,  $\theta$ , the angle subtended between the line of sight of the object and the fibre axis at the fibre end face, increases up-to the limiting value of the numerical

aperture of the fibre or the lenslet, whichever is smaller, the tilt in the field increases yielding  $\text{Re}(E_{xg})$  as shown Fig.6.10(a)-(c) for instance. The fine, diffractive, detail of the convolution of the pupil image with the lenslet PSF is included in these images. Unless otherwise stated, the lenslet is assumed, throughout this analysis, to have a focal ratio of  $f/5$ .

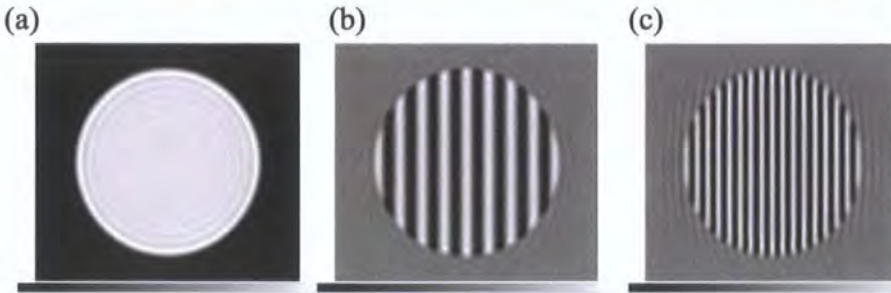


Figure 6.10 - Images of  $\text{Re}(E_{xg})$ , (a), On-axis, (b)  $6^\circ$  input at fibre end face, (c)  $12^\circ$  input at fibre end face. All with no Spherical term

With the Fourier like model in mind the mode carrying most power within the fibre is the one that best matches  $\theta$  in Eq.6.9. The broadening of MPD into an Airy pattern occurs because of diffraction, in the sense that the MPD is the modal transform of the image of the exit pupil of the telescope - an Airy pattern.

#### 6.4.2 Non-negligible spherical term - Ideal seeing

We now turn to the more realistic case, where the spherical image term in Fig 5.1 / Eq. (5.3) is not negligible. Fig.6.11(a) shows the MPD associated with a  $6^\circ$  angle of incidence at the fibre, for an  $\Theta=0.22$ ,  $50\mu\text{m}$  diameter core fibre fed with two different values of  $f_l$ , the focal length of the field lenslet. The increased angular distribution of light associated with the projection of  $S_2$  onto  $U(V)$  causes the MPD to be smeared out about the position of the Airy pattern, in the MPD, in the non-spherical case. Fig 6.11(b), is an example showing the significant extra width associated with even a value of  $(af_l)$  as a low as 0.05.

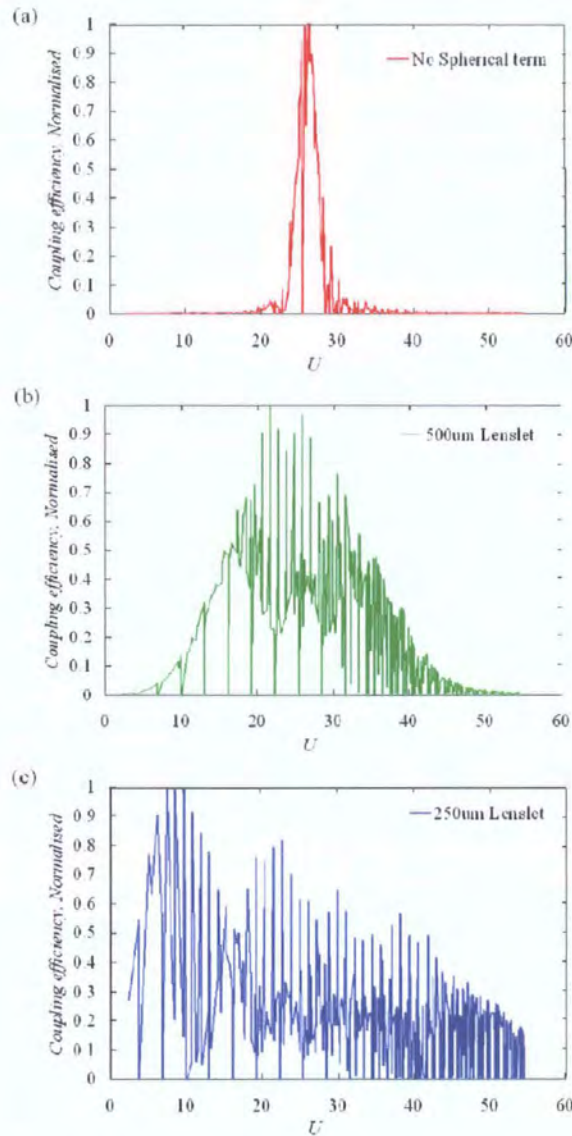


Figure 6.11 –  $50\mu\text{m}$  fibre core  $a=25\mu\text{m}$  fed with (a) No spherical term, (b)  $f_l = 500\mu\text{m}$ , (c)  $f_l = 250\mu\text{m}$

Geometrically we can think of the extra angular component as being due to the increased angle of incidence of rays associated with the projection of  $S_2$  onto  $U(V)$  as shown in Fig.6.12.

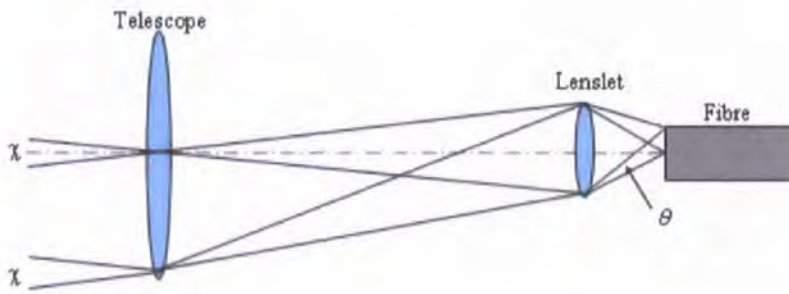


Figure 6.12 - The secondary focal ratio degradation model.  $\chi$  is the sample size on the sky

The increased angular range in  $A$  due to the curvature of  $S_2$  is given by,

$$\theta \approx \frac{a}{f_l} \quad (6.10)$$

This effect is more commonly known as secondary FRD (focal ratio degradation) and the increased range of input angles, greater than the focal ratio of the feeding lenslet, needs to be allowed for in deriving the relationship between  $\lambda_{min}$  and  $M$  in the lenslet fed case.

#### 6.4.3 The field of view as a function of $M$

In this section the relationship between the field of view of the fibre as a function of  $M$ , the number of modes within the SMA is derived. From the previous section, the MPD is directly related to the image of the telescope PSF and so implicit in figures 6.10 and 6.11 was that the telescope PSF was badly under-sampled - i.e. the entire telescope PSF passes through the lenslet and is therefore fully visible in the MPD. Generally the size of the lenslets in the telescope image plane would match, at least, the Nyquist sampling criteria of 2 pixels per resolution element. Therefore only some fraction, roughly half for critical sampling, of the telescope PSF would couple into the fibre. However, the aperture function of the lenslet, in the telescope image plane, forms the maximum extent of the telescope PSF coupled into the fibre, regardless of how badly it might be aberrated by the atmosphere and so the maximum range of angles that couple into the fibre in all atmospheres is given by,

$$\theta_{max} = \frac{1}{2F_l} + \frac{a_{image}}{f_l} \quad (6.11)$$

where  $\theta < \Theta$  and  $a_{image}$  is the radius of the pupil image, independent of the core radius. All of the quantities in Eq.6.11 are specified in the region immediately outside the fibre end face. e.g. If the lenslet has a refractive index of  $n_l$ , then  $F_l = n_l F_{air}$ . For  $\lambda < \lambda_{min}$  the input ray angle retained by the SMA is given from Eq.6.5 and Eq.6.6 as,  $\theta = (\sqrt{M\lambda})/(\pi n_l)$  where again  $\theta$  is specified within the feeding lenslet assumed in contact with the fibre end face. Equating this and Eq.(6.11) and re-arranging for  $\lambda_{min}$ , the minimum wavelength at which  $\theta_{max}$  is supported within the fibre, yields,

$$\lambda_{min} = \frac{\pi n_l \left( \frac{1}{2F_l} + \frac{a_{image}}{f_l} \right)}{\sqrt{M}} \quad (6.12)$$

Fig.6.13(a) is plot of Eq.(6.12), where  $F_l=7.25$ ,  $n_l=1.45$  and  $a=a_{image}$  and shows that for  $M \approx 200$  a wavelength independent field of view exists for  $\lambda_{min} > 800\text{nm}$  for only the smallest fibres core radii,  $a < 25\mu\text{m}$  and the largest focal length lenslets,  $f_l > 1000\mu\text{m}$ . A  $100\mu\text{m}$  diameter core fibre would require in excess of 250 modes just to access  $< 1600\text{nm}$ . However, more realistically, referring again to J and H band applications,  $M_{\lambda_{min}=1.15\mu\text{m}} = 87$  modes and  $M_{\lambda_{min}=1.49\mu\text{m}} = 52$  modes for the case of  $a=a_{image}=25\mu\text{m}$  and  $f_l=1000\mu\text{m}$ .

Notice also that the practice of under-sizing the image with respect to the fibre core, usually done to reduce losses from diffractive spreading of the pupil image at higher wavelengths and to avoid centration losses, decreases  $\lambda_{min}$  for the same  $M$ , or conversely decreases  $M$  for the same  $\lambda_{min}$ . For instance, there is a 10 mode decrease in  $M$  if  $a_{image}$  is reduced to 90 per cent of  $a$  with comparison to the  $a_{image} = a$  case, when  $F_l = 7.25$  and  $f_l = 1\text{mm}$  for the same  $\lambda_{min}$ .

Values of  $a$  smaller than  $25\mu\text{m}$  are shown for information in Fig.6.13 but are rarely found due to the practical difficulties of lenslet alignment.

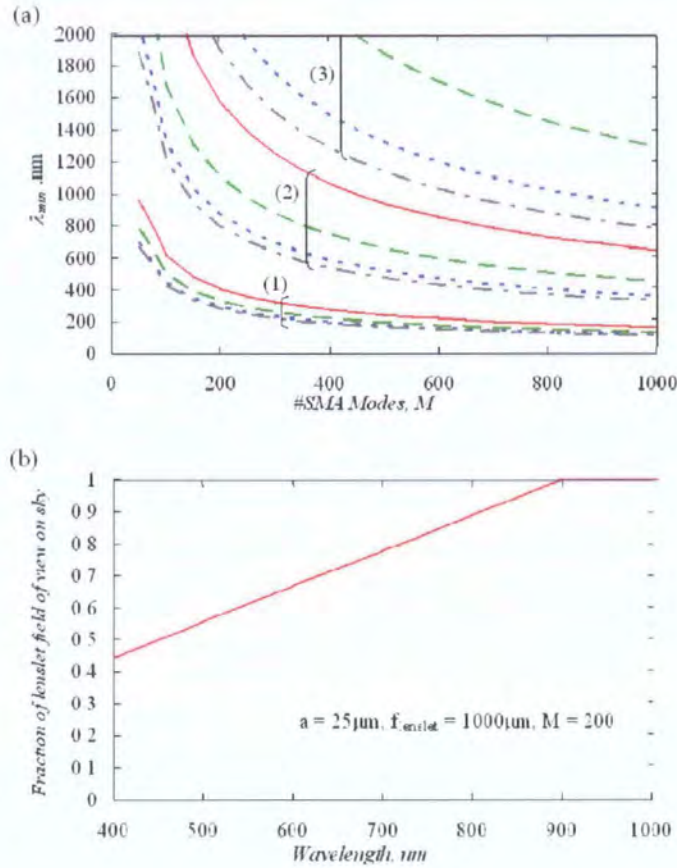


Figure 6.13 (a) The minimum wavelength that guarantees a wavelength independent field of view for the case of  $F_l = 7.25$ , in  $n_l = 1.45$  typically used to avoid FRD issues, (1)  $a = 10\mu\text{m}$ , (2)  $a = 25\mu\text{m}$ , (3)  $a = 50\mu\text{m}$ , (dot-dash)- $f_l = 1500\mu\text{m}$ , (dots only)-  $f_l = 1000\mu\text{m}$ , (dashes only)-  $f_l = 500\mu\text{m}$ , (solid)-  $f_l = 250\mu\text{m}$  (b) the fraction of the on-sky field of view as a function of wavelength for the case of  $a = 25\mu\text{m}$ ,  $f_l = 1000\mu\text{m}$  and  $M = 200$ .

Fig.6.13(b) shows how the fraction of the on-sky field of view of the truncated fibre changes with  $\lambda$ , for the case of  $a = 25\mu\text{m}$ ,  $f_l = 1\text{mm}$  and  $M = 200$ . Notice that if the telescope PSF is well sampled then this reduction in the field of view would, as in the Airy feed case, manifest itself as a reduction in transmission with the square of  $\theta$ .

#### 6.4.4 Sampling performance of OH suppression fibres

We have computed the PSF's of 4m and 8m telescopes under various conditions of seeing and AO correction, as in section 6.3.3. The  $a = a_{image} = 25\mu\text{m}$  case was considered as a sensible minimum  $a$  for alignment purposes with  $F_l = 5$  in air and  $f_l = 1\text{mm}$  chosen to minimise primary and secondary FRD, respectively. By the conservation of etendue then  $F_T = 14$  and the size of the lenslet in the telescope image plane is  $140\mu\text{m}$ .

4m Telescope	10cm 1rz	10cm 7rz	15cm 1rz	15cm 7rz
Wavelength, nm	FWHM, $\mu\text{m}$	FWHM, $\mu\text{m}$	FWHM, $\mu\text{m}$	FWHM, $\mu\text{m}$
800	235	176	151	104
1000	218.5	156	143	92
1500	194.5	113.5	126	32.3
2000	179	47.5	115	6.4

Table 6.1 - FWHM of the 4m telescope PSF in various atmospheres and degrees of correction.

8m Telescope	10cm 1rz	10cm 12rz	15cm 1rz	15cm 12rz
Wavelength, nm	FWHM, $\mu\text{m}$	FWHM, $\mu\text{m}$	FWHM, $\mu\text{m}$	FWHM, $\mu\text{m}$
800	486	370	318	219
1000	459	322	299	190
1500	411	258	267	52.5
2000	378	98	243	39.2

Table 6.2 - FWHM of the 8m telescope PSF in various atmospheres and degrees of correction.

From Tables 6.1 and 6.2 we see that the sampling of the example fibre+feed is rather better matched to the 8m telescope with near critical sampling of the full width half maximum, FWHM, of the PSF in 10cm seeing and 12 radial orders of correction in the H band and in the J band for tip-tilt only in  $r_0 = 15\text{cm}$  seeing. The fibre is not well matched to the 4m telescope with the PSF under-sampled even in poor seeing and only tip-tilt corrected. Since by the conservation of etendue,  $F_T = (1=2n)(f_l=a)$ , then increasing  $F_T$  to better match the sampling of the 4m telescope would require a

decrease in  $(a=fi)$  which by Eq.(6.12) would decrease  $M$  due to the decreased secondary FRD, Eq.(6.11).

As noted above, on the 8m telescope taking  $a = a_{image} = 25 \mu m$  and  $f_i = 1000 \mu m$ ,  $M = 87$  and  $M = 52$  modes, respectively, are required to access  $\lambda_{min} = 1:15 \mu m$  and  $\lambda_{min} = 1:49 \mu m$ . To increase  $F_r$  by a factor of two, say, to match the sampling of the 4m telescope,  $M$  thence decreases to 65 and 39 modes, respectively. This can be achieved by leaving the fibre core diameter as  $50 \mu m$  and  $f_i = 1000 \mu m$  and then reducing the radius of the pupil image (by increasing  $F_r$ ) to  $a_{image} = 12:5 \mu m$ .

#### 6.4.5 *The effect of de-focusing, demagnification and de-centration of the pupil image on the MPD.*

Since an adhesive layer typically exists at the lenslet/fibre boundary it is common practice to have the focus of the lenslet somewhere just inside the face of the fibre to avoid scattering from defects within the glue. De-centration of the image on the fibre core is also sometimes an issue with the alignment of lenslet arrays with many, potentially very small fibres, a challenging task. However, as has been shown at various points throughout this chapter it is the geometrical ray model that dominates, even when relatively few modes are supported within the MMF. Since the angular range of modes entering the fibre is not effected by either deliberate de-focussing or de-centering or demagnification of the image with respect to the core size then, to first order, the results of section 6.4 are not altered by these effects.

### 6.5 *Summary*

A simple model of an OH-suppressing fibre as proposed by Bland-Hawthorn *et al* <sup>[2]</sup> and demonstrated in the lab by Leon-Saval *et al* <sup>[1]</sup> has been presented in order to determine how these devices behave on telescope. This general analysis is necessarily presented to an accuracy of <10 per cent due to issues surrounding mode counting near cut-off and the much smaller uncertainties associated with the coupling calculation.

When fed with an Airy pattern, the field of view of the fibre is unaffected by the number of cores/modes in the SMA array,  $M$ , but the transmission of the device

becomes wavelength dependent below some minimum wavelength. The atmosphere was shown to have a significant effect on the performance with the competing needs of reducing  $M$ , for manufacturability, whilst increasing the size of the fibre in order to couple more light in from the aberrated telescope PSF. Throughput of greater than 50 per cent was found to be possible at  $>800\text{nm}$  on well corrected (7rz) 4m class telescopes for  $<200$  modes at  $>1500\text{nm}$  for the same fibre on an 8m telescope. More realistically, the J and H bands can be accessed at  $>80$  per cent throughput with  $<200$  and  $<100$  modes, respectively on the well corrected (7rz) 4m class telescope in 15cm seeing but this reduces to 50 per cent coupling for the same fibre on the 8m class in the same seeing.

In the pupil-fed case, and assuming that the PSF is well sampled by the feeding lenslet, the field of view of the fibre was shown to become wavelength dependent, again below some minimum wavelength. In this case, the natural scales associated with fibres supporting 80-120 modes were found to match the sampling requirements of well corrected (12rz) 8m telescopes and tip-tilt corrected 4m telescope both in  $r_0=15\text{cm}$  seeing in the J and H bands. Whether or not OH-suppressing fibres find use in IFS will depend largely on how easy (and therefore cheaply) they can be manufactured in bulk.

## 6.6 References

- 1) 'Multimoded fiber devices with singlemode performance', SG Leon-Saval, T Birks, J Bland-Hawthorn and M Englund, *Opt. Lett.* **30**, 2545. (2005)
- 2) 'New approach to atmospheric OH suppression using an aperiodic fibre Bragg grating', Bland-Hawthorn J, Englund M and Edvell G, *Opt. Exp* **12**, 902 (2005)
- 3) Birks – private correspondence (2006)
- 4) "Number of modes on optical waveguides.", C Pask A Snyder, D Mitchell, *JOSA*, **65**, 356 (1975)

- 5) 'Optical Waveguide Theory', A Snyder & JD Love, Kluwer (1983)
- 6) Ramsey L., Barden S., ASP Conference series – Fibre optics in astronomy, 3 (1988)
- 7) "On the application of optical-fiber image scramblers to astronomical spectroscopy" WD Heacock, AJ, 92, pp. 219-229, (1986)
- 8) 'Diffraction Images in Systems with an Annular Aperture', EH Linfoot & E Wolf, Proc. Phys. Soc. LXVI, I-B (1953)

# Chapter 7

---

## *Fibre modal noise*

### **7.1 Introduction**

In this chapter we once again touch on the EM model of light propagation along the fibre in order to describe the effects of 'fibre modal noise'. However, due to the, generally, very large number of modes involved, in much the same way that the ray model replaces the EM model when describing optical propagation along the fibre, so in this case the EM model is replaced by a more appropriate statistical model.

Fibre modal noise is a photometric uncertainty on a resolution element of a spectrograph detector. The very small spectral element  $\delta\omega$  associated with high resolution spectroscopy causes the many modes supported within the fibre feeding the spectrograph to interfere with each other coherently at the output end face of the fibre. The scattering of energy between modes from inclusions in both core/cladding interface and within the core itself cause a speckle pattern that remains static when the fibre is at rest but is subject to pseudo-random changes when the fibre is moved. Telescope tracking thus results in a photometric error on the resolution element of the detector that cannot be calibrated out.

Modal noise was a well known and characterised problem in fibre optic communications in the 1970's but in high spectral resolution astronomical spectroscopy the problem was first reported by Baudrand *et al* <sup>[1]</sup> and has since been the subject of papers by Baudrand & Walker<sup>[2]</sup> and Grupp<sup>[3]</sup>.

This chapter contains an explanation of how the coherence of the fibre illumination causes modal noise in section 7.2, the results of a relevant literature search in section

7.3 which then motivates the experimental investigation of modal noise using a purpose built high dispersion spectrograph in sections 7.4 onwards.

## 7.2 What is modal noise?

A distant on axis point source<sup>9</sup> and the resulting spatially coherent field is incident at the telescope entrance pupil (thence re-imaged onto the fibre end face) as in figure 7.1. Each source can be thought of as an input ‘beam’ to the fibre exciting a number of modes – Chapter 5.

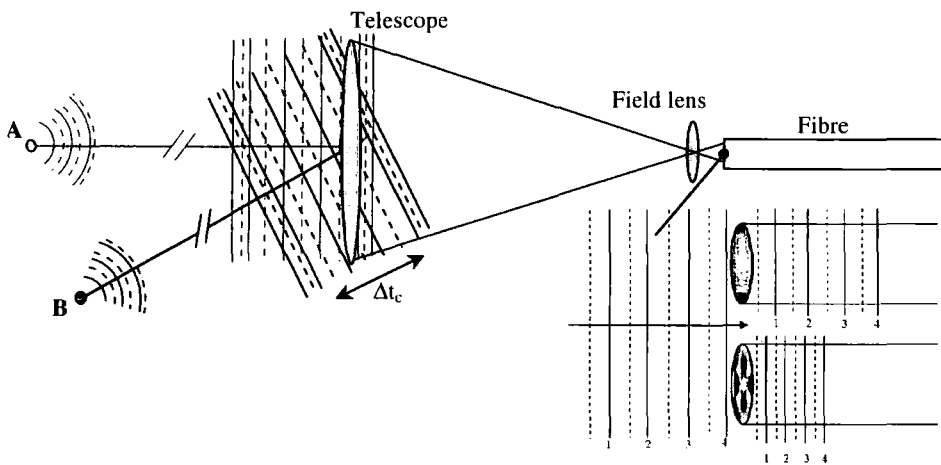


Figure 7.1 –The fields of two partially (temporally) coherent sources superpose in the entrance pupil of the telescope. The  $HE_{11}$  and  $HE_{32}$  modes travel different distances along the fibre for the same number of temporal oscillations of a single frequency component from the total incoming wavepacket. Each mode shown in a separate fibre for clarity.

We know from Chapter 2 that the coupling efficiency of some incident field into the fibre end face is governed only by the transverse part of the incident and modal fields in the plane  $P-P'$ , in Fig. 7.2. The incoming wavepacket, from source **B** in Fig.7.1 say, can be decomposed into its Fourier frequency components along any line of

<sup>9</sup> A source of light large enough to contain many atoms but small enough to be considered as small macroscopically. Actually this does not include stellar objects. Stars are enormous and for the rather precise nature of this analysis should be considered as populating a small range of input beams at such large distances. Were this not the case, then stellar interferometry would not work at all! The usual assumption of a plane wave input due to an entire star is, of course, related to the unresolved image of the star by the telescope.

propagation such as the arrow in Fig.7.2 or any other line parallel to it. Therefore the incoming wavepacket can be considered to be a superposition over a continuum of beams of separate angular frequency,  $\omega$ , Fig.7.2(b), within the  $\Delta\omega$  of the wavepacket. The projection of each component beam onto the fibre end face can then be given by

$$E(\omega) \propto \exp(iknx\theta) \exp(-i\omega t + \phi) \tag{7.1}$$

where the  $x$ -axis is chosen to lie within the plane of P-P' without loss of generality due to the circular symmetry of the core,  $k$  is the free space wavenumber,  $n$  the refractive index immediately outside the fibre.  $\phi$  the phase constant of the Fourier component. Each beam at angle  $\theta$  will excite a range of modes within the fibre, yielding some modal power distribution (MPD). The MPD will vary with different values of  $(knx\theta)$  but as long as  $\Delta k$  is small then we can ignore any MPD variation over the small  $\Delta\omega$ . i.e all Fourier components populate approximately the same MPD. Since the coupling is due only to the transverse spatial portion of Eq. (7.1) with the time term invariant across the boundary, thus the phase differences between the components of the wavepacket are retained across the boundary, P-P'.

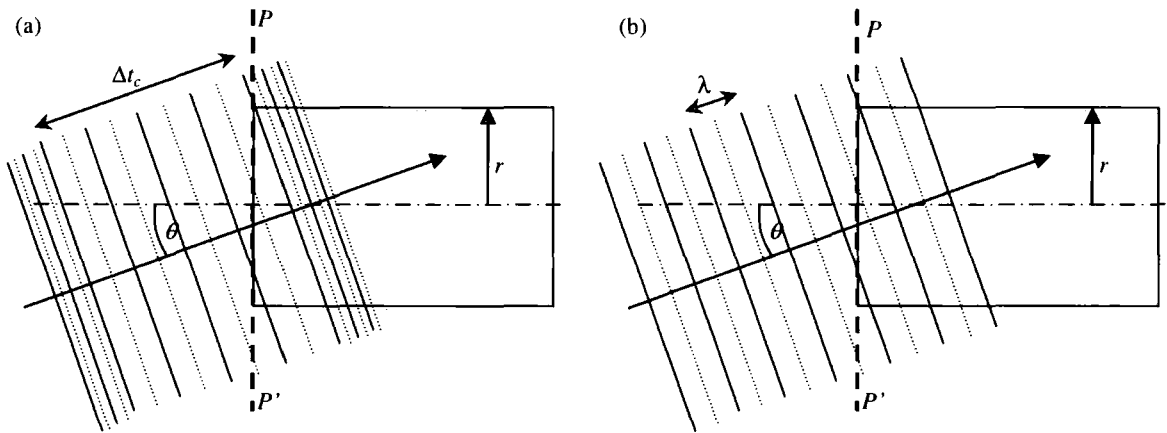


Figure 7.2 –(a) A single wavepacket incident on the fibre end face. (b) The coupling of a single Fourier component from the wavepacket .

The phases of the frequency components that go to make up a single wavepacket have a constant phase relationship with respect to each other but with a random relationship with the components in other packets, due to the random times of arrival at some point

in space of the wavepackets making up the total wavetrain. The total wavetrain is only considered to be coherent for times less than the coherence time of the component wavepackets. At any one point in space the wavetrain is made of many wavepackets superposing and randomly phased with respect to each other. However, the smaller the interval of observation,  $\delta t$ , is with respect to  $\Delta t_c$ , the coherence time of an individual wavepacket and of course requiring that  $\delta t < \Delta t_c$ , the more *likely* the total disturbance will be coherent over  $\delta t$  when averaging over many wavepackets. The coherence length is the upper limit above which it is impossible for two separate points to be correlated.

Since we are dealing with a very small  $\Delta\omega$  an excited mode,  $i$ , travels at the modal group velocity  $V_{gi}$  as given by Eq. 2.5 and hence the mean time taken for the wavepacket to traverse a fibre of length,  $L$ , is  $t_i = L/V_{gi}$ .

The total energy of the wavepacket is distributed amongst a range of modes. Dispersive effects within each mode must work to increase the length of each wavepacket and thence increase the coherence<sup>[4]</sup>. However modal noise is dominated by *intermodal* effects and thence *intramodal* dispersion is ignored. Each mode considered separately, then, travels different distances along the fibre in the same elapsed time. The inset in Fig 7.1 shows how a single monochromatic components travels different distances along the fibre, in the same time, due to the different propagation constant,  $\beta$ . In simple general terms, modes excited by a single source can interfere to some degree if they are separated at the output end face of the fibre by less than the coherence time of one of the wavepackets that go up to make the incoming wavetrain. i.e.  $|t_i - t_j| \ll \Delta t_c$ , where  $t_j$  refers to the  $j^{\text{th}}$  mode. If  $|t_i - t_j| > \Delta t_c$  the two modes must be excited at all times by different, incoherently, related wavepackets and they will sum in intensity for all times and not contribute to the speckle pattern.

Unlike most fibre applications, such as communications, it is, therefore, the *lack* of intermodal dispersion for some given fibre length,  $L$ , that is detrimental to good performance.

### 7.2.1 Effects of an arbitrary field of view – Perfect fibre.

If the spectral resolution is the same over the entire input field then the temporal coherence of each input beam (A,B, etc.....in Fig. 7.1) is the same. What happens if

energy from two separate (incoherently related) input beams couples into the same mode? Coherent behaviour is a statistical phenomenon whereby the number of identical wavepackets observed is very large. Hence,  $N$  wavepackets per second from source A plus  $M$  wavepackets per second from source B, both observed at the same spectral resolution yields the same coherence properties in a mode as  $M + N$  wavepackets per second from a single beam.

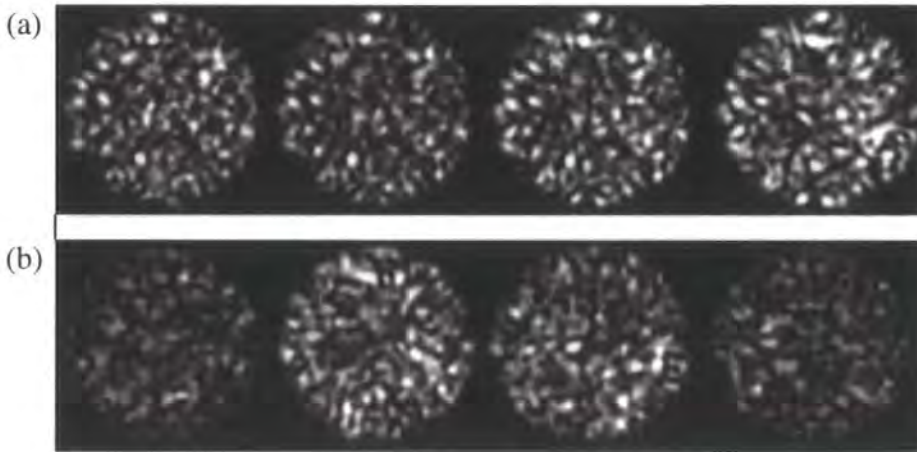


*Figure 7.3 – Demonstration that the input image changes the speckle image at the output of the fibre. (a) Fibre near-field images (Linear intensity scale) taken for field tilts in the telescope entrance pupil image placed on the fibre input end face due to off axis point sources. Tilt increases from left to right, (b) Speckle images taken for lateral offset of pupil image with respect to the fibre core. Increasing offset from left to right. Both sets of images taken with no movement of the fibre between exposures. Note the large changes in (b) images when compared to the relatively small changes in (a) images.*

As the distribution of the input illumination on the fibre end face changes then different modes are populated within the fibre and this can alter the speckle pattern at the fibre output since the power distribution within the modes of the fibre is then altered. Figure 7.3 shows some examples of speckle patterns as the telescope exit pupil image is moved about over the input end face of the fibre and with tilt in the field due to a perfect point source. The light used to populate the pupil was from a laser. Note that the changes in the speckle pattern are far more significant for the pupil offset than the field tilt.

### 7.2.2 The effects of non-perfect fibres.

Any real waveguide will have micro-bends and scattering centres in the core/cladding walls and even inclusions in the core itself which affect the speckle pattern in a complicated, pseudo-random manner. With no fibre movement, ray directions are altered by non-uniformities in the fibre wall and indeed from scattering centres within the core itself. These non-uniformities include both microscopic inclusions and the molecular granularity of the component materials. See Fig 7.4 for a ray optical model interpretation of this phenomenon, where each mode has only a single ray angle associated with it and so energy is scattered amongst the modes. The positions of the scattering centres are randomly positioned along the fibre and the phase relationships amongst the modes (even if excited by only one wavepacket) is different at different  $z$  due to intermodal dispersion. Hence the light scattered into a mode from many other modes does so at many different phase values and a pseudo random phase and amplitude variation is introduced to each mode as it travels along the fibre resulting in a static speckle pattern on the fibre output. This scrambling of energy amongst the modes is known to instrumentalists as focal ratio degradation, (FRD).<sup>[5,6]</sup>

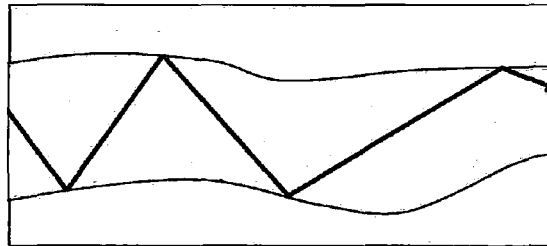


*Figure 7.4 – Ray optical model showing how the propagation of energy within the fibre can be affected by perturbations within the fibre.*

As the fibre is moved, the speckle pattern changes due to the stressing/de-stressing of micro-bends and differing macro-bend radii. Once the fibre is brought to rest again the speckle pattern will be static but whilst moving a varying speckle pattern will be observed even for static spatial distribution at the fibre end face. FRD increases as the mechanical stress on the fibre increases but even the smallest perturbations of the fibre are generally enough to cause the speckle pattern to change without apparently affecting the FRD performance.

To summarise: For a static fibre, the speckle pattern does change due to a changing spatial distribution of the source due to the different modal power distributions excited by an arbitrary source distribution. Modes separated by less than the coherence length of the transported light can interfere to some degree causing a speckle pattern in the fibre near-field. Macro, micro and molecular perturbations along the fibre cause a pseudo-random amplitude/phase redistribution amongst the modes to occur that remains static when the fibre is held firm but will change for each static position of the fibre.

Finally then, all of the above highlights the fact that if the detector resolution element in the spectrograph spans a small enough  $\Delta\omega$ , i.e. a high enough spectral resolution, then an uncertainty in intensity exists due to the static speckle pattern which will be different at different (static) fibre positions along with the random uncertainty in intensity associated with the movement of the fibre and the subsequent changing speckle pattern on the resolution element. The dynamic uncertainty due to the fibre motion is the one most typically associated with spectral noise, of course.

### 7.3 *How is modal noise described?*

We have already discussed that the end face of the fibre has the appearance of a speckle-like pattern and how the speckle pattern is created from the point of view of the fibre modes and the source of illumination. However, like previous chapters, the EM mode description of modal noise is overly complex for general use and it is perhaps not surprising then that, once modal noise had been identified<sup>[7,8]</sup> much investigative work was based on generalised speckle analysis, with a few examples in references<sup>[9-11]</sup>.

The work by Goodman & Rawson<sup>[10]</sup> highlighted the drawbacks of this approach and replaced the previously assumed negative exponential statistics, i.e. the statistics of the signal to noise with respect to fibre properties and illumination, with Beta statistics. Negative exponential statistics predict that the limiting modal noise should be numerically equal to  $\sqrt{M}$  where  $M$  is number of populated modes within the fibre. However, beta statistics correctly describe the fact that for no loss-dependent mechanism such as a misaligned fibre connector or vignetting by the optical system

used to place the fibre end face image on the detector and an infinite number of populated modes, the  $S/N$  should trend to infinity. They also went on to provide a simple formula for the expected  $S/N$  as a function of the number of modes populated within the fibre,

$$S/N = \rho \sqrt{\frac{M+1}{1-\rho^2}} \quad (7.2)$$

where,

$$\rho^2 = A_d/A_f \quad (7.3)$$

for  $A_d$ , the fraction of the area of the fibre end face imaged onto the detector and  $A_f$  the area of the fibre end face.  $\rho$  is dimensionless.  $M \gg 1$  is assumed.

Goodman, Rawson and Norton<sup>[12]</sup> state that the [number of modes] = [the number of speckles] in the near-field. Therefore, as long as there are many modes and therefore many speckles, Eq.(7.3) can be interpreted as  $\rho^2$  selecting out a fraction,  $A_d/A_f$  of the modes supported within the fibre.

Baudrand and Walker found a poor correlation between the negative exponential based statistical theory and their experimental results, however, equations (7.2) and (7.4) can be used to get a much closer correlation. They used  $f/4$  and  $f/2.8$  inputs to the fibre from a calibration source and noted that they made significant efforts to ensure that all light from the fibre end face found its way onto the detector. Taking, initially,  $\rho^2 = 0.995$  then, as noted in Chapter 6, an approximation to the number of modes travelling within the fibre is given by

$$M = V^2/2 \quad (7.4)$$

for  $V = ka\Theta$ , where  $k$  is the free space wavenumber and  $a$  the fibre radius although Eq.(7.4) is computed using the input focal ratio rather than the numerical aperture of the fibre. At 500nm signal to noise levels of 780 and 1100 should be expected for the  $f/4$  and  $f/2.8$  cases, respectively. These expected values are far closer to the measured  $S/N$  1300 in both cases than the expected values of the negative exponential model of

56 and 80, respectively. It is not clear why no difference in  $S/N$  was measured for different focal ratio inputs. Possibly scattering within the fibre meant that  $f/4$  and  $f/2.8$  inputs both led to something like an  $f/2.8$  output via FRD. Further, the output lenslet system described in the paper indicates an  $f/3.5$  output. The  $S/N$  expected in the  $f/3.5$  case is 1280.

However, it should be noted that very large variation in expected  $S/N$  occurs for relatively small changes in  $\rho^2$ . Taking  $\rho \in [0.99, 1.00]$ , Fig 7.5 shows that Eq.'s(7.2) and (7.4) are a much better match for the  $S/N$  as a function of wavelength than the negative exponential model. However, for even a modest 5% loss, the predictions are inaccurate by a factor of 3 – curve (2) in the figure. It would appear that it is possible to dial up an answer to some extent. Note further, that Baudrand & Walker<sup>[2]</sup> did not include error bars on their data.

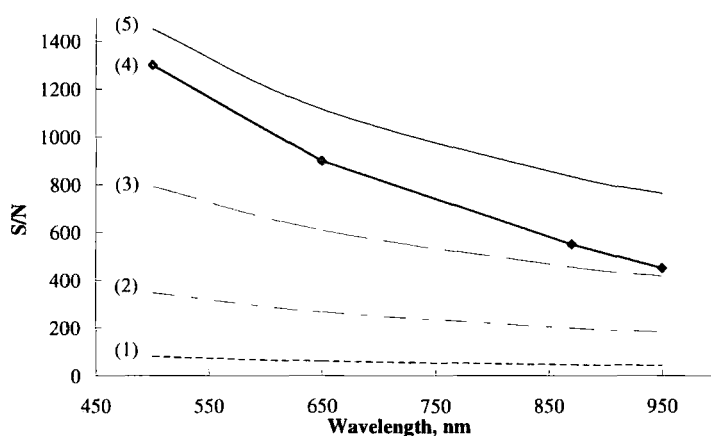


Figure 7.5 – Comparison of Baudrand & Walkers experimental data with Rawson and Goodman's models. (1) The original and incorrect negative exponential statistical model, (2) the Beta statistical model,  $\rho^2=0.95$ , (3) the Beta statistical model,  $\rho^2=0.990$ , (4) Baudrand &Walkers experimental data, (5) the Beta statistical model,  $\rho^2=0.997$ .

Grupp's work<sup>[3]</sup> went one step further than that of Baudrand & Walker deriving an expression for the noise per signal of

$$N/S = \frac{I}{\sqrt{M}} \sqrt{\frac{1-g}{g}} \quad (7.5)$$

where  $g$  is the fraction of the vignetting of the input focal cone into the fibre by the spectrograph entrance slit (at the fibre output)<sup>10</sup>. Hence,  $g = \rho^2$  and substituting this into Eq.(7.5) and rearranging yields,

$$S/N = \rho \sqrt{\frac{M}{1-\rho^2}} \quad (7.6)$$

Equations (7.2) and (7.6) are almost equivalent and hence both Baudrand & Walker and Grupp's results can be seen to be closely aligned with the Beta statistical model of Goodman & Rawson.

However, Grupp then achieves a good correlation between experiment and theory with a single example with no error bars using a  $V$  value in his model inaccurate by a factor of two, since he used the fibre diameter instead of the radius in Eq. (2.7). As in the case of Baudrand & Walker, then some considerable doubt must be cast on the validity of Eq.(7.6) in this application.

Rawson, Goodman & Norton<sup>[13]</sup> have derived a frequency correlation function (FCF) that computes the correlation between the mean field intensity computed over the fibre near-field with one mean per fibre position then averaged over many fibre positions at one wavelength, with the same spatial/fibre position average at another wavelength. The model is derived for a planar waveguide but with approximate applicability to circularly symmetric fibres if  $\rho^2 < 0.5$ .

---

<sup>10</sup> Grupp assumes no FRD occurs due to the relatively fast input beams used on the FOCES spectrograph<sup>[3,14]</sup>.

The following relationship can be derived from the FCF,

$$\Delta\lambda \cong \frac{1.5n\lambda^2}{L\Theta^2} \quad (7.7)$$

where,  $\Delta\lambda$  is the spectral width of the FCF between correlation values of 1.0 ( $\Delta\lambda=0$ ) and 0.1 ( $\Delta\lambda > 0$ ),  $c$  is the speed of light in a vacuum,  $n$  is the core refractive index and  $L$  is the length of the fibre.  $\Theta$  is the numerical aperture of the fibre. On a single resolution element of the detector,

$$\Delta\lambda_s = \frac{\lambda}{R} \quad (7.8)$$

and for  $\Delta\lambda = \Delta\lambda_s$ ,

$$R_{crit} = \frac{L\Theta^2}{1.5n\lambda} \quad (7.9)$$

So, according to the model, we can expect speckle effects to be important for  $R > R_{crit}$  and reductions in speckle are then associated with increased  $L$ , high  $NA$  or low  $\lambda$ . In most general purpose fibres, very short wavelength are typically associated with lower throughput and so there will be some trade-off in the throughput-resolution product at very low  $\lambda$ , dependent on the attenuation spectrum of the fibre.

In the Baudrand & Walker case,  $\Delta\lambda_s = 4.3 \times 10^{-3} \text{ nm}$  at 650nm (and  $\Delta\lambda_s = 3.3 \times 10^{-3} \text{ nm}$  at 500nm and  $\Delta\lambda_s = 6.3 \times 10^{-3} \text{ nm}$  at 950nm). Baudrand & Walker found no difference in  $S/N$  values for 7.0m and 70m of fibre and using the values from their experiments it is possible to compute from Eq.(7.7),

$$\Delta\lambda(L = 7.00m) = 2.71 \times 10^{-3} \text{ nm} \quad (6.69 \times 10^{-3} \text{ nm}) \quad (7.10)$$

$$\Delta\lambda(L = 70.0m) = 2.71 \times 10^{-4} \text{ nm} \quad (6.69 \times 10^{-4} \text{ nm}) \quad (7.11)$$

Since  $\Delta\lambda_s > \Delta\lambda(L = 7m)$  then Eq.(7.10) predicts that significant decorrelation in the speckle must have occurred and since  $\Delta\lambda_s > \Delta\lambda(L = 70m)$  also then the failure to

detect a difference between 7.0m and 70m could be due to the fact that both cases are somewhat decorrelated. The figures in brackets in Eq.7.11/12 are for the observed  $\Theta = 0.14$  output of the fibre ( $f/3.5$ ) and even in this case it is possible to interpret the same result for 7.0m and 70m on the basis of approximately equal values of the FCF, although less clear cut in this case. So the match between Eq. (7.9) and the results of Baudrand and Walker, is rather poor and further testing of Eq. (7.9) is required. Certainly from a practical point of view, the issue of fibre length is very significant.

In 1984 Thomas H. Wood<sup>[14]</sup> published a short work that calls into question the validity of the statistics of the Goodman & Rawson<sup>[11]</sup> model for arbitrary illumination of the fibre as would occur during an on sky measurement, such as some point source, for instance. He found highly varying values of  $S/N$  ratio for various Gaussian beam inputs from a semiconductor laser. The variation was found to be due to the sparsely populated MPD whereas a central assumption in the work of Goodman & Rawson is that an infinite number of populated modes exists.

The MPD was found to be heavily biased towards a few lower order modes and the mode selective mechanism (in this case a fibre-to-fibre transverse offset) preferentially selected out higher order modes, as does a spectrograph entrance slit. The signal to noise was found in some cases to be twice that of the uniform MPD case. Saijonmaa & Halme<sup>[15]</sup> and Papen & Murphy<sup>[16]</sup> found similar results for restricted launch conditions at the fibre end face. Indeed the results of Chapter 5 indicate how wildly the MPD changes with even small changes in illumination.

The data recorded by Baudrand & Walker and Grupp were from calibration sources which in all likelihood populated nearly all available modes within the fibre. Indeed a Lambertian source, such as a calibration lamp in the case of Baudrand & Walker is known<sup>[17]</sup> to populate all modes within a fibre. The Lunar spectra of Grupp would certainly have filled the input aperture to the fibre and so populate close to all of the very large number of available modes within this aperture. However, Fuhrmann *et al*<sup>[18]</sup> note that the  $S/N$  was limited to 200 on various stellar observations. Wood's work shows clearly that the  $S/N$  noise will change with the MPD and so either the magnitude of the changes in  $S/N$  associated with the fibre MPD excited by a stellar source are small enough that the final  $S/N$  ratio, at the FOCES spectral resolution(s), is

unaffected or that the poor seeing of the observations may have had a significant effect.

In light of all of the above, it would seem that a systematic, experimental, investigation of the properties of modal noise with fibre/spectrometer parameters is required. The work completed to this end is described in the next section.

#### 7.4 Experimental investigation of modal noise – Experimental setup

In order to demonstrate and investigate further the effects of modal noise a high dispersion spectrometer was built. The spectrometer design is discussed in the next section, with modal noise results presented and discussed from section 7.5 onwards.

##### 7.4.1 Spectrometer design

Figure 7.6 shows the basic spectrometer configuration referenced throughout the rest of the chapter. The pictures show the apparatus under construction, prior to the blackout covers being put on. The test grating was used with the same included angle,  $\Psi$ , (but different  $\alpha$ ) so that the optics could be set-up prior to the delivery of the echelle.

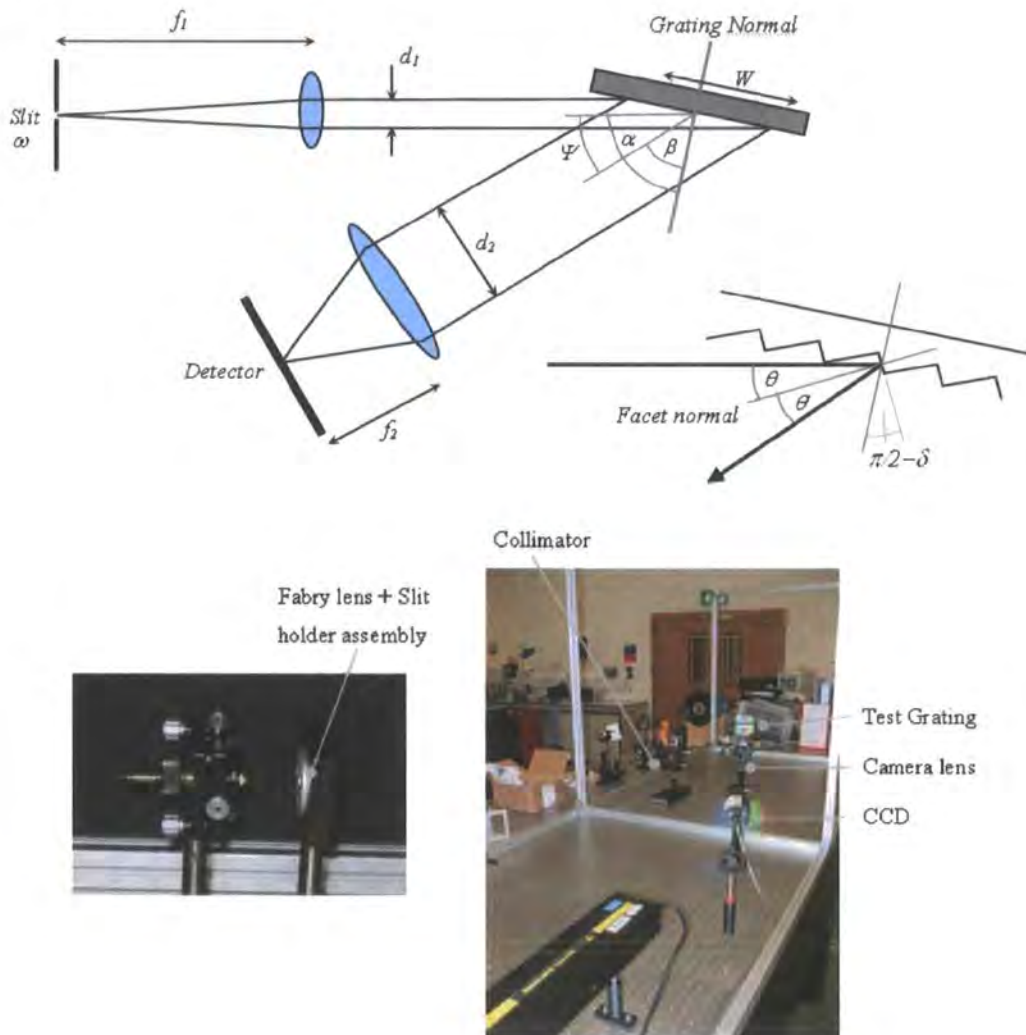


Figure 7.6 – The basic spectrometer configuration. See figure 7.8 for slit,  $\alpha$  geometry. The detector was a Q-Imaging Retiga EX.

The resolving power,  $R$ , of the spectrometer shown in the figure may be given as

$$R = \frac{2 f_l \sin \delta \cos(\theta)}{w \cos(\delta + \theta)} \quad (7.12)$$

where  $\delta$  is the blaze angle of the grating. Hence in order to increase  $R$ , the ratio  $f_l/w$  must be maximised. The maximum grating efficiency occurs when the diffracted beam exits the grating at the blaze peak. The net effect of blazing a grating is for this peak to occur in the direction of the specular reflection ( $\theta = \theta'$ ) off the facet face – See the inset in figure 7.6. Increasing  $\theta$  also increases  $R$  via the cosine terms as shown in Fig 7.7, however, it also increases the size of the grating,  $W$ , since  $\alpha = \delta + \theta$  and thence by simple projection of  $d_1$  onto the surface of the grating surface with increasing  $\alpha$ . This increases the grating cost and the size of the camera lens required to accommodate the larger  $d_2$ . The final choice, due to these effects, and the limitations on  $f_l$  noted below, led to a choice of  $\theta = 9^\circ$  and thence  $\Psi = 18^\circ$ .

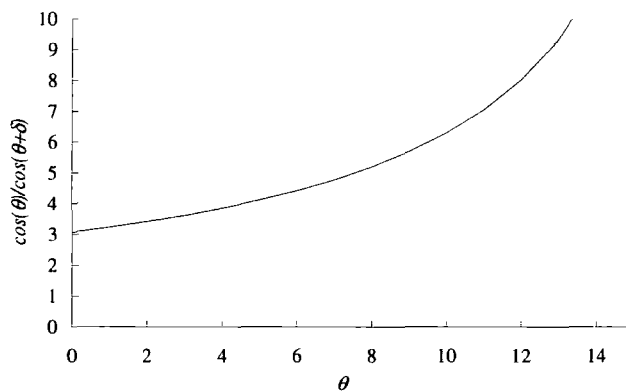


Figure 7.7 - The fractional cosine term in Eq.7.14. All angles in degrees.

The fibre output is collimated by the aspherical lens and the slit placed in the far field. This is done in order that various slit widths,  $w$  can be slotted in for a desired spectral resolving power and is shown schematically in Fig 7.8

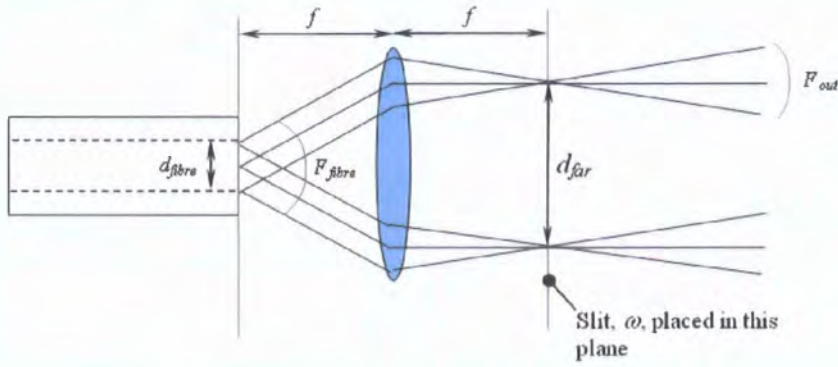


Figure 7.8 – The fibre, lenslet, slit geometry

The relationship between the relevant variables in Fig 7.8 is

$$\frac{F_{out}}{d_{far}} = \frac{F_{fibre}}{d_{fibre}} \tag{7.13}$$

where  $d_{far}$  is the fibre far-field output. The slit,  $\omega$ , was placed in the far-field as shown in Fig. 7.8. In order to increase  $f_l$  but retain a reasonably sized collimator beam size,  $d_1$  and thence  $W$  and  $d_2, d_{fibre}$  must be minimised.

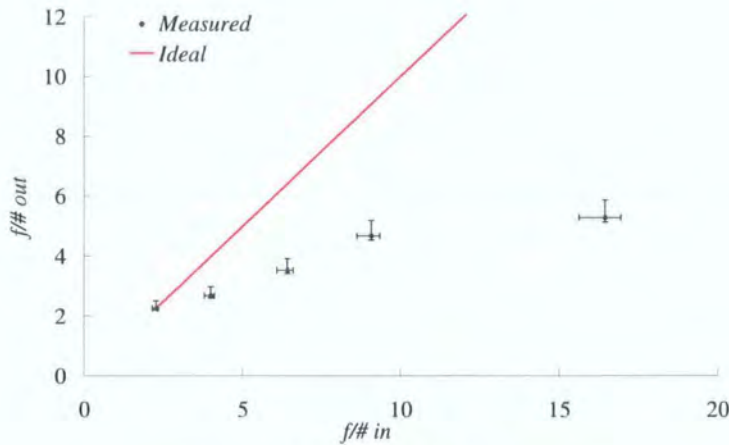


Figure 7.9 The FRD plot of the 50µm fibre

The FRD of a 50µm diameter fibre (Thorlabs AFS80/125Y) was measured using the apparatus described in section 2.4.2, by simply replacing the single-mode fibre with the multi-mode fibre. Some considerable care was taken to ensure good end face quality and to minimise mechanical stress in the fibre mounts. The FRD was found to

be limited to  $f/5.5$ . There are examples of fibres with a slower FRD output but this fibre gave a good practical match between the size of the far-field image,  $d_{far}$  and commonly available slit widths and Fabry lenses (focal length, 4mm used) that yielded an  $F_{out} = 80$ . This was slow enough to allow a large  $f_1$  but with small  $d_1$ , and with an R2.9 grating,  $d_2$  small enough for (relatively) cheap stock optics to be used. The final specifications are included in table 7.1

Grating Newport (Richardson) Part No. 53-025 -453E R2.9 ( $\delta = 71.0$ deg)					
$\Psi = 18$ deg					
$f/\#_{in}$	$f_1, m$	$d_1, m$	$W, m$	$d_2, m$	$f_2, m$
80.000	1.050	0.013	0.075	0.035	0.750
Slit width	Spectral resolution				
100 $\mu$ m	105.0 k				
200 $\mu$ m	52.5 k				
500 $\mu$ m	21.0 k				
No Slit	7.9 k				

Table 7.1 – The spectrometer specification

In order to measure the dispersion the fibre was removed and the 100 $\mu$ m slit illuminated with a Sodium discharge lamp. The spectrum of the Sodium D line recorded is shown in Fig 7.10. The FWHM of the slit image, recorded using a 633nm laser, is 4.45 pixels across<sup>11</sup>. The separation of the line centroids in Fig 7.10 is 474 pixels yielding a dispersion of  $(589.592\text{nm} - 588.995\text{nm}) / 474.000 = 1.259 \times 10^{-3}$  nm/pixel. The spectral resolution at the Sodium doublet wavelength with the 100 $\mu$ m slit, is therefore,  $589.592\text{nm} / (1.259 \times 10^{-3}\text{nm/pixel} \times 4.450 \text{ pixels}) \approx 105\text{K}$ , well matched to the exact figure in Table 7.1.

<sup>11</sup> Measured using a high quality 633nm laser and analysed using GAUSSFIT in IDL.

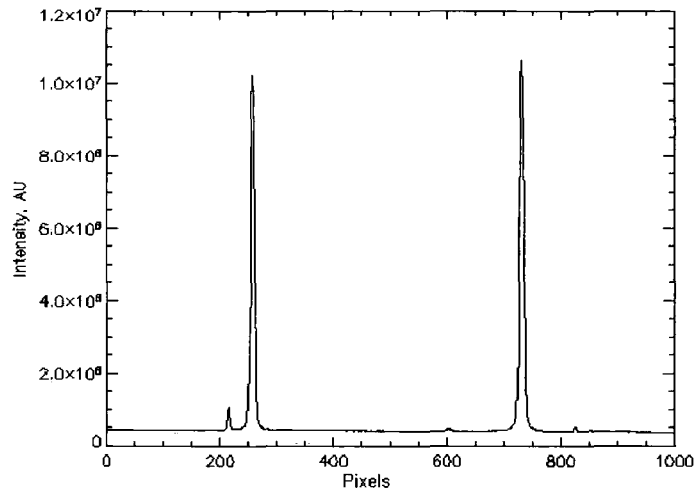


Figure 7.10 – The spectrum of the Sodium discharge lamp

Three narrowband filters,  $579.8 \pm 0.8\text{nm}$ ,  $633\text{nm} \pm 0.5\text{nm}$  and  $905\text{nm} \pm 5\text{nm}$  were used to provide the test wavelengths. Originally, an Oriel monochromator (74000) was used to illuminate the system, however, heating of the internal optics occurred due to the high power illumination required ( $>100\text{W}$ ). Drifts in wavelength of the order of  $0.5\text{nm}$  or so between measurements were observed and over long integration times this effect would mask other sources of noise, such as the modal noise the apparatus was constructed to investigate.

The grating order at the three test wavelengths of  $579.8\text{nm}$ ,  $633\text{nm}$  and  $905\text{nm}$  is 102, 94 and 65, respectively. Noting the bandwidth of each filter, then, cross dispersion is avoided since free spectral ranges ( $\lambda/m$ ) are  $5.7\text{nm}$ ,  $6.8\text{nm}$  and  $13.9\text{nm}$  respectively.

## 7.5 Experimental investigation of modal noise – Multimode fibre

### 7.5.1 Introduction

In this section the series of experiments undertaken to quantify modal noise effects when feeding the high dispersion spectrograph described in the previous section are presented. Eq (7.6) was derived assuming perfectly coherent light and tests using laser illumination of the spectrograph are detailed in section 7.5.3. The range of experiments conducted using the rather more interesting partially coherent light are then described in sections 7.5.4 onward. Due to the apparent confusion in the literature in this area, I have explicitly explained my analysis in detail in section 7.5.2. The results are discussed in section 7.6 with suggestions for further work are found in Chapter 8.

### 7.5.2 Details of the analysis

Each recorded frame consists of a single order, illuminated by the laser line filter, in the spectral direction with the spectrum height determined by the illuminated length of the slit. The spatial extent thus depends on the input focal ratio to the fibre and the amount of FRD within the fibre.



*Figure 7.11 – (a) An un-agitated spectrum, (b) Agitated spectrum. Both taken within a few seconds of each other. A very slow input focal ratio, with attendant very low  $S/N_M$ , is shown since the modal noise along the slit in the un-agitated case can actually be seen by eye, even with partially coherent illumination. The beating along the spectrum is due to the laser filter.*

Each image was flat-fielded by dividing by an agitated image recorded with four times the integration time. The agitation has the effect of removing modal noise and is described in detail in section, 7.5.4.1. As we shall see in the next section the agitated results agree extremely well with the photon limit. Further, this technique removes any

variation in modal noise due to effects such as thermal changes in the environment during the extended flat-field exposures by comparison to the shorter test exposures. Since a static fibre technique was used by Baudrand & Walker, I also ran some quick checks of agitated flat-fielded images against images that were flat-fielded using a static fibre in a different position to the test image and found no difference, within experimental uncertainty. The flat-fielded test image was then summed in the slit direction to yield a 1-dimensional spectrum. e.g. Fig 7.10.

As is common in astronomical analysis, the measured  $S/N$  value is taken as  $S/N_M = \bar{x}/\sigma_x$ , the mean photo-electron count divided by the standard deviation taken over the  $q$  pixels of the spectrum length. In this work, this is typically the full 1280 pixels of the CCD width.

The photon noise per pixel is given by  $S/N_p = N/\sqrt{N+B} \times 1/\sqrt{q}$ .  $B$  is the total background photo-electron count and  $N$  the total, background subtracted, spectrum count over the  $q$  pixels. In all cases, the integration was allowed to continue until the readout and dark count noise contributions were negligible. The total photon noise  $N/\sqrt{N+B}$  is expressed as sum over all the pixels in the spectrum and so the factor of  $1/\sqrt{q}$  is included to yield the per pixel value.

The predictions of Eq.(7.6) are taken over the entire fibre output. Since the output, a single resolution element, is then re-imaged onto the detector and sampled by  $p$  pixels in the 1D spectrum then the  $S/N$  prediction must be multiplied by  $1/p / \sqrt{1/p} \equiv \sqrt{1/p}$ . i.e. the per pixel value is smaller than the value associated with the entire resolution element. This is in contradiction to Grupp's approach<sup>[3]</sup>. He multiplied his results by  $\sqrt{p}$ . Since we disagree on this point, I have checked the relationship experimentally with the results described in section 7.5.3.

### 7.5.3 Coherent illumination

The fibre, 45m in length, was illuminated by a 633nm HeNe laser whose beam was expanded and collimated and then fed into the fibre via an  $f/1.4$  lens, thereby filling the numerical aperture. Tests using a 100 $\mu\text{m}$ , 200 $\mu\text{m}$  and 500 $\mu\text{m}$  slit and no slit (1.33mm) were performed and the signal to noise measured over 50 images, each with significant fibre movement between them. Each  $S/N$  value was checked over 25, 40 and 50 of the images to ensure that a stable result had been achieved. Figure 7.12 shows that in the coherent regime the correlation between the predictions of Eq (7.6) and the experimental data are excellent. With reference to the last section, in each of the four cases, the per pixel value was a factor of  $\sqrt{1/p}$  smaller than the value over the entire image.

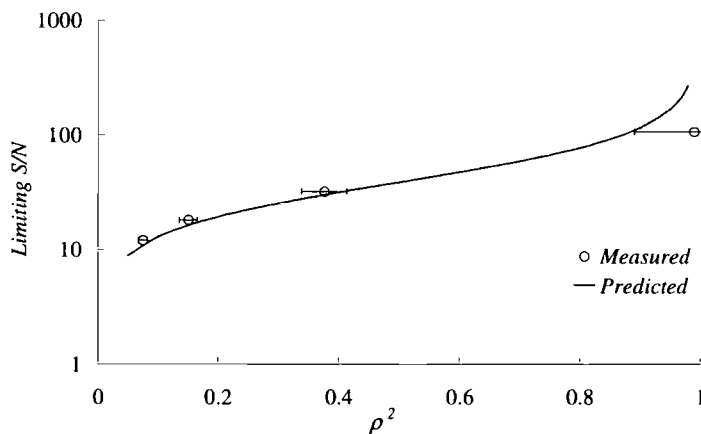


Figure 7.12 – Measured and predicted limiting  $S/N$  values under coherent illumination

The no-slit data point is plotted at  $\rho^2 = 0.999$ . (A perfect match for the predicted curve is found if the point is plotted at  $\rho^2 = 0.9$ ). The optics of the spectrograph were significantly oversized with respect to both  $d_1$  and  $d_2$  (Fig. 7.6) and so any loss mechanism such as scattering from dusty optics would affect all four data points. However, Eq (7.6) is singular at  $\rho^2 = 1$  and indeed, Goodman & Rawson seemed satisfied that a value of  $S/N_M = 370$  was a good approximation to infinity. The measured value in the above graph was 110 although the horizontal (1SD) error bar does allow for a rather better alignment of experiment and theory. Vertical error bars are smaller than the symbol size. The horizontal error bars are due to the difficulty in measuring  $A_f$  due to problems estimating image extents with no slit present (Fig 7.8).

Gratings are known to react differently to each incoming linear polarisation state and possibly then might play some part in the propagation of modal noise. The fibre used is not polarisation preserving<sup>12</sup> and hence both linear polarisation states were partially populated at the fibre output. Since good agreement was found between theory and experiment then any polarising affects due to the grating do not seem to affect the modal noise and the spectrometer can be considered as a simple light collecting device in this respect.

#### 7.5.4 Partially coherent illumination

In real astronomical measurements, at very high dispersions, the light entering the spectrograph is *partially* coherent and this will effect the *S/N* results. In order to test this, the laser was removed and the fibre illuminated using a scheme similar to Fig 5.15 but with a 150mm collimating lens and a 12mm maximum diameter iris. The laser line filters were placed in the collimated beam ensuring that they were operating at their centre wavelength. Different iris settings thus allow different input focal ratios to the fibre to be set.

##### 7.5.4.1 Agitation

Baudrand & Walker note that agitation of the fibre removed the modal noise. This technique was actually first noted by Daino *et al* in 1980<sup>[8]</sup>. In my work, various agitation schemes were tried but the most successful was found to be a piezo vibrating toothbrush with its head removed. Figure 7.13(a).

It is important to note that in configuration (b) of Fig 7.13 the agitator yielded poor results with significant differences between agitated and photon limited cases. This is attributed to the fact that modal noise is dominated by fibre displacement, with respect to thermal changes for instance. Sufficient agitation therefore implies sufficient movement of the fibre. In the configuration shown in panel (c) the movement of the fibre was large enough to yield measurements such as the (typical) green traces in Fig 7.14.

---

<sup>12</sup> This was checked by monitoring the output at the slit when a polariser was rotated with respect to the slit. No preferential directions were found even with the laser illumination.

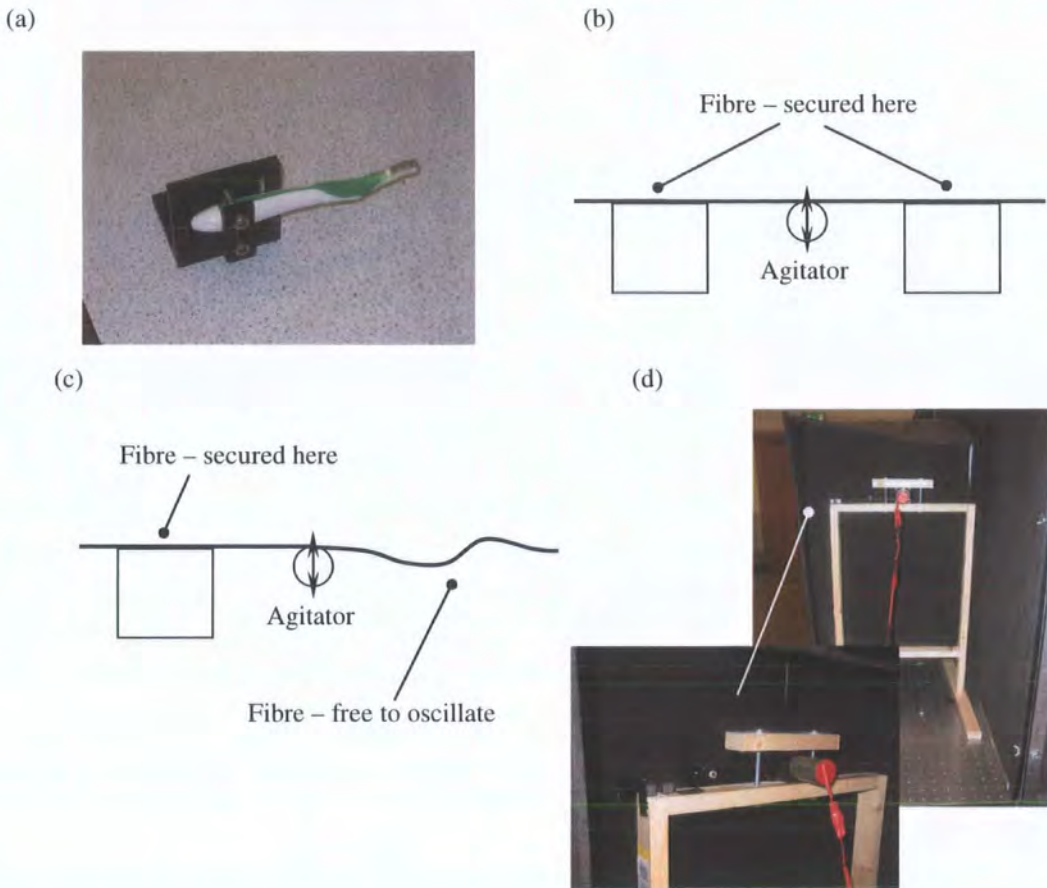


Figure 7.13 – (a) The toothbrush agitator, (b), (c) toothbrush configurations tested, (d) The slow moving agitator

In all cases tested, in configuration (c), the agitated spectrum, was found to be in good agreement (within 5%) of the photon limited case. The photon case was computed from the measured photon count. This justifies the use of the agitated images for flat-fielding purposes, but for experimental rigour an extra 5% uncertainty is included in quadrature in all limiting  $S/N$  measurements to allow for this. – However, as we shall see in the coming sections, in practice, this is a very small contribution in comparison to the natural variation in the fibre modal noise itself.

It should also be noted that the amplitude of the fibre movement on the unsecured side of the agitator varied between a few millimetres to as much as 10-15mm with no apparent systematic change in the agitated  $S/N$  measurements.

To highlight further the importance of the amplitude of the fibre movement rather than the frequency of agitation, the slow moving agitator in figure 7.13(d) was constructed. The frequency of the slow agitator was about 0.25Hz or so, compared to  $\gg 10$ Hz of the toothbrush. Experimentally identical results were achieved with the period of rotation of the arm of the same order as the integration time but with a very large amplitude of movement .

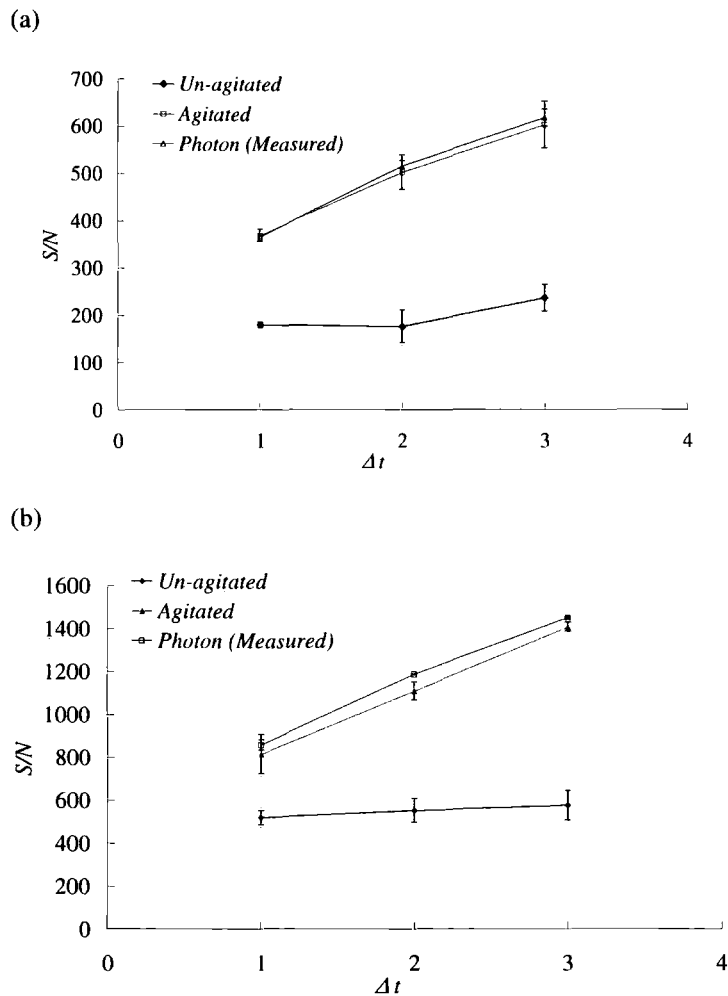


Figure 7.14 – Typical comparisons of un-agitated and agitated (configuration (c)) measurements and the measured photon limit. (a)  $200\mu\text{m}$  slit,  $F=4$  feed into fibre, (b)  $200\mu\text{m}$  slit,  $F=2$  feed into fibre.  $S/N$  per pixel shown in both cases.

So to conclude, fibre agitation yields  $S/N$  measurements that closely approximate the photon limit. Further, successful agitation depends primarily on the amplitude rather

than the frequency of the movement with the caveat that enough movement of the fibre occurs within the integration time.

#### 7.5.4.2 Slit width, and input focal ratio

In this section the results of varying the slit width and input focal ratio to the fibre are shown. The four input focal ratios were a filled numerical aperture  $>f/2$ ,  $f/6$ ,  $f/9$  and  $f/16$  and the slit widths yielding the  $\rho^2$  values shown in figure 7.15.

The limiting value was found by increasing  $\Delta t$  until stable (within experimental uncertainty) un-agitated measurements were found. Three data point at each of three  $\Delta t$  were used for 9 data points per limiting S/N value.

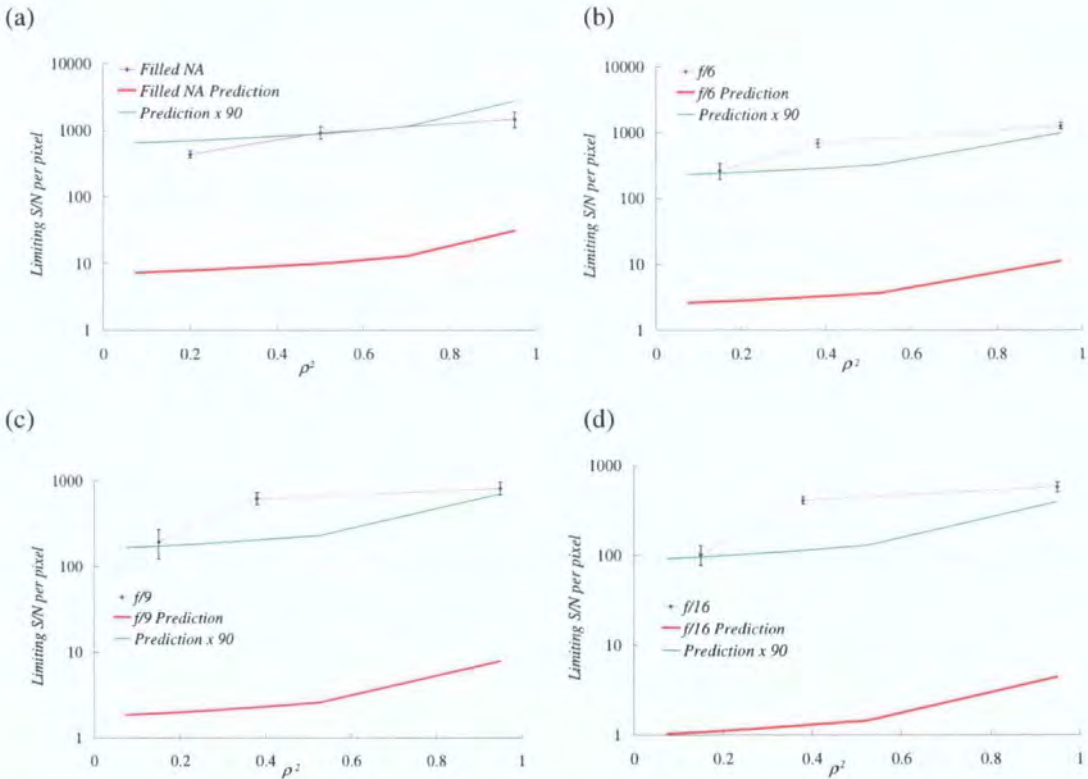


Figure 7.15 – The measured limiting signal to noise and associated value predicted by Eq's. (7.2), (7.4) and (2.7). Fibre fed with focal ratio (a)  $f/2$ , (b)  $f/6$ , (c)  $f/9$ , (d)  $f/16$ . All at  $633\text{nm} \pm 1\text{nm}$ . See text for further details.

Since the spectrometer has been characterised as a simple light collecting device with respect to modal noise (section 7.5.3) and since the illumination is the only change in the apparatus from the coherent light experiment, then it is immediately obvious that the partially coherent nature of the light is having a significant effect with greatly

increased measured, limiting signal to noise values of the coherent case. From Fig 7.15, the typical difference is two orders of magnitude.

To investigate further the input focal ratio was changed for the same slit width with the resulting curve in Figure 7.16. The plot shows only the limiting S/N values in the un-agitated case – i.e. The value at which the S/N trended regardless of how many more photons were collected. e.g. As more and more photons were collected in the  $f/17$  case the S/N was measured as trending to  $\sim 100$ . However total collected photons yielded the expected standard deviation of  $\sqrt{N}$  for  $N$  collected photons. The  $f/17$  experiment was continued until the photon limited S/N was  $>500$ , for example.

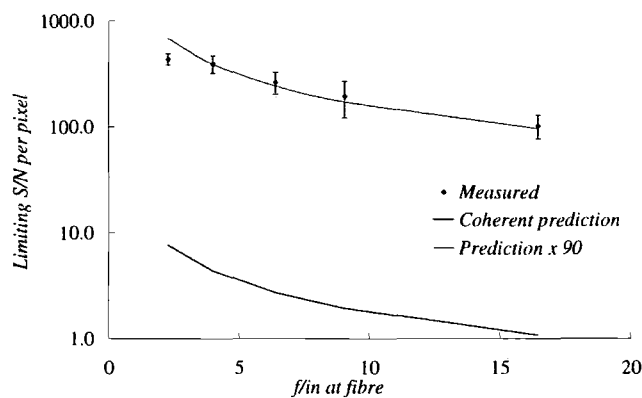


Figure 7.16 – The limiting S/N as a function of focal ratio input with a  $200\mu\text{m}$  slit. At  $633\text{nm} \pm 0.5\text{nm}$ .

Figure 7.16 shows that at least some correspondence between the coherent theory and the partially coherent experimental results remains. This might be expected on the basis that some correspondence principle must exist between the two regimes.

A simple first attempt to determine whether or not these data are due to a partially coherent regime might be to multiply the coherent prediction by some constant and the green curves in figures 7.15 and 7.16 are just that and seem to indicate that this is the case. Note however, that despite the good fit at  $\rho^2 = 0.15$  ( $200\mu\text{m}$  slit) other values of multiplying factor are required for other values of  $\rho^2$ . Further, the fit to the data when the numerical aperture of the fibre is filled is poor with the same constant of 90 even at  $\rho^2 = 0.15$ .

Finally, the functional dependence out to an  $f/16$  feed into the fibre indicates that Wood's concerns<sup>[14]</sup> are not applicable here since most fibres in astronomical instrumentation are fed at  $f/5$  or faster to avoid FRD. Possibly, some variation in  $S/N$  might be measured if a very bright single point source illuminated the fibre within the focal cone of the feeding lenslet, but since this would work to increase the  $S/N$ <sup>[14]</sup> it is of little concern, with the practically relevant result over the entire focal cone of the lenslet.

#### 7.5.4.3 Wavelength

The  $f/16$ ,  $200\mu\text{m}$  slit case was also recorded using a  $905\text{nm}$  and  $579.8\text{nm}$  laser filter with the result shown in Fig 7.17. I suspect that the mercury line filter ( $579.8\text{nm}$ ) was highly attenuating only over a small band about the centre wavelength, therefore allowing light from other wavelengths far away from the centre wavelength to reach the detector. However, the fit of the factored (coherent) prediction to both  $633\text{nm}$  and  $905\text{nm}$  is actually rather good. This would indicate that the centre wavelength of the partially coherent light has a similar effect to the coherent case. Changing the wavelength is tantamount to selecting the number of modes supported within the fibre, as indeed is changing the input focal ratio.

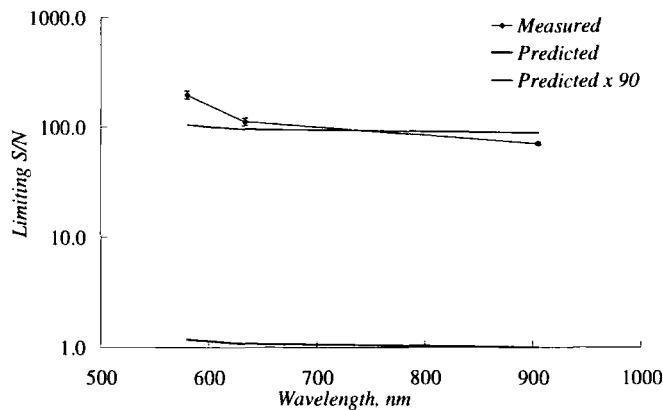


Figure 7.17 – The limiting  $S/N$  for three separate test wavelengths using the  $200\mu\text{m}$  slit and  $f/16$  feed into the fibre.

Therefore since a good correlation between measured and (factored) predicted values is found for the non NA filled case in Fig 7.16 then a good correlation in Fig 7.17 is entirely consistent.

#### 7.5.4.4 Fibre length

Since modal noise is due to the lack of intermodal dispersion then fibre length must play an important role. To within experimental uncertainty no change in the limiting signal to noise values was observed over the 1m to 45m range tested,, even when the numerical aperture was filled.

It should also be noted that Eq.(7.9) predicts that  $R_{crit}$  in the 45m, filled numerical aperture case is  $1.6 \times 10^6$ . Since the resolving power with the 200 $\mu$ m slit is 52.5K and yet we clearly observe modal noise, then as in the Baudrand & Walker's case, Eq.7.10 is also poorly aligned with my data.

### 7.6 Experimental investigation of modal noise – Single-mode PCF

Previous authors, including myself in the previous section, have demonstrated that the significant agitation of the fibre will remove the limiting signal to noise associated with the fibre modes, with the agitated value approaching the photon limit. However, other spectroscopic errors occur due to poor image scrambling, whereby spatial information at the input to the fibre is retained at the output. This, in turn, effects the distribution of light within the illuminated part of the slit and thence causes an extra uncertainty in the spectrum. Hunter & Walker, have suggested and indeed used a double scrambler arrangement of lenses <sup>[19]</sup>, whereby the near and far-field of two aligned fibres are swapped over. However, these devices are extremely lossy with typical throughputs of <20%.

As shown in Chapter 5, a small array of single-mode fibres can be used to collect light at 30-40% efficiency in the diffraction limit, with <82% into a single fibre. Single-mode fibres require neither expensive, and cumbersome, fibre agitators nor double scramblers. However, the polarisation doublet of the LMA fibre fundamental mode does have very slight differences in its two linearly polarised fields which are due to the six-fold symmetry of the holey structure and so possibly this might cause some modal noise.

The spectrometer described in this chapter was fed with an LMA-20 fibre and 905nm partially coherent light. 905nm was used instead of 633nm in order that the fibre was

operated well within the region of its attenuation spectrum unaffected by bend losses of any magnitude associated with bend radii which would likely snap the fibre. The minimum bend radius was at least 30cm. The analysis was careful to integrate out to the 95% points along the slit in order that any variation in the extents of the field were included in the signal to noise measurement. The resulting S/N measurements are shown in Fig 7.19.

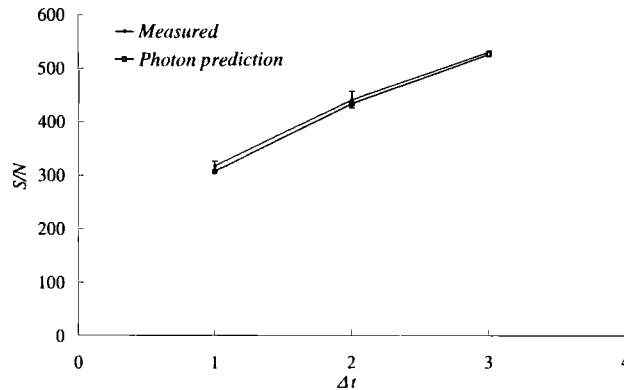


Figure 7.19 – The single mode LMA fibre feed signal to noise measurements.

The results are clearly photon limited and therefore to within the experimental uncertainty of a few per cent, from the diagram, the doublet does not affect the S/N performance of the single-mode PCF feed.

### 7.7 Summary

The coherent model of Rawson and Goodman has been shown to be inappropriate when applied to the partially coherent regime, despite the claims of previous researchers. In broad terms the measured values behave in a functionally similar manner when the numerical aperture is under-filled. Significant departures are observed when the numerical aperture of the fibre is fully populated, however. Further, the measured values also include a dependence on the slit width, highlighted by the need to multiply the coherent model predictions by a different constant at each value of  $\rho^2$ . No dependence on length was detected in the range 1m to 45m.

As far as building high dispersion spectrometers with multimode fibres is concerned, such as the forthcoming WFMS<sup>[20]</sup> project, ***no current theory exists that can adequately predict the performance.*** This is commented upon further in Chapter 8.

The single-mode PCF feed into the spectrometer was shown to be photon limited to within experimental uncertainty. This linked with the array scheme in Chapter 5 may provide an efficient way to feed very high dispersion spectrographs without the need for fibre agitation or lossy double scramblers and with a similar field of view.

### 7.8 References

- 1) 'Use and development of fiber optics on the VLT', J Baudrand, L Jocou, I Guinouard, ASP Conf Ser.152 Fibre Optics in Ast. III, 32 (1998)
- 2) 'Modal Noise in High-Resolution, Fiber-fed Spectra: A Study and Simple Cure', Baudrand, J & Walker, G.A.H PASP, **113**,851-858 (2001)
- 3) 'The nature of the *fiber* noise with the FOCES spectrograph', F Grupp, A & A **412** 897 (2003)
- 4) 'Numerical dispersion compensation for Partial Coherence Interferometry and Optical Coherence Tomography', A Fercherl, Optics Express **9** 12 p610 (2001)
- 5) L Ramsey, S Barden, 1988, ASP Conference series – Fibre optics in astronomy, 3
- 6) "On the application of optical-fiber image scramblers to astronomical spectroscopy" WD Heacock, AJ, 92, pp. 219-229, (1986)
- 7) Epworth, R.E. Proc. 4th European Conf. on Opt.Comms. (4ECOC) p492 Genoa (1968)
- 8) Epworth, R.E. Technical digest of the Topical meeting on Optical Fibre Communications, p106, Washington D.C. (1979)

- 9) 'Analysis and measurement of modal noise in an optical fibre', B Daino, G de Marchis, S Piazzola, *Electronics Letters* **15** p755 (1979)
- 10) 'Statistics of modal noise in fibers: a case of constrained speckle', E Rawson, J Goodman, *Optics Letters* **6** No.7 p324 (1981)
- 11) 'Speckle and Modal Noise in Optical Fibres Theory and Experiment', B Daino, S Piazzola and A Sagnotti, *Optica Acta*, 26,923, (1979)
- 12) 'Analysis and measurement of the modal-noise probability distribution for a step-index optical fiber', E Rawson, J Goodman, R Norton, *Optics Letters* **5** No.8 (1981)
- 13) 'Frequency dependence of modal noise in multimode optical fibers', E Rawson, J Goodman, R Norton, *J.Opt.Soc.Am.* **70** No.8 p968 (1980)
- 14) 'Actual modal power distributions in multimode optical fibers and their effect on modal noise', T Wood, *Optics Letters* **9** No.3 (1984)
- 15) 'Reduction of modal noise by using reduced spot excitation', J Saijonmaa, S Halme, *Applied Optics* 20 No.24 p4302 (1981)
- 16) 'Modal noise in multimode fibers under restricted launch conditions', G Papen, G Murphy, *Journal of Lightwave Technology* 17 No.5 p81 (1999)
- 17) 'Optical Waveguide Theory', A Snyder & J Love, Kluwer (1983)
- 18) 'The surface gravities of cool dwarf stars revisited', K Fuhrmann, M Pfeiffer, C Frank, J Reetz, T Gehren, *A & A* 323, 909 (1997)
- 19) "Scrambling properties of optical fibres and the performance of a double scrambler," T Hunter and L Ramsey, *PASP* 104, pp. 1244-1251, (1992)

- 20) 'Instrumentation and Technology Development at the Anglo-Australian Observatory', S Barden and J Bland-Hawthorn, American Astronomical Society Meeting 207, No. 173.17; Bulletin of the American Astronomical Society, Vol. **37**, p.1441, (2006)

# Chapter 8

---

## *Closing comments*

### **8.1** *Introduction*

This final chapter concerns itself with positioning this thesis within the current understanding of instrument science as it applies to astronomy. A brief overview of the thesis is given in Section 8.2 and its original contribution is explicitly listed in Section 8.3. Proposals of further work are described in Section 8.4 and a final word from the author is found in Section 8.5.

### **8.2** *Thesis synopsis*

This thesis has dealt with a range of issues surrounding the use of traditional and new fibre technologies in astronomy.

For instance, the beginnings of an investigation into how starlight can be coupled into single-mode PCF's for use in modern and possibly future photonic instrumentation was undertaken. Amongst other things, Chapters 4 and 5 have demonstrated the advantages of using large mode area photonic crystal fibres in single-mode fibre applications such as interferometry. Their use is proposed, for the first time, in high dispersion spectroscopy, with possibly reduced losses by coupling into single-mode fibres in comparison to multimode schemes that include double scramblers (see Chapter 7) but with an array of SM fibres providing a similar field-of-view to the multimode case.

Also, inherently multi-moded fibre issues such as OH suppressing fibres and modal noise in high dispersion spectrographs are dealt with. In Chapter 6 the performance of atmospheric line suppressing fibre systems was analysed on a model telescope and shown to be effective for use over narrow-bands. Chapter 7 investigated fibre modal noise in high dispersion spectroscopy, showing that the theories of coherent light as applied to communications are not applicable to the partially coherent regime of astronomy. This, leaving no current theory that can be used to predict the performance of a high R spectrograph.

As well as these, very specific pieces of work, an *underlying* theme of this thesis is that exploration of the electro-magnetic field properties of both traditional and photonic crystal fibres allows new possibilities for significant instrumental advances in fibre fed astronomical instrumentation. Interestingly, in both of the ‘multi-mode’ Chapters, 6 and 7, the single-mode (EM model dominated) regime still took on some importance. The OH suppression devices rely on the single-moded nature of the central array in order that the fibre Bragg gratings work efficiently and in the high dispersion spectroscopy case, modal noise was removed by using a single-moded photonic crystal fibre. (Although admittedly a step index single-mode fibre would have done).

### 8.3 Contribution

The original contributions of this thesis are as follows:-

- 1) A single LMA fibre can replace multiple step index fibres in current fibre interferometers fed directly with the telescope PSF with the same overall efficiency and slower feed optics. A deliberately defocused scheme was also proposed that could be used to increase overall coupling efficiency.
- 2) The use of LMA PCF allows the fibre to be fed with a field lens allowing coupling of the entire VIS-NIR into a single fibre. Further, this technique can be used to considerably simplify fibre stellar interferometry since only a single fibre + single feed + single recombiner is required.

- 3) The lenslet feed also allows contiguous single-mode sampling of the field therefore opening up the possibility of polarisation preserving integral field devices and the use of single-mode arrays to feed multiple photonic instruments or a single cata-dioptic high resolution spectrograph. In the diffraction limit the overall array coupling efficiency was shown to be ~35% but the performance in natural seeing is yet to be determined. The overall 'coupling' of multimode fibre feeds to high resolution spectrographs, via double scramblers, can be as low as <20%. Therefore the easier alignment of pupil images to the large core sizes of LMA single mode fibres may mean that efficiencies of this order might be achieved in the single-mode regime which is characterised by 100% intrinsic image scrambling and no need for an expensive fibre agitator.
- 4) The number of modes required in OH suppression single-mode fibre arrays to be useful in astronomy was determined for 4m and VLT class facilities. It was found that these fibres are likely to remain limited to >1000nm use for the near term due to current limits on manufacturability. A lower theoretical (diffraction) limit on the  $V$  parameter of approximately 13 was determined for lossless fibre astronomy.
- 5) A major paper search showed that the Grupps model can in fact be derived from the same basic model by Rawson & Goodman. The frequency correlation function of Rawson *et al* was shown to compare poorly with known experimental results and should not be trusted as a design tool. Experimental investigation of modal noise on a purpose built spectrometer has shown that the models of coherent light used in communications theory are not applicable to astronomical measurements which are, even at very high dispersion, found to be in the partially coherent regime.

#### 8.4 *Proposals of further work*

The scientific process of answering questions inevitably raises more questions and this thesis is no exception. The following is a brief list of both the (inevitable) issues that

remain unresolved in the work completed to date and where the author feels that more research would yield valuable results for instrument science in astronomy.

Chapters 4 and 6 on LMA fibres in interferometry and OH suppression fibres are essentially complete modelling exercises so there is little further work to do as long as one is happy with the underlying assumptions of each model. Both lend themselves to experimental falsification, of course. The coupling into the interferometer can be tested with a small aperture telescope in any atmosphere simply by selecting the aperture with respect to the local seeing. However, higher absolute throughput would decrease the noise in any measurements and therefore observations at some site of low seeing would be desired.

The excellent work on building MMF-SMF-MMF devices at the Birks/Knight group at the University of Bath, alongside Bland-Hawthorn at the AAO will ensure that practical demonstrations of OH suppressing devices on telescope are only a matter of time away.

There is much work yet to be done in the uses of LMA fibres in spectroscopy. Modelling the coupling into arrays of these fibres in natural seeing is required in order to determine if the lower coupling efficiency into arrays, compared to single SM fibres, in the diffraction limit is a general result. Investigation, experimentally, of what coupling efficiencies can be achieved using the new lenslet fed scheme is of paramount importance. This would include, for instance, solving the practical difficulties associated with gluing a lenslet to a holey structure. Interfacing LMA fibres with photonic instrumentation will also be a key area requiring investigation. The throughput, measured on a highly corrected 4m class telescope would indicate whether or not LMA fibres would be able to efficiently replace a multi-mode fibre with a double scrambler and fibre agitator. The same experiments performed on VLT class facilities would yield useful information on whether or not efficient coupling, again in the highly AO corrected regime, might be possible on ELT class telescopes. A word to the AO community. The coupling into optical fibres is computed on a EM (rather than squared field) basis and therefore ELT analyses, to come along in the next few years, should allow for this. Experimental determination of the usefulness of the deliberate defocus scheme would also be welcome.

Bringing together the ideas of Chapters 5 and 6, perhaps a few-mode MMF, thence split into an SMA and from there feeding a few cheap photonic spectrometers, in a similar manner to Fig 1.4(b), with OH suppression encoded on each fibre might be the way forward. Horton & Bland-Hawthorn's work on coupling starlight into few-mode fibres would be of particular significance here<sup>[1]</sup>.

A piece of work not presented in this thesis due to its incomplete nature is that if the PSF and geometrical image beat with each other to cause dark rings in the field of view then might there be solutions of this problem that super-resolve two overlapping PSF's? Preliminary exercises indicate that very small gains, possibly approaching the Sparrow limit might be made – The author remains hopeful of finding something interesting in this area!

A theoretical treatment of the relationship between modal noise, the spectrometer and fibre properties is required but is likely to be highly complex. However, falsification of the theory would naturally be required and so possibly, with the forthcoming WFMOs and PVRS projects in mind, the most expedient determination of at what dispersions and fibre properties modal noise disappears would be experimental. Both the theoretical and experimental tasks are currently in hand and will be published at a later date.

### 8.5 *Final words*

In this thesis I have tried to give a flavour of the possibilities of the exploration of the parameter space of optical fibres when viewed at a more fundamental level than the ray optical model whilst, also, addressing some key issues in the application of modern fibre technology to astronomy. As noted, the underlying theme is that *both* the EM and ray optical models have their place and should both be in the intellectual toolbox of any instrument scientist concerned with applying optical fibres to astronomy in the modern era. Certainly in the regime of single-moded or few-moded fibres, which are likely to play a central role in the application of photonic devices to astronomy, the ray optical model is inappropriate, to some degree. The importance of the ray optical model is certainly not diminished, of course, as the results of the

Chapter 6 show, however it is my opinion that from this point onward it not enough on its own. With this in mind and the original contributions noted in the previous section, I submit this work to the Centre for Advanced Instrumentation at Durham University, as my proposed doctoral thesis.

### 8.6 References

- 1) 'Coupling light into optical fibres near the diffraction limit', AJ Horton & J Bland-Hawthorn, SPIE **6269**, (2006)

